Fall 2013

Automatic construction and meshing of multiscale image-based human airway models for simulations of aerosol delivery

Shinjiro Miyawaki
University of Iowa

AUTOMATIC CONSTRUCTION AND MESHING OF MULTISCALE IMAGE-BASED HUMAN AIRWAY MODELS FOR SIMULATIONS OF AEROSOL DELIVERY

by

Shinjiro Miyawaki

A thesis submitted in partial fulfillment of the
requirements for the Doctor of Philosophy
degree in Civil and Environmental Engineering
in the Graduate College of
The University of Iowa

December 2013

Thesis Supervisor: Professor Ching-Long Lin

Graduate College
The University of Iowa
Iowa City, Iowa

CERTIFICATE OF APPROVAL

PH.D. THESIS

This is to certify that the Ph.D. thesis of

Shinjiro Miyawaki

has been approved by the Examining Committee for the thesis requirement for the Doctor of Philosophy degree in Civil and Environmental Engineering at the December 2013 graduation.

Thesis Committee: _____
Ching-Long Lin, Thesis Supervisor

_____
Allen Bradley

_____
James Buchholz

_____
Eric Hoffman

_____
Jia Lu

_____
Jacob Odgaard

_____
Merryn Tawhai

To my parents and brother

ACKNOWLEDGEMENTS

First of all, I am deeply grateful to my thesis supervisor, Dr. Ching-Long Lin. It was very fortunate for me that he gave me the directions of the study and I had the initiative to progress toward the directions. I greatly enjoyed doing my research thanks to his motivation, encouragement, and patience. Without his persistent support this thesis would not have been possible.

My appreciation also goes to Dr. Tatsuaki Nakato who gave me an opportunity to study at the University of Iowa after I got my Master's degree in Japan and was my advisor temporarily until he retired. The course of this study would not have started without his generous support. I would like to thank all of my committee members, especially Dr. Merryn Tawhai who helped me understand the in-house geometric airway model. Improving this model became my main contribution.

I would like to thank all of former and current members of Ching-Long Lin's lab, especially Dr. Jiwoong Choi and Dr. Haribalan Kumar with whom I always had insightful discussion about the in-house fluid, solid, and particle solvers. I would also like to thank my colleagues in the hydraulics lab, IIHR, especially Dr. Alejandro Castro and Daniel Gilles who always encouraged me during the course of this study.

This work was supported in part by NIH Grants R01-HL-094315, U01-HL-114494, and S10-RR-022421. I also thank the Texas Advanced Computing Center, San Diego Supercomputer Center, and Extreme Science and Engineering Discovery Environment sponsored by the National Science Foundation for the computer time.

ABSTRACT

The author developed a computational framework for the study of the correlation between airway morphology and aerosol deposition based on a population of human subjects. The major improvement on the previous framework, which consists of a geometric airway model, a computational fluid dynamics (CFD) model, and a particle tracking algorithm, lies in automatic geometry construction and mesh generation of airways, which is essential for a population-based study. The new geometric model overcomes the shortcomings of both centerline (CL)-based cylindrical models, which are based on the skeleton and average branch diameters of airways called one-dimensional (1-D) trees, and computed tomography (CT)-based models. CL-based models are efficient in terms of pre- and post-processing, but fail to represent trifurcations and local morphology. In contrast, in spite of the accuracy of CT-based models, it is time-consuming to build these models manually, and non-trivial to match 1-D trees and three-dimensional (3-D) geometry. The new model, also known as a hybrid CL-CT-based model, is able to construct a physiologically-consistent laryngeal geometry, represent trifurcations, fit cylindrical branches to CT data, and create the optimal CFD mesh in an automatic fashion. The hybrid airway geometries constructed for 8 healthy and 16 severe asthmatic (SA) subjects agreed well with their CT-based counterparts. Furthermore, the prediction of aerosol deposition in a healthy subject by the hybrid model agreed well with that by the CT-based model. To demonstrate the potential application of the hybrid model to investigating the correlation between

skeleton structure and aerosol deposition, the author applied the large eddy simulation (LES)-based CFD model that accounts for the turbulent laryngeal jet to three hybrid models of SA subjects. The correlation between diseased branch and aerosol deposition was significant in one of the three SA subjects. However, whether skeleton structure contributes to airway abnormality requires further investigation.

TABLE OF CONTENTS

LIST OF TABLES

Table

LIST OF FIGURES

Figure

CHAPTER 1
INTRODUCTION

1.1 Background

The study of aerosol deposition in the human lung is important because aerosols can affect human health in both negative and positive ways. The inhaled aerosols include cigarette smoke, dust, and aerosolized pharmaceutical drugs (Figure 1.1). For example, cigarette smoke is the main cause of chronic obstructive pulmonary disease (COPD) and lung cancer, and environmental factor such as dust can cause asthma symptoms in addition to genetic factor[66]. Conversely, aerosolized pharmaceutical drugs can be used for the treatment of lung diseases like COPD, asthma, and cystic fibrosis (CF) through airway wall, and systemic diseases such as headache and diabetes through alveoli[22, 27, 46].

Exposure to environmental factor can cause the development of lung diseases and exacerbate symptoms. Higher density of aerosols in the environment can obviously increase the risk of diseases, but other factors could cause the variability in risk under the same environmental condition. The delivery of aerosols in the human lungs is mainly determined by breathing pattern, geometry of the lung, and physical characteristics of the aerosols. For example, higher flow rates, narrower airway branches, or larger branching angles cause higher aerosol deposition in the proximal region, while larger gravity angle results in higher aerosol deposition in the peripheral region. In addition, larger aerosols deposit in the proximal region and smaller aerosols in the

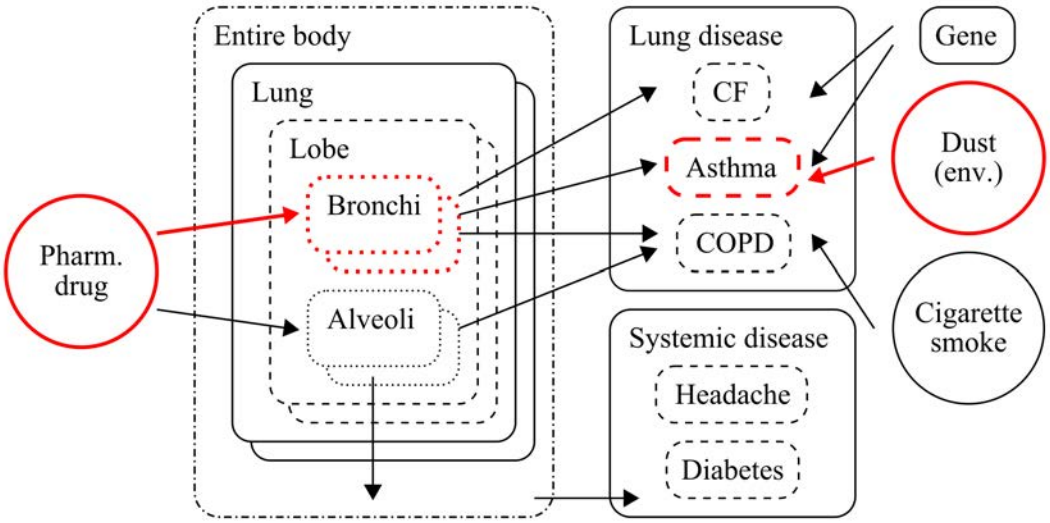

Figure 1.1: The relationship between aerosols and the human lung. "Pharm.", "Gene", and "env." stand for pharmaceutical, genetic factor, and environmental factor, respectively.

peripheral region. However, the correlation between lung diseases and the important factors governing aerosol deposition remains unclear. A better understanding of the correlation could improve the prevention and treatment of lung diseases.

Aerosol therapy is an effective drug delivery method. Aerosolized pharmaceutical drugs are conveniently delivered to the human lung without pain and the drugs act rapidly when the inhalers are properly used[22]. Aerosol therapy is most effective when the drugs are successfully delivered in the right amounts and to the correct regions of the lung. The drugs should be delivered to different regions of the lung depending on the disease to be treated or the receptor for the drugs to be used[6, 50]. For example, the drugs need to be delivered to the bronchi for bronchitis (COPD),

asthma, and CF, and the alveoli for emphysema (COPD). The receptor for one drug can be distributed in the proximal branches, while the receptor for another can be distributed in the peripheral branches. A better understanding of aerosol delivery would make aerosol therapy more effective.

Aerosol delivery in the human lung has been investigated experimentally and numerically. The experiments can be performed using living lungs (*in vivo*) and physical lung models (*in vitro*), but it is still difficult to accurately measure local aerosol deposition, e.g., on one branch or smaller scale[39]. The results from numerical simulations (*in silico*) can be analyzed in detail, although the models involve uncertainties and require excessive computational time. For example, it can take a week to simulate the aerosol delivery in one subject during one breath. In this study, we used *in silico* models to investigate aerosol delivery in detail.

An *in silico* model consists of a geometric, computational fluid dynamics (CFD), and particle tracking model. First, a geometric model constructs three-dimensional (3-D) airway geometry using the skeleton and branch diameters of the airway called one-dimensional (1-D) tree and/or, e.g., a 3-D computed tomography (CT) image of the airway. A CFD model then numerically solves the 3-D gas-flow field in the airway geometry. Finally, a particle tracking model computes the trajectories of aerosols using the gas-flow field. It is challenging to construct realistic geometry, impose realistic boundary conditions, and analyze aerosol distribution efficiently. In this study, we developed realistic and efficient *in silico* models.

1.2 Geometric Modeling of Conducting Airways

The symmetrical centerline (CL)-based geometric models have been used for the investigations of the fundamental physics of gas-flow and aerosol delivery in the human lungs (Figure 1.2). Balásházy and Hofmann[4] used a single-bifurcation geometry, which is the same as the one used in the experiment by Kim and Iglesias[47]. They are consistent with the third to fourth generation airways in Weibel's model[90]. Comer et al.[17] used a double-bifurcation geometry, which corresponds to the third to fifth generation airways in Weibel's model. Zhang and Kleinstreuer[97] used a triple-bifurcation geometry, which corresponds to the third to sixth generation airways in Weibel's model. Spencer et al.[75] built a geometry of up to 23^{rd} generation, i.e., the alveoli, based on Weibel's model and the statistics about the airway dimensions of adult lungs. Balásházy and Hofmann[4] demonstrated that the results from the simulations using the CL-based symmetric geometry can be compared to analytical solutions due to the simplicity of the geometry. Nonetheless, the CL-based symmetric model is impractical for the study of aerosol delivery in the human lungs because the human airway is asymmetric and contains trifurcations[40, 99].

The asymmetrical CL-based geometric models have been used for the simulation of aerosol delivery in representative human lungs (Figure 1.2). Balàshàzy and Hofmann[5] used the same single-bifurcation geometry as the one used by Kim and Iglesias[47], whose dimensions are equivalent to the third to fourth generation airways in Weibel's model but angles between the parent and the two child branches are not equal. In the seven-generation geometry constructed by van Ertbruggen et al.[84],

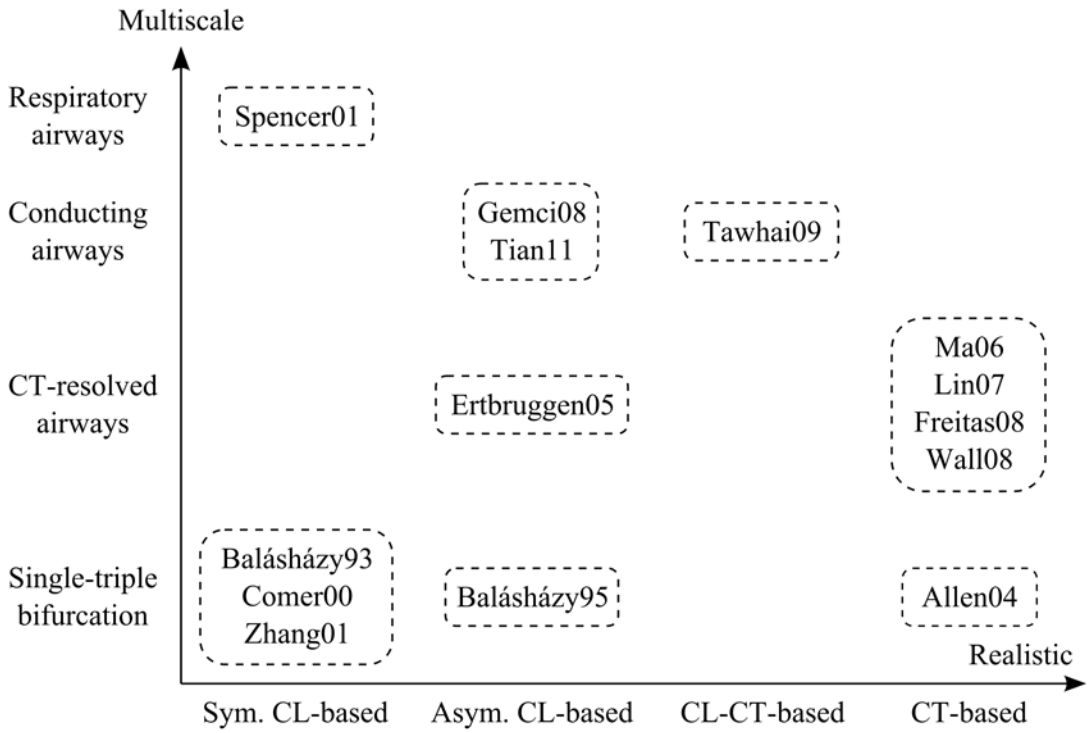

Figure 1.2: The previous studies on geometric lung model. The studies are listed in chronological order in each group. "Sym.", "Asym.", "CL", "CL-CT", and "CT" stand for symmetrical, asymmetrical, centerline, hybrid CL-CT, and (*in vivo*) computed tomography, respectively. "Balásházy93", "Balásházy95", "Comer00", "Spencer01", "Zhang01", "Allen04", "Ma06", "Ertbruggen05", "Lin07", "Freitas08", "Gemci08", "Wall08", "Tawhai09", and "Tian11" are the studies by Balàshàzy and Hofmann[4], Balàshàzy and Hofmann[5], Comer et al.[17], Spencer et al.[75], Zhang and Kleinstreuer[97], Allen et al.[1], Ma and Lutchen[59], van Ertbruggen et al.[84], Lin et al.[54], Freitas and Schröder[28], Gemci et al.[31], Wall et al.[87], Tawhai et al.[80], and Tian et al.[83], respectively.

the dimensions of airways and the branching angles were obtained from Horsfield's model[40], the azimuthal angles were obtained from the bronchoscopic images[82], and the orientation of the branches was checked using the CT images[82]. Gemci et al.[31] built a geometry of up to terminal bronchioles (the 17^{th} generation) based on the skeleton of a normal lung developed by Schmidt et al.[73]. Tian et al.[83] created a geometry extending up to terminal bronchioles (the 15^{th} generation) whose dimensions were based on the anatomical cast reported by Yeh and Schum[94], 3-D geometry was based on an empirically-defined representative geometry called the physiologically realistic bifurcation (PRB)[36], and azimuthal angles beyond the third bifurcation were assumed to be 90°[69]. The asymmetrical CL-based models based on the skeleton of representative lungs are not subject-specific. Even with subject-specific skeletons, airway branches are still modeled as straight tubes with cylindrical cross-sections. These approximations can result in simulation error especially in the proximal airways, where impaction is the dominant mechanism of the aerosol deposition.

The CT-based geometric models have been used for realistic simulations of aerosol delivery in subject-specific human lungs (Figure 1.2). It is crucial to use subject-specific geometries due to large intersubject variability in gas-flow and aerosol delivery in the human lung[13, 27, 34, 56, 77]. For instance, Allen et al.[1], Ma and Lutchen[59], Lin et al.[54], Freitas and Schröder[28], and Wall and Rubczuk[87] used 1-, 5-, 6-, 6-, and 4-generation geometries in their numerical simulations. The CT-based geometries can resolve not only non-circular cross-sections and non-straight

airways, but also cartilage rings mainly in the proximal airways. The CT-based models have two main shortcomings. First, the highest branch generation included in the model is limited by the resolution of CT scanners, and the terminal bronchiles (end of conducting region) cannot be resolved with the current technology. Second, it is time-consuming to pre- and post-process the CT-based geometries. The surface may require smoothing to remove artifacts, the geometry needs to be manually split branch by branch to analyze regional distribution and deposition of aerosols. Furthermore, the airway cross-sections need to be created for the investigation of secondary gas-flow profiles or monitoring aerosol delivery during the simulation. The manual surface smoothing and splitting are time-consuming because airway geometry is complex.

Previous studies have developed the laryngeal models to account mainly for the laryngeal jet in the trachea during inhalation. The CT scanning may not include the extrathoracic region (mouth-larynx) to reduce radiation exposure, but the larynx plays a crucial role in generating turbulence due to the laryngeal jet in the trachea as Chan et al.[11] suggested the requirement of laryngeal models based on their experimental study. Stapleton et al.[78] created an "average" extrathoracic geometry based on the CT images of 10 subjects and the observation of 5 living subjects. Kleinstreuer and Zhang[48] and Xi and Longest[93] made a circular and elliptic extrathoracic geometry based on the anatomical data reported by Cheng et al.[12]. Due to inter-subject variability in extrathoracic geometry, the CT-based model instead of "average" representative model should be used if the CT image is available.

Researchers have modeled the geometry of bronchioles to account for the multi-

scale nature of the human lung if the CT scanners do not resolve the terminal bronchioles. The symmetric 23-generation geometry built by Spencer et al.[75] was based on Weibel's model. Tawhai et al.[80] added the artificial bronchioles created with the volume-filling method to the CT-based geometries, resulting in a geometry extending to the terminal bronchioles. The asymmetric 15-generation geometry made by Tian et al.[83] was basically based on the anatomical cast reported by Yeh and Schum[94]. The asymmetric 17-generation geometry created by Gemci et al.[31] was based on the *in vitro* CT images obtained by Schmidt et al.[73]. *In vivo* instead of *in vitro* CT images are required for the geometries of the lungs at multiple inflation levels, but the current CT scanning technology is still far from resolving terminal bronchioles. The representative model can be unrealistic because the azimuthal angles need to be assumed, and the model by volume-filling method may still need to improve.

The hybrid CL-CT-based geometric models can overcome the shortcomings of the CL- and CT-based models (Figure 1.2). It should be noted that "CT" does not mean only CT images but any images, e.g., magnetic resonance imaging (MRI) images. Zhang et al.[96] fitted the CL-based geometry to the CT/MRI-based geometry to build a geometry of vascular system. Tawhai et al.[80] fitted the CL-based geometry to the CT-based geometry, and added the CL-based geometry of the CT-unresolved airways. The hybrid model is more realistic than the CL-based model, the surface is smoother than that of the CT-based model, and pre- and post-processing are more efficient compared to the CT-based model. The branches with more than two child branches in the model by Zhang et al.[96] has not been applied to the human lung,

and the model proposed by Tawhai et al.[80] does not account for trifurcations[99] and includes manual process in the fitting algorithm.

1.3 Aerosol Simulation in Conducting Airways

A number of boundary conditions for ending branches have been proposed (Figure 1.3a). The boundary conditions need to be imposed at the most distal branches of airway geometry. Balásházy and Hofmann[5] distributed the flow rate proportional to the cross-sectional area by imposing uniform bulk velocity. Liu et al.[57] imposed uniform pressure boundary conditions. Allen et al.[1] imposed uniform flow rate boundary conditions at each generation. Cebral and Summers[9] imposed traction-free boundary conditions with extrapolated velocities. van Ertbruggen et al.[84] imposed non-uniform flow rate boundary conditions based on Horsfield's model. Ma and Lutchen[60] imposed non-uniform flow rate boundary conditions based on Horsfield's model and uniform velocity in proximal and peripheral regions, respectively. Walters and Luke[89] imposed pressure boundary conditions at the end of resolved paths and randomly matched the pressure at the end of truncated path to the pressure in a resolved path at the same generation, which is referred to as "stochastic coupling". Yin et al.[95] imposed flow rate boundary conditions by connecting the ending branches to the image registration-based regional ventilation map with bronchiole geometry[81]. Tian et al.[83] imposed non-uniform flow rate boundary conditions based on Horsfield's model and uniform flow rate in proximal and peripheral regions, respectively. The method proposed by Yin et al.[95] reflects ar-

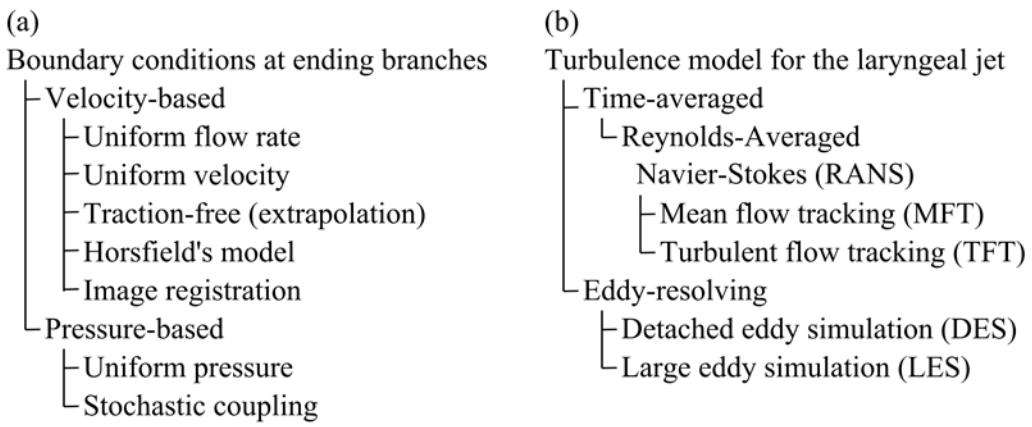

Figure 1.3: The boundary conditions at ending branches and turbulence model for aerosol simulations in conducting region. "Horsfield's model" is based on the flow rate proposed by Horsfield et al.[40]. "Uniform" means the uniform distribution over ending branches, not in the cross-section of each ending branch.

guably the most realistic regional ventilation, while dynamic, instead of quasi-static, regional ventilation map should be used and the geometric bronchiole model need to improve for smaller error at sub-lobe level.

Researchers have been used different turbulence models to account for the turbulence generated by the laryngeal jet in the trachea as discussed in Section 2.4 (Figure 1.3b). Gas-flow in the trachea can be turbulent due to the laryngeal jet created by the glottal constriction even if the Re in the trachea (Re_t) is lower than the critical Re (Re_c) for a straight pipe (~ 2300). RANS[20, 44, 48, 60, 71], detached eddy simulation (DES)[44], and LES[31, 44, 54, 98] have been used for the simulation of gas-flow in the human lung. RANS solves time-averaged governing equation without

resolving any eddy, while DES and LES resolve large-scale eddies. RANS has two major disadvantages to simulate the aerosol delivery in the human lung. First, RANS requires another model that adds turbulent fluctuation to the time-averaged flow field using turbulent statistics. Second, RANS may not accurately predict turbulent statistics depending on the nature of turbulent flow. The RANS-based aerosol simulation without adding turbulent fluctuation is referred to as "mean flow tracking" (MFT), which is physically correct only if there is no or very little turbulence. The RANS-based aerosol simulation with artificially added turbulence is referred to as "turbulent flow tracking" (TFT), which may not successfully reproduce the aerosol delivery, e.g., when the laryngeal jet oscillates with low frequency[63]. RANS can overestimate the critical Re in the trachea ($\mathrm{Re}_{c,t}$) by factor of three or more compared to the result from the experiments by Dekker[21].

Synthetic turbulence has been added to the flow above the glottal constriction for a realistic laryngeal jet below the constriction when a reduced geometric model that excludes the oral cavity is used. Gas-flow can become turbulent in the oral cavity, so the gas-flow above the glottal constriction should also be turbulent. Turbulent kinetic energy (TKE) can be prescribed in RANS models, while fluctuating flow field needs to be given in eddy-resolving models, e.g., DES and LES. Choi et al.[13] attempted to add random fluctuation to the time-averaged component of inflow based on LES-predicted turbulent statistics in the oral cavity. However, synthetic turbulence methods need to establish time-space correlation of synthetic turbulence to prevent rapid dissipation of turbulence. An ideal method to generate synthetic turbulence

should account for the correlation in time and space, but should not require any computation *a priori*. For instance, the synthetic-eddy method (SEM) proposed by Jarrin et al.[43] requires only the length scale and intensity of the turbulence to get homogeneous isotropic turbulence as the simulation progresses.

1.4 Objectives

The ultimate goal of this study is to automatically construct and mesh multi-scale image-based human airway geometries for the numerical simulations of aerosol delivery. The four specific objectives corresponding to Chapters 2-5 are to:

- Investigate the effect of turbulence on the aerosol delivery in the human lung using CT-based geometric airway model (Chapter 2)
- Develop a CL-based model including trifurcations (Chapter 3)
- Develop a hybrid CL-CT-based model including trifurcations (Chapter 4)
- Investigate the effect of airway skeleton structure on aerosol deposition in severe asthmatic (SA) lungs using the hybrid model (Chapter 5)

Chapter 2 presents eddy-resolving aerosol simulations with a CT-based model. There are two major CFD models to account for the turbulence of gas-flow in the human airway: time-averaged and eddy-resolving methods. Most of the previous studies of aerosol delivery used the former, but those studies showed two major shortcomings of their methods. They inaccurately predicted turbulent characteristics, and overestimated aerosol deposition even if the prediction of turbulent characteristics is reasonable. To show the importance of eddy-resolving methods in aerosol simulation,

we simulate gas-flow with different levels of turbulence using LES model. Furthermore, we use the results from the simulations with the CT-based model as reference to assess the accuracy of the hybrid model in aerosol simulation in Chapter 4.

Chapter 3 presents a CL-based model for trifurcations. The human lung is a tubular branching structure, so the simplest geometry is the CL-based geometry that consists of cylinders based on the 1-D tree. An existing model accounts for only bifurcations, although human airways contain trifurcations. The geometry of trifurcations can be constructed in the framework of the existing model. A 1-D tree can include very short branch that is not possible in 3-D geometry because of branch diameter. Furthermore, it is important whether the three child branches of a trifurcation are coplanar or not for the construction of geometry in the framework of the existing model. To automatically construct the geometry, the model uses criteria to identify and classify trifurcations. In addition to visualization, the CL-based geometry can be used for the simulation of aerosol delivery.

Chapter 4 presents a hybrid CL-CT-based model. The accuracy of the CL-based model needs to improve for the simulation of aerosol delivery. Therefore, we fit the CL-based geometry to the CT-based one, resulting in the hybrid geometry, in which the cross-sections can be non-circular, the airways can be non-straight, and the diameter can be non-uniform in each branch. To generate realistic level of turbulence of the laryngeal jet, we add a laryngeal geometry to the trachea. The new method generates computational grid automatically, specifies boundary conditions efficiently, and reduces the data from simulations systematically. The new method facilitates

the branch-by-branch analysis of aerosol deposition in multiple lungs.

Chapter 5 demonstrates the potential application of the hybrid model to investigating the effect of airway skeleton structure on aerosol deposition in SA lungs. Both airway skeleton structure and branch diameter are important factors in aerosol delivery, but it is well known that asthmatic branches are narrower than healthy branches. To control branch diameter, skeleton should remain the same and only branch diameters need to be modified. To define narrow branches and the branches with high deposition compared to healthy branches, we analyze both healthy and SA subjects. The CT-based model is not suited for the analysis of multiple subjects because the pre- and post-processing are time-consuming, while the hybrid model is more efficient. By design, each sub-domain of the hybrid geometry is consistent with each branch, so geometry and aerosol delivery can be compared branch by branch.

Chapter 6 summarizes Chapters 2-5 and presents potential improvements in the models and their applications.

CHAPTER 2
NUMERICAL SIMULATIONS OF AEROSOL DELIVERY IN THE HUMAN LUNG USING DIFFERENT CARRIER GASES

2.1 Introduction

Aerosols have strong relevance to human health because inhalation of environmental or toxic aerosols can cause diseases,whereas inhalation of therapeutic aerosols can treat diseases. For example, Gauderman et al.[29] recruited 1759 children in 12 southern California communities and measured their lung functions annually for a period of 8 years. They found that regional air quality has chronic, adverse effects on lung development in children as they reach adulthood. In addition to regional air quality, Gauderman et al.[30] found that micro-environments in association with freeway also affect lung functions of 3677 children, depending on how close they lived from a freeway of high particulate concentrations. Conversely, for treatment of diseases aerosols can be used to deliver drugs to the lung airways as well as to the bloodstream by depositing aerosols in the alveolar regions[27]. To maximize therapeutic drug effect, minimize unwanted side effects, and reduce treatment cost, it is important to effectively deliver inhaled drugs to different regions of interest in the lung[6, 79], e.g., proximal/peripheral region (serial targeting[6]), left/right lung, and upper/middle/lower lobe (parallel targeting[6]).Therefore, understanding the mechanisms of regional aerosol deposition is crucial.

Computational fluid dynamics (CFD) models have risen in popularity as a tool for studying aerosol deposition in the human lungs because they can be used

to track individual aerosol motion and quantify aerosol deposition in a region of interest[20, 44, 48, 51, 60, 71]. Since the flow field governs aerosol delivery, an accurate prediction of aerosol deposition depends on an accurate realization of flow field, which in turn depends on CFD airway model geometries, fluid solvers, and boundary conditions. Thus, use of a realistic airway geometry is desirable[54, 60, 87]. Even if the Reynolds number (Re, based on the bulk velocity) of the air flow in the lungs is lower than the critical Re of 2300 in a straight smooth pipe flow, the flow can become turbulent due to the glottal constriction that induces a turbulent laryngeal jet[54]. Thus, unsteady eddy-resolving CFD models, e.g., large-eddy simulation (LES), are necessary to accurately predict the flow field. Currently, since the whole lung geometry is not available for CFD simulations, proper boundary conditions are needed to produce physiologically-consistent regional ventilation at the whole lung level[95].

The airway geometry, flow rate, aerosol properties, and gas properties are the other important factors that determine aerosol delivery in the human lung. A number of experimental and numerical studies have been conducted to study the effect of aerosol size on aerosol delivery, a review of which can be found in Lippmann et al.[56]. In contrast, the effect of gas physical properties on aerosol delivery in the human lung is not sufficiently understood. Most previous studies have focused on a heliumoxygen mixture (heliox), as reviewed by Corcoran and Gamard[18]. Experimental studies showed that heliox lowers the airway resistance as compared with air, thus improves the ventilation for a given pressure drop, and that the alveolar aerosol deposition increases with decreasing airway resistance[18]. The oral deposi-

tions for different airway geometries, flow rates, and aerosol sizes were measured in the experiment by Grgic et al.[34] and the results showed the correlation between the oral deposition, Stokes number (Stk), and Re. Although experimental studies have provided an overall picture of aerosol deposition, regional (lung) aerosol distribution has not been comprehensively studied.

The aerosol distribution in a model of the bronchial tree extending from the trachea to the segmental bronchi was simulated to find the relationship between ventilation and aerosol distribution[20]. The aerosol delivery for laminar to turbulent flows in the oral cavity and trachea was investigated numerically using a Reynolds-Averaged NavierStokes (RANS) model[48], which showed the critical Re is higher than 1200 (critical flow rate of more than 15 L/min) in the trachea. The aerosol deposition for heliox in an oral extra-thoracic airway model was simulated using a RANS model[71], and the correlation of the oral deposition with not only Stk but also Re was confirmed. Nonetheless, the literature is currently lacking accurate CFD numerical studies on aerosol delivery in the extra- and intra-thoracic airways over a wide spectrum of Re (ranging from 190 to 2800) that arises due to variation in gas properties.

In this chapter, the effect of gas properties on regional areosol distribution is investigated numerically. The airway model consists of multi-detector row computed tomography (MDCT)-based upper and intra-thoracic central airways. The LES technique and an image registration-derived boundary condition are adopted to capture turbulent and transitional flow characteristics at a local level, and to match subject-

specific regional ventilation at the whole lung level, respectively. The aerosol delivery is then simulated using the Lagrangian tracking algorithm with unsteady turbulent flow fields.

2.2 Methods

2.2.1 Study Cases

Figure 2.1 exhibits the realistic geometric model of the human airway reconstructed from MDCT images[14, 51, 95]. The average airway diameters D_{aw} of the trachea, the left main bronchus (LMB), and the right main bronchus (RMB) were 18.8, 11.9, and 16.1 mm, respectively. Fine, medium, and coarse meshes of 15-, 8-, and 4-million tetrahedral elements were generated for a grid sensitivity analysis. The image-registration-derived boundary condition[95] was imposed at the end faces of the terminal airways to produce subject-specific regional ventilation. This method uses two MDCT volumetric lung image datasets from a single human subject, scanned at two different lung volumes, to derive physiologically realistic flow rates at the end of each ending branch in the human airway model (Figure 2.1). The CT intensities of the lung images can be used to calculate regional air volume distributions at the two lung volumes. By image registration, the mapping between the two images can be obtained to derive the regional air volume change (ventilation) of the subject. The entire conducting airway tree of the subject can also be constructed using the volume filling technique[81]. By overlapping the regional ventilation with the whole airway tree, the change of air content associated with individual terminal bronchioles

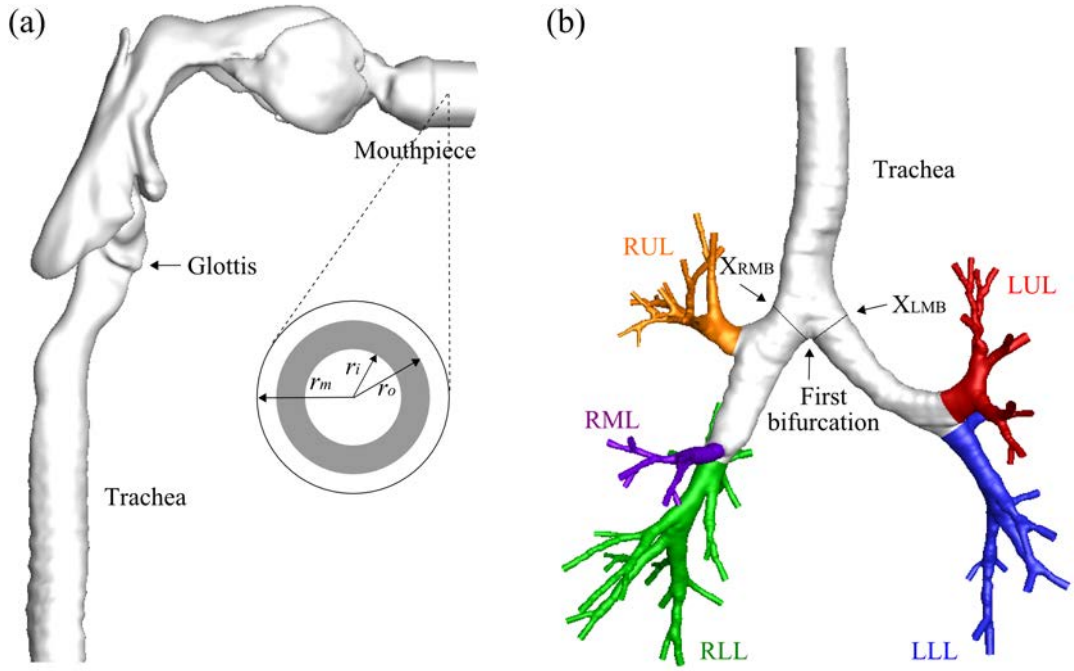

Figure 2.1: The airway model geometry and the definition of the terms used: (a) upper airways viewed from right and the region of aerosol release viewed from front, (b) lower airways viewed from front. r_m = radius of the mouthpiece, $r_{i,o}$ = inner and outer radii to define the region of aerosol release, LMB = left main bronchus, RMB = right main bronchus, LUL = left upper lobe, LLL = left lower lobe, RUL = right upper lobe, RML = right middle lobe, RLL = right lower lobe.

can be calculated. Then by connectivity of the tree structure, the flow rates for the MDCT-resolved ending branches can be determined. Details of the methodology are given in Yin et al.[95].

To investigate the effect of Re on regional aerosol distribution, four different carrier gases were considered: helium (He), a heliumoxygen mixture (He-O_2), air,

and a xenon-oxygen mixture (Xe-O_2). A steady inspiratory flow rate of 342 mL/s was imposed at the mouthpiece inlet for a time period of 2.16 s. The tracheal Re (Re_t, defined below) for He, He-O_2, air, and Xe-O_2 in this subject at this flow rate were 190, 460, 1300, and 2800, respectively. The airway model and the flow condition for the air case were the same as those by Lambert et al.[51] and Yin et al.[95]. The properties of these gases were summarized in Table 2.1. It is noteworthy that a heavier gas under the same inlet flow condition yields a higher Re. The left-right lung (LR) ventilation ratio for this subject is 0.98, which is derived from CT images via the image-registration-derived flow boundary condition[95]. In order to investigate the effect of LR ventilation ratios on aerosol delivery, the LR ventilation ratio in the He case was artificially reduced to 0.67 (2/3). This special case is referred to as "He23". A total of five cases were investigated: He, He23, He-O_2, air, and Xe-O_2.

The aerodynamic diameter (d_{aer}, defined below) is the only particle property that affects the trajectory of a spherical particle with diameter d, when particle Re (denoted by Re_p) $\ll 1$ and $d \gg k$, where λ is the mean free path of molecules in the gas[27].

$$d_{aer} = (sg)^{1/2} d \tag{2.1}$$

where sg is the specific gravity defined as the ratio of the particle density (ρ_p) over the water density. To study aerosol distribution, we chose $d = 2.5$ μm and $\rho_p = 1000$ kg/m^3, yielding $d_{aer} = 2.5$ μm for the following two reasons. First, the aerosols with d_{aer} between 1 and 5 μm were reported to achieve the most effective deposition in the human lung[37, 70, 77]. Furthermore, the main deposition mechanism for aerosols

Table 2.1: Fluid properties of He, He-O_2 mixture, air, and Xe-O_2 mixture.

Fluid	ρ_f (kg/m^3)	μ (kg/s m)	ν (m^2/s)	Re_t	$\lambda \times 10^6$ (m)
He	0.166	1.97×10^{-5}	11.9×10^{-5}	190	0.15
He-O_2	0.400	1.98×10^{-5}	4.95×10^{-5}	460	0.13
Air	1.200	2.04×10^{-5}	1.70×10^{-5}	1300	0.067
Xe-O_2	2.597	2.09×10^{-5}	0.81×10^{-5}	2800	0.064

[a] He-O_2 = 80%He-20%O_2 and Xe-O_2 = 40%Xe-60%O_2.

[b] ρ_f = fluid density, ν = kinematic viscosity, Re_t = trachea Reynolds number based on the trachea hydraulic diameter of 18.3 mm, and λ = mean free path.

[c] Re_t is presented with two significant digits.

of $d_{aer} > 1$ μm in the tracheobronchial region shown in Figure 2.1 is impaction. Second, the densities of aerosolized pharmaceutical drugs are close to that of water. Nonetheless, for model validation, we compared with the existing data of the oral deposition and the LR distributions for a wide range of aerosol sizes d_{aer} = 1.0, 2.5, 5.0, 10, 20, 40, 80, and 160 μm.

Ten thousand spherical aerosols were released at the mouthpiece, having a circular cross-section with radius r_m. The probability integral transform was used to generate the cylindrical coordinates (r, θ) of the aerosols released uniformly in the annular region between two radii r_i and r_o (Figure 2.1):

$$r = \sqrt{\xi\,(r_o^2 - r_i^2) + r_i^2} \tag{2.2}$$

$$\theta = 2\pi\zeta \tag{2.3}$$

where ξ and ζ are random numbers distributed uniformly between 0 and 1. If the aerosols are released uniformly over the entire cross-section of the mouthpiece, i.e., $(r_i, r_o) = (0, r_m)$, Equation 2.2 reduces to $r = \sqrt{\xi} r_m$. To study the effect of aerosol release location on aerosol distribution, we divided r_m into 10 uniform segments and released aerosols between two radii $r_i = (i-1)0.1r_m$ and $r_o = (i)0.1r_m$, with $i = 1-10$ at the mouthpiece. The average aerosol release location in any of these annular regions is denoted by r_c, namely $r_c = 0.5\,(r_i + r_o) = (i - 0.5)0.1r_m$. The uncertainty due to the random number generator is assessed in the He case. Based on eight different seeds in the random number generator, the uncertainty due to the seed on the LR aerosol distribution ratio is less than 1.5 %. An aerosol is considered to be deposited on the airway wall when the distance between the aerosol center and the nearest wall is smaller than the aerosol radius.

For model validation, the oral deposition was quantified using the deposition efficiency DE. The oral deposition efficiency DE_o is defined as the ratio of the number of aerosols deposited in the oral cavity to the total number of aerosols released in the mouthpiece. The local Reynolds number Re_l based on the local velocity scale U_l and the length scale D_l is defined as

$$\mathrm{Re}_l = \frac{\rho_f U_l D_l}{\mu} = \frac{U_l D_l}{\nu} \tag{2.4}$$

where subscript l is replaced with o for oral cavity and t for trachea, ρ_f is the fluid density, μ is the fluid dynamic viscosity, and ν is the fluid kinematic viscosity. Grgic et al.[34] used the geometrically equivalent diameter D_{mean} as D_l and the bulk velocity U_{mean} (based on D_{mean}) as U_l, where $D_{mean} = 2\sqrt{V/\pi L}$, and V and L are the

respective volume and path length of the airway segment.

The time history of the number of aerosols that passed the cross-sections X_{LMB} and X_{RMB} (Figure 2.1) was monitored at a time interval of 0.006 s. The particle flux is defined as the number of aerosols passing through the cross-section per unit time. The integration of the particle flux over time, i.e., the area underneath the particle flux curve, gives the cumulative aerosol number.

The tracheobronchial airway resistance R_{tb} was used to compare the bulk airway resistance for the four different gases. The R_{tb} is defined as the ratio of the tracheobronchial pressure drop Δp_{tb} to the flow rate at the mouthpiece Q_m. The Δp_{tb} is defined as the difference between the pressure at the mouthpiece p_m and the average of the pressures at all the terminal airways $p_{trm,i}$ in the CT-based airway model.

$$R_{tb} = \frac{\Delta p_{tb}}{Q_m} = \frac{p_m - \left(\sum_{i=1}^{N_{trm}}\right)/N_{trm}}{Q_m} \tag{2.5}$$

where N_{trm} is the number of the terminal airways.

2.2.2 Computational Method

The gas flow was simulated using an in-house LES code. The governing equations for the flow of incompressible fluids consist of the filtered continuity and momentum equations.

$$\frac{\partial u_i}{\partial x_i} = 0 \tag{2.6}$$

$$\frac{\partial u_i}{\partial t} + u_j \frac{\partial u_i}{\partial x_j} = -\frac{1}{\rho_f}\frac{\partial p}{\partial x_i} + (\nu + \nu_T)\frac{\partial^2 u_i}{\partial x_j \partial x_j} \tag{2.7}$$

using the summation convention for repeated indices, where u_i is the velocity components in x_i-direction, p is the pressure, ν_T is the subgrid-scale (SGS) eddy viscosity. The governing equations are integrated using the second-order characteristic Galerkin fractional four-step method. A pressure-Poisson equation is solved to satisfy the continuity equation, Equation 2.6. The SGS model by Vreman[86] is adopted to compute ν_T, which is reduced to zero for laminar flow. The time step is determined by the CourantFriedrichsLewy (CFL) condition. This model has been previously validated[14, 51, 54]. Further model validation can be found in the validation subsection.

2.2.3 Lagrangian Particle Tracking Algorithm

Aerosol trajectories were computed with the Lagrangian tracking algorithm using the simulated flow field. The main mechanism of particle deposition in the tracheobronchial region is impaction, so Brownian motion of the particles is not considered. The governing equation for the particle trajectory is

$$\frac{dv_{p,i}}{dt} = f_{D,i} + \frac{\rho_p - \rho_f}{\rho_p} g_i \tag{2.8}$$

where $v_{p,i}$ is the particle velocity, $f_{D,i}$ is the drag force per unit mass, and g_i is the gravitational acceleration. Since ρ_p is typically 1000 times greater than ρ_f, the coefficient for the second term is close to unity. The drag force per unit mass $f_{D,i}$ can be computed as

$$f_{D,i} = \frac{U_l}{\mathrm{Stk} \cdot D_l} \left(v_{f,i} - v_{p,i}\right) \tag{2.9}$$

where $v_{f,i}$ is the fluid velocity interpolated from the fluid velocity field u_i at the particle location and U_l and D_l are the respective local velocity and length scales as defined in Equation 2.4. The Stokes number Stk can be expressed generally as

$$\mathrm{Stk} = \frac{4}{3}\frac{\rho_p}{\rho_f}\frac{d}{D_l}\frac{U_l}{v_{rel}}\frac{1}{C_D}C_c\alpha^{3.7} \tag{2.10}$$

where v_{rel} is the magnitude of the particle velocity relative to the fluid velocity, C_D is the drag coefficient, C_c is the Cunningham slip correction factor[38], and α is the particle-particle interaction factor[27], which was set to 1 in this study due to the negligible particle volume per unit gas volume of 1.30×10^{-7} for 2.5 μm-particles. Particles with small Stk ($\ll 1$) follow streamlines, while particles with large Stk (~ 1) do not follow rapid changes in curved streamlines. C_D is generally a function of particle Reynolds number Re_p[65], which is defined as

$$\mathrm{Re}_p = \frac{v_{rel}d}{\nu} \tag{2.11}$$

When $\mathrm{Re}_p \ll 1$,

$$C_D = \frac{24}{\mathrm{Re}_p}, \text{ so} \tag{2.12}$$

$$\mathrm{Stk} = \frac{U_l\rho_p d^2}{18\mu D_l}\alpha^{3.7}C_c \tag{2.13}$$

For the four gases considered, a higher Stk implies a larger d.

2.2.4 Grid and Flow Time Interval Sensitivity

The aerosol depositions are sensitive to the velocity field near the wall, thus to the grid size. Therefore, the sensitivities of the regional aerosol distribution and the oral deposition to the grid size were investigated with three different computational

meshes. The average element sizes of the medium and the fine meshes were 82 and 66% of the element size in the coarse mesh. The oral deposition efficiencies DE_o of 2.5 μm-aerosols in air for the coarse, medium, and fine meshes were 6.5, 4.2, and 3.4%, respectively. The absolute differences in the oral deposition between the coarse and medium meshes and between the fine and the medium meshes were 2.3 and 0.8%, both of which are less than the uncertainty (3.4%) between our data and the empirical results of Grgic et al.[34]. In addition, the absolute differences in the DE_o of 2.5 μm-aerosols between Xe-O_2 and air and between air and He for the fine mesh are 1.4 and 2.0%, respectively. Therefore, the fine and medium meshes are sufficient to predict the oral depositions for different gases. The fine-mesh result is used in the following analysis.

For turbulent flow, the velocity field is unsteady, and the instantaneous velocity field, not the time-averaged velocity field, determines aerosol motion. Aerosol trajectories were computed by post-processing a time sequence of instantaneous flow fields. The effect of the time interval between two subsequent flow fields on the LR aerosol distribution was investigated for optimal data storage and computational time. We used the average integral time scale of turbulence ($\sim$ 0.003 s) in the region between the pharynx to the main bronchi as a reference time scale. The result showed that for 2.5 μm-aerosols computed in air using time intervals of 0.003 and 0.006 s, the difference between the LR aerosol distribution ratios was 0.01, which is smaller than the standard deviation of the LR aerosol distribution ratio. Therefore, the flow time interval of 0.006 s was used in the following analysis.

Because of the transient nature of turbulent flow, the aerosols need to be released multiple times to obtain time-averaged quantities, so the effect of the number of aerosol releases on average LR aerosol distribution was also studied. The time interval between consecutive aerosol releases was set to 0.048 s, which is much longer than the integral time scale of turbulence. The study showed that when the aerosols are released more than 8 times, the relative variation of the average LR aerosol distribution ratio is less than 1%. As described below in detail, only for the case of He-O_2, the flow became transitional with low-frequency oscillation, so the aerosols are released for 7 oscillatory periods with 8 aerosol releases per period. The mean and the standard deviation of the quantities obtained from multiple releases of aerosols are reported below.

2.2.5 Validation

The aerosol deposition efficiencies in the oral cavity and at the main bronchi were compared with previously published experimental results for validation. Additional validation is shown in Lambert et al.[51]. The oral deposition efficiency DE_o from the current simulation was compared with the DE_o from the similarity equation proposed by Grgic et al.[34] based on their experimental results:

$$DE = 1 - \frac{1}{b\left(\mathrm{Stk}_o \cdot \mathrm{Re}_o^a\right)^c + 1} = 1 - \frac{1}{11.5\left(\mathrm{Stk}_o \cdot \mathrm{Re}_o^{0.37}\right)^{1.92} + 1} \tag{2.14}$$

where Stk_o and Re_o in Figure 2.2 are calculated based on Grgic et al.[34] and the subscript o means "oral". In contrast to Lambert et al.[51], which assumed constant Re_o and different sizes of aerosols, the Stk_o and Re_o here differ due to differing gas

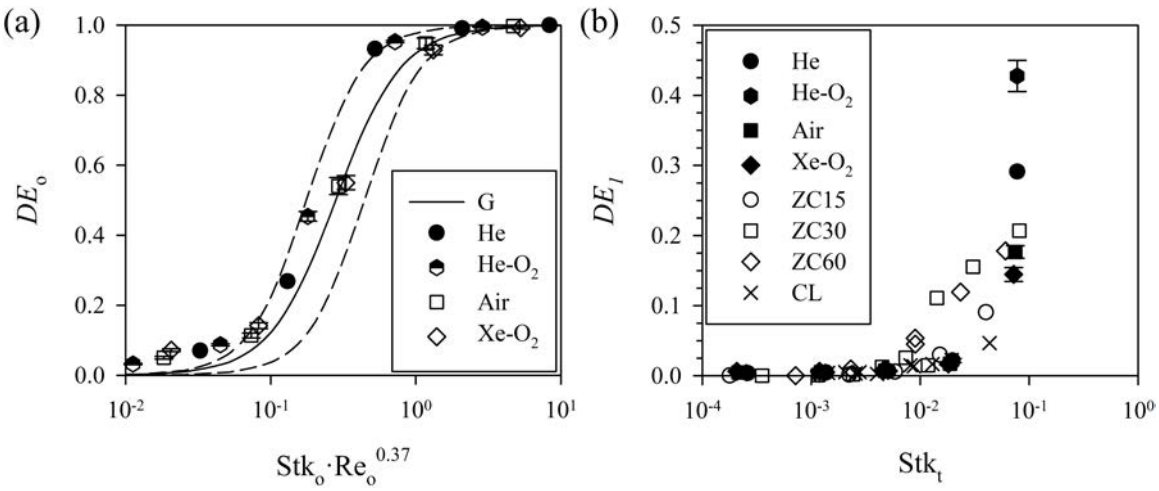

Figure 2.2: (a) The oral deposition efficiency compared with the similarity equation obtained experimentally by Grgic et al. (G)[34] with the dashed lines that envelop the experimental data. The parameters (b, c) in Equation 2.14 are (45, 2.2) and (6.0, 2.2) for the upper and the lower dashed lines, respectively. (b) The first generation deposition efficiency compared with the experimental results by Chan and Lippmann (CL)[10] and Zhou and Cheng (ZC)[100]. "ZC15", "ZC30", and "ZC60" denote the cases of 15, 30, and 60 mL/s, respectively, in Zhou and Cheng[100].

properties and aerosol sizes.

The current results agreed reasonably well with Equation 2.14. Sandeau et al.[71] used a different set of model parameters (a, b, c) = (0.30, 150, 2) in Equation 2.14, but the current results agreed better with Grgic et al.[34]. The current simulation slightly overestimates DE_o for a lower value of $\mathrm{Stk}_o \cdot \mathrm{Re}_o^{0.37}$. The difference may be attributed to the uncertainties in inter-subject variability, simulation, or experiment. We further compared the predicted deposition efficiencies at the first airway

generation DE_1 with the experimental measurements by Chan and Lippmann[10], and Zhou and Cheng[100]. Figure 2.2b shows that they are in good agreement.

2.3 Results

2.3.1 Flow Field

The predominant flow structures in the oral cavity and the trachea are the free-shear jets created by the constrictions at the mouth and at the glottis. Figures 2.3a-2.3c show that the spatial scale of the jet structure becomes smaller as the flow is more turbulent with increasing tracheal Re_t (or gas density). Figures 2.3d-2.3f show that, around the peripheral region of the jet, the flow is more dispersed and the length of the jet becomes shorter as Re_t increases. The length of the laryngeal jet is defined as the length of the region where the velocity magnitude is larger than the bulk velocity at the glottis. The laryngeal jet lengths are $7.91D_t$, $7.87D_t$, $2.74D_t$, and $1.74D_t$ for $\mathrm{Re}_t \sim 190$, 460, 1300, and 2800, respectively, where D_t is the average tracheal diameter. The comparison between Figures 2.3a-2.3c and 2.3d-2.3f clearly shows the transient feature of turbulent flow for the case of Xe-O_2. The values of the tracheobronchial airway resistance R_{tb} based on the time-averaged flow fields of He, He-O_2, air, and Xe-O_2 are 0.170, 0.233, 0.421, and 0.732 cmH_2O/(L/s), respectively, and the R_{tb} increases almost linearly with increasing Re_t.

Figure 2.4 shows that for the He case the turbulent kinetic energy (TKE) is negligible compared to that of Xe-O_2, and that the TKE normalized by the bulk velocity is less than 10^{-8} in the trachea. Therefore, the flow in the He case is laminar,

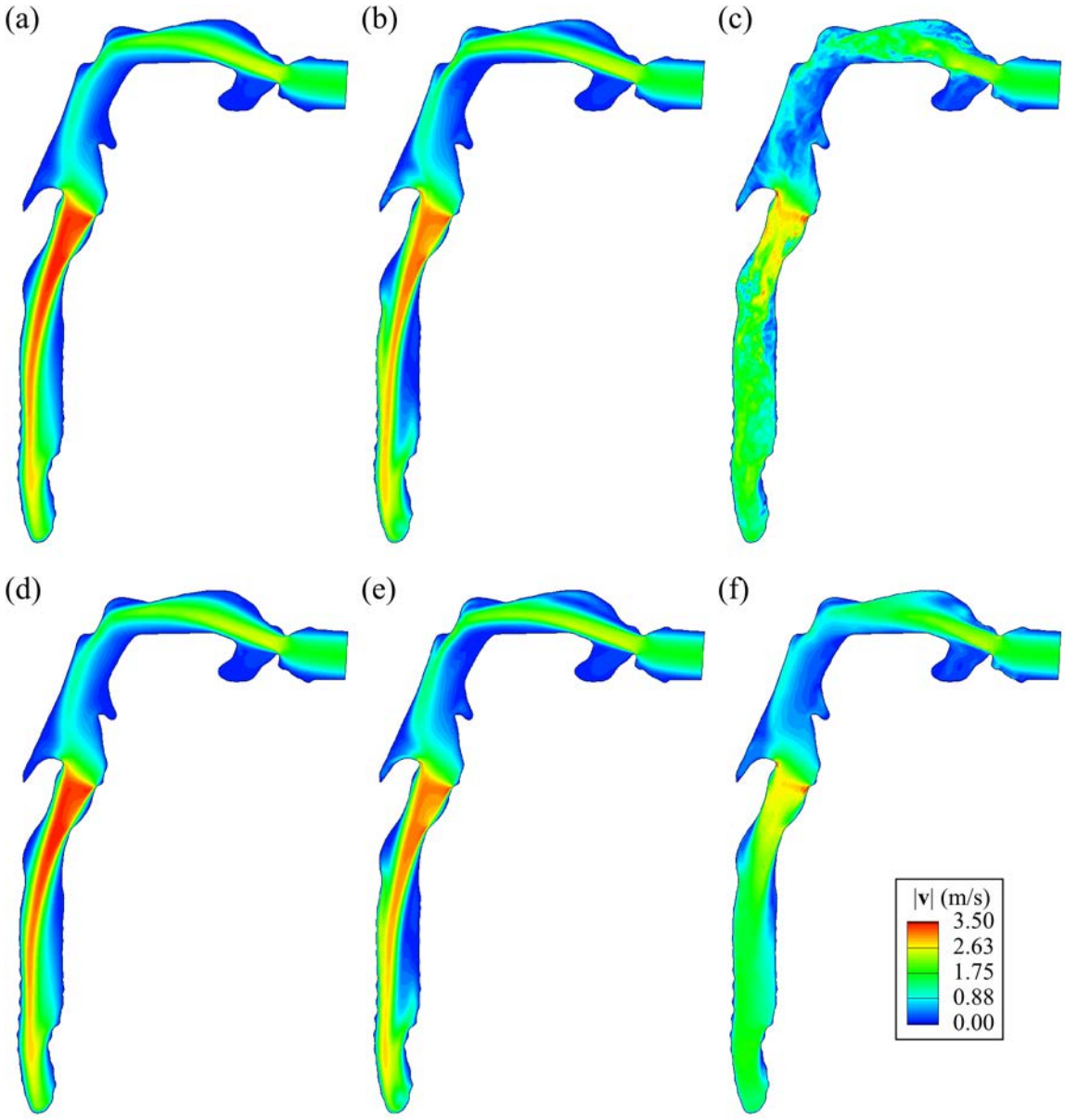

Figure 2.3: The instantaneous (at 2.16 s), (a)(c), and time-averaged, (d)(f), velocity magnitude (VM) $|\mathbf{v}|$ (m/s) distributions in a vertical plane cutting through the center of trachea looking from right: Re_t = (a)(d) 190 (He), (b)(e) 460 (He-O_2), (c)(f) 2800 (Xe-O_2).

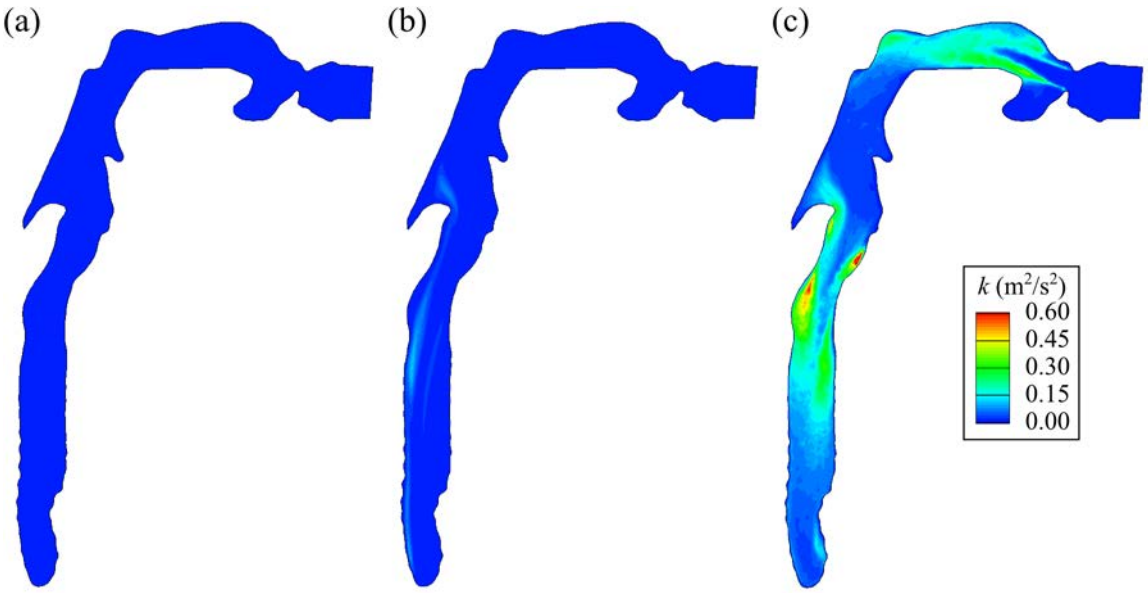

Figure 2.4: The turbulent kinetic energy (TKE) k (m^2/s^2) distributions in a vertical plane cutting through the center of trachea looking from right: Re_t = (a) 190 (He), (b) 460 (He-O_2), (c) 2800 (Xe-O_2).

which can also be confirmed by comparison of Figures 2.3a and 2.3d. For the cases of air (not shown) and Xe-O_2, the TKE is greatly amplified due to increased turbulent motions. The high TKE is mainly found in two regions: (i) the shear layer between the free stream and the open-cavity-like geometry near the top of the trachea, and (ii) the shear layer surrounding the jets in the oral cavity and the trachea.

Only for the case of He-O_2, the jets in the oral cavity and the trachea exhibit low-frequency oscillation due to the transitional nature of the flow. As a result of a spectral analysis, the period of this low-frequency oscillation was 0.36 s both in the oral cavity and the trachea. The instantaneous velocity field quantitatively resembles

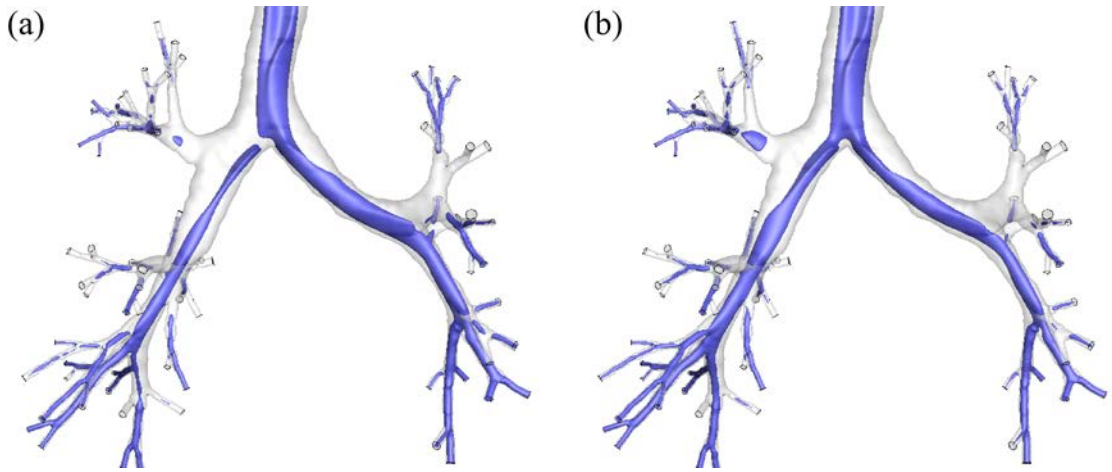

Figure 2.5: The iso-surfaces of the velocity magnitude at 1.75 m/s in the lower airways with the LR ventilation ratio of (a) 0.98 (He) and (b) 0.67 (He23).

the time-averaged velocity field (Figures 2.3b-2.3e), while the TKE is not negligible compared to Xe-O_2 (Figures 2.4b-2.4c): $\mathrm{TKE}_{\mathrm{max,He\text{-}O_2}} \sim \mathrm{TKE}_{\mathrm{max,Xe\text{-}O_2}}/6$. From the simulation results with He/O_2 = 85/15 and Re_t = 390, the flow remains laminar. Therefore, the flow becomes transitional as Re_t increases from 390 to 460. The critical Re_t for transition between laminar and turbulent flows ($\mathrm{Re}_{t,c}$) is approximately taken as 430.

The ratio of the cross-sectional areas $\mathrm{X_{LMB}}/\mathrm{X}_{RMB}$ is 0.72, so the bulk gas speed is higher in $\mathrm{X_{LMB}}$ with the given LR ventilation ratio of 0.98, resulting in a much larger high-speed region near the inner wall of the LMB than in the RMB (Figure 2.5a). In the He23 case, the LR ventilation ratio is 0.67, resulting in comparable bulk gas speeds in both LMB and RMB. As a result, the high-speed region in the RMB is nearly as large as that in the LMB (Figure 2.5b). Since the only difference between

the cases of He and He23 is the LR ventilation ratio, the flow fields in both cases are nearly identical before reaching the first bifurcation.

2.3.2 Regional Aerosol Distribution

Figure 2.6 shows that the aerosols are less dispersed in the He-gas laminar flow. In contrast, in the Xe-O_2-gas turbulent flow, the aerosols are already well mixed in the oral cavity and distributed uniformly when entering the trachea. In addition, the aerosols in the turbulent flow are transported more slowly along the axial direction of the airway than in the laminar flow. Figure 2.7 shows that more aerosols are advected first to the LMB and then to the RMB in the laminar flow (He), whereas nearly equal numbers of aerosols enter the LMB and RMB at the same time in the turbulent flow (Xe-O_2). In the steady laminar flow, there are two local peaks in the time history of particle flux to the RMB due to the complex flow field in the oral cavity, which is specific to this subject. It is noteworthy that the summation of the areas underneath the two curves in the laminar flow is the same as for the turbulent flow, because of using the same number of aerosols for both cases.

The peaks for both X_{LMB} and X_{RMB} at around 0.25 s in Figure 2.7a correspond to the cloud aerosols located on both sides of the upper trachea indicated by the two arrows in Figure 2.6a. The aerosols are already split into the two groups before entering the trachea due to the deflection of the flow against the wall in the oral cavity. For the case of He23 shown in Figure 2.7b, the aerosols are delivered to the LMB and RMB in a similar manner as for He, but the difference between the particle

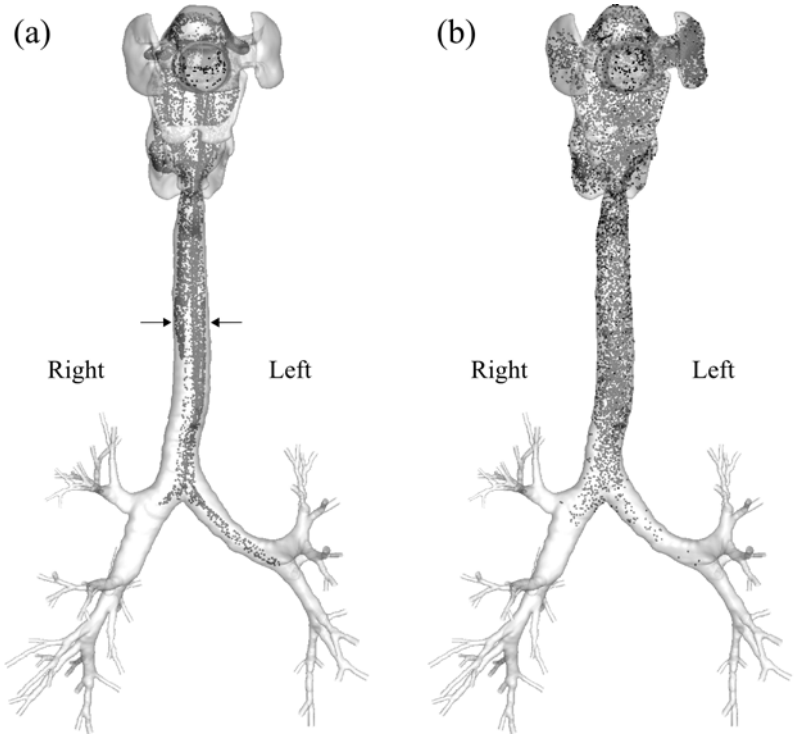

Figure 2.6: The instantaneous distributions of 2.5 μm-aerosols when the aerosols reached the second bifurcation in the left lung: (a) He at 0.195 s and (b) Xe-O_2 at 0.228 s after the release of the aerosols at the mouth, viewed from the front. The aerosols are released uniformly over the cross-section of the mouthpiece ($(r_i, r_o) = (0, r_m)$).

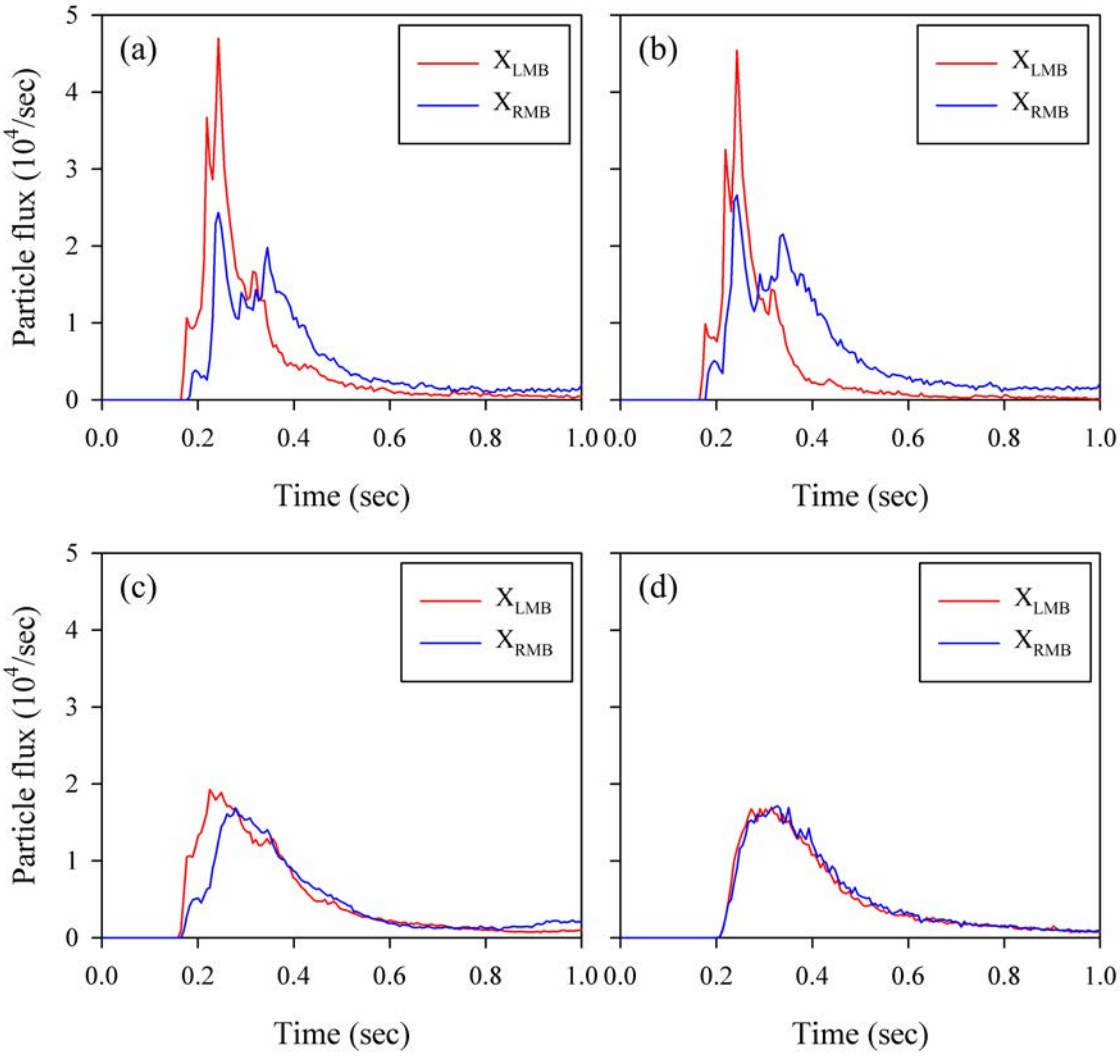

Figure 2.7: The time history of particle flux of 2.5 μm-aerosols at X_{LMB} and X_{RMB} in (a) He, (b) He23, (c) He-O_2, and (d) Xe-O_2. The aerosols are released uniformly over the cross-section of the mouthpiece ($(r_i, r_o) = (0, r_m)$).

fluxes to the respective LMB and RMB is smaller than that of the He case due to the lower LR ventilation ratio for the case of He23 (Figure 2.7b). In the particle flux profile for He-O_2 (Figure 2.7c) there is no sharp peak as observed in He and He23, but the profile for X_{LMB} is different from X_{RMB}, suggesting that aerosols in He-O_2 are not as well mixed as those in Xe-O_2. The particle flux profiles for air (not shown) and Xe-O_2 (Figure 2.7d) are similar to each other.

When the aerosols are released uniformly over the cross-section of the mouthpiece, the LR aerosol distribution ratios for the cases of He, He23, He-O_2, air, and Xe-O_2 are 0.99, 0.67, 1.01 $\pm$ 0.046, 1.00 $\pm$ 0.047, and 0.98 $\pm$ 0.046, respectively. The latter three cases include the standard deviations based on the results of multiple aerosol releases to account for the transition (He-O_2) and turbulence (air and Xe-O_2) effects. For the LR ventilation ratio of 0.98, the difference between the mean aerosol ratios in the laminar (He), transitional (He-O_2), and turbulent (air and XeO_2) flows is not statistically significant, and the aerosols entering the LMB and RMB are about the same. The uncertainty due to the transition and turbulence effects is less than 5% in He-O_2, air, and Xe-O_2. For the case of He23 with the LR ventilation ratio of 0.67, the aerosol distribution ratio nearly equals the corresponding ventilation ratio as in the He case.

When the aerosols are released only in the annular region between two radii r_i and r_o, the LR aerosol distribution ratio deviates from the corresponding ventilation ratio in the laminar (He) and transitional flows (He-O_2), whereas the LR aerosol ratio is nearly equal to the ventilation ratio in the turbulent flows (Xe-O_2 and air)

as shown in Figure 2.8. In the laminar flow, the distribution of the aerosol ratio is not monotonic, varying significantly between around 16 and 0.4. In the transitional flow, the deviation of the aerosol distribution ratio from the ventilation ratio is much smaller than that in the laminar flow, and the uncertainty is larger than that in the turbulent flow due to the low-frequency oscillation of the jets. In the turbulent flow, the uncertainty is greater when the aerosols are released near the center of the mouthpiece, perhaps due to their physical correlation with the turbulent jets in the core region of the airways. The shape of the distribution of the aerosol ratio for He23 is similar to that for He, but the average ratio for He23 is smaller than that for He due to the smaller ventilation ratio.

If aerosols are released randomly over the radius[51] as expressed below

$$r = \xi r_m, \tag{2.15}$$

then more aerosols are clustered near the center of the mouthpiece. This distribution differs from the uniform distribution given by Equation 2.2. With the aerosol distribution given by Equation 2.15, for the case of turbulent flow the LR aerosol distribution ratio still nearly equals the ventilation ratio, suggesting that the initial aerosol distribution does not affect the LR aerosol distribution. On the other hand, for the laminar flow the LR aerosol distribution ratio is 1.3, indicating that 30% more aerosols are advected to the LMB. This is consistent with the results described above. That is, for the case of laminar flow with the aerosol distribution given by Equation 2.15 at the mouthpiece, aerosols clustered near the center of the mouthpiece are more likely to be advected to the LMB as shown in Figure 2.8.

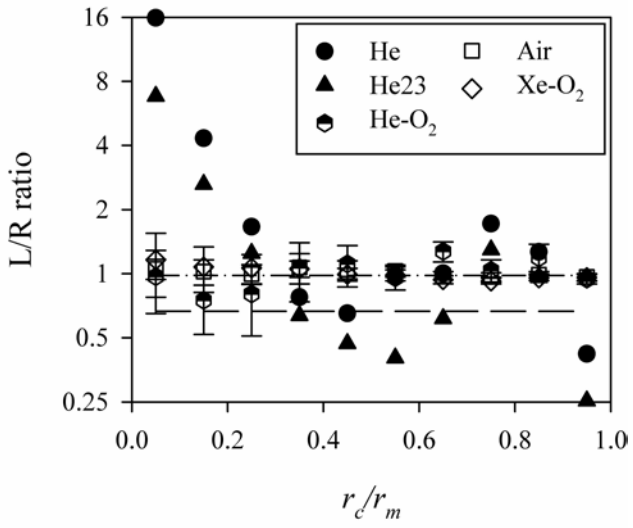

Figure 2.8: The LR aerosol distribution ratios as a function of the location of the aerosols at the mouthpiece r_c non-dimensionalized with the radius of the mouthpiece r_m. The dash-dot and dash lines represents LR ventilation ratios of 0.98 (He, He-O_2, air, Xe-O_2) and 0.67 (He23), respectively.

2.4 Discussion

The first objective of this study is to study the effect of carrier gas properties on aerosol transport and distribution for effective drug delivery in the human lung. Previous experimental and numerical studies have focused on the oral deposition, so the interest of this study is in the distribution of small (2.5 μm) aerosols in the intra-thoracic airways. The second objective of this study is to show the importance of the unsteady eddy-resolving CFD model to account for the turbulent laryngeal jet.

2.4.1 Effect of Gas Properties

Different gas properties result in different Re_t. If Re_t is lower than ~ 430, the flow is laminar, and small aerosols generally follow the steady streamlines of the flow (i.e. flow structures), which depend on airway geometry and regional ventilation. Thus, the release location of an aerosol at the mouthpiece determines its transport along the streamline that begins at the release location. Aerosols advected along different streamlines may experience different degrees of acceleration and deceleration. For example, in the He-gas laminar cases the aerosols first enter the LMB, and then enter the RMB as illustrated in Figure 2.7a. Furthermore, if small aerosols are uniformly distributed at the mouthpiece, the flow ventilation ratio basically determines the LR aerosol distribution ratio.

For the He-O_2 case of transitional flow, the jets in the oral cavity and the trachea exhibit low-frequency oscillation and can mix aerosols. For the cases of turbulent flow (air and Xe-O_2), inhaled small aerosols are well mixed in the oral cavity

and the trachea before entering the main bronchi LMB and RMB (Figures 2.7c-2.7d). Thus, regardless of the aerosol release location at the mouthpiece, the flow ventilation determines the LR aerosol distribution (Figure 2.8). The major difference between the laminar and turbulent flow cases is that turbulent structures mix aerosols in the oral cavity and trachea, and subsequently aerosol distribution does not depend on the release location at the mouthpiece. In contrast, for the case of laminar flow, the mixing of aerosols is absent, and flow ventilation would roughly match aerosol distribution only if the aerosols are uniformly distributed at the mouthpiece.

The critical Re_t of ~ 430 found in this study is lower than the critical Re of ~ 2300 for transition to turbulent flow in a straight pipe. It is because the turbulent flow in the trachea is caused by the airway constriction at the glottis, being a free-shear flow rather than a wall-bounded flow. Dekker[21] found experimentally that the critical flow rate for transition to turbulent flow in the trachea is 96 ± 26 mL/s with $\nu = 1.51 \times 10^{-5}$ m^2/s. Although Dekker[21] did not report the trachea diameter nor the critical Re_t, with the assumption[40] of $D_t = 16$ mm the critical Re_t is estimated to be 506 ± 137, which is close to the current critical Re_t. The uncertainty in the critical flow rate is due in part to its dependence on individual airway features (e.g., glottal constriction) and upstream flow disturbances.

2.4.2 Comparison with Other CFD Studies

Table 2.2 summarizes some related CFD studies. Except Jayaraju et al.[44], all of the listed studies used RANS models only. The other common feature in

these studies is that aerosols were released uniformly at the inlets of their respective airway models. RANS models predict time-averaged mean flow fields and turbulent statistics, e.g., TKE, without resolving any transitional/turbulent flow structures. Therefore, there are two common approaches used for prediction of aerosol trajectories on a RANS-predicted flow field. One approach uses the mean flow field only, being referred to as "mean flow tracking" (MFT). The other approach, known as "turbulent flow tracking" (TFT), employs an eddy interaction model (EIM)[33, 44] to introduce random turbulent fluctuations based on RANS-predicted TKE to the mean flow field.

MFT does not allow turbulent mixing of aerosols. Lagrangian tracking of particles in a RANS-predicted mean flow is numerically equivalent to tracking in a steady laminar flow, where aerosol trajectories depend on the aerosol release location. As a result, MFT cannot reproduce the release-location-independence feature of the aerosols in turbulent flows (Figure 2.8). Releasing aerosols uniformly at the model inlet may help dispersing aerosols in the absence of turbulent mixing.

TFT utilizes the predicted intensity and distribution of TKE, which depend on the RANSs limited ability to predict turbulent characteristics, e.g., free-shear flow vs. wall-bounded flow and isotropy vs. non-isotropy. Accurate prediction of turbulent features is crucial to reproduce preferential particle concentration in turbulent dispersed multiphase flow[3]. Jayaraju et al.[44] showed the accuracy of two unsteady eddy-resolving methods, detached-eddy simulation (DES) and LES, over RANS using both MFT and TFT. Kleinstreuer and Zhang[48] simulated the aerosol delivery in laminar to turbulent flows with TFT. Their results showed that the flow is laminar

Table 2.2: Comparison between the previous numerical studies about aerosol delivery in the human lung using Reynolds-Averaged Navier-Stokes (RANS) models.

	Airway	RANS	Particle	B.C.	Re_t	$Re_{t,c}$
Ma	Oral cavity	$k-\epsilon$	MFT	H[c]	1200	< 1200
and Lutchen[60]	Bronchioles		TFT		-4800[d]	
			(G)[b]			
Kleinstreuer	Oral cavity	LRN	TFT	NA	1200	1200
and Zhang[48]	Trachea	$k-\omega$			-4800[d]	-2400
Darquenne et al.[20]	Trachea	$k-\epsilon$	MFT	H	500	8000[e]
	Bronchioles				-2500[e]	
Jayaraju et al.[44]	Oral cavity	LRN	MFT	NA	2100	NA
	Trachea	$k-\omega$[f]	TFT			
			(G)			
Sandeau et al.[71]	Oral cavity	LRN	TFT	NA	280	400
	Trachea	$k-\omega$	(G)		-3100[g]	

[a] "RANS" is $k-\epsilon$ or low-Reynolds number (LRN) $k-\omega$ model. "Particle" is mean flow tracking (MFT) and/or turbulent flow tracking (TFT). "B.C." is the ventilation boundary condition (B.C.) at the ending branches. Re_t and $Re_{t,c}$ are the Reynolds and critical Reynolds numbers in the trachea, respectively.

[b] (G) = oral deposition efficiency is compared with that by Grgic et al.[34].

[c] H = Horsfield et al.[40].

[d] $D_t = 18$ mm is assumed[90].

[e] The values are obtained from their earlier paper[84].

[f] RANS is compared with detached eddy simulation (DES) and large eddy simulation (LES).

[g] The values are computed based on $Re_t = 400$ for airflow of 128 mL/s.

for Re_t = 1200 (airflow rate of 15 L/min) with the assumption35 of D_t = 18 mm, and the flow becomes turbulent when Re_t is 2400 (30 L/min). The estimated critical Re_t (between 1200 and 2400) is more than twice the ones found from the experiments by Dekker[21], the numerical simulations by Sandeau et al.[71] and the current study. In Kleinstreuer and Zhang[48], the maximum TKE in the trachea normalized by the trachea bulk velocity for Re_t of 1200 is underestimated by about three orders of magnitude as compared with Sandeau et al.[71] and the current study.

Darquenne et al.[20] reported that "ventilation defines the delivery of aerosol to lung segments" when small (0.5-, 1-, and 2-μm) aerosols are released uniformly at the trachea with air flow rate of 500 mL/s (Re_t = 2500). Their airway model is the only model that begins from the trachea without including the oral cavity and the larynx. Their earlier paper[84] reported no significant differences between the results predicted by laminar and RANS models and the critical Re_t of 8000, suggesting the importance of including the upper airway in the model. Although their finding about the aerosol distribution agrees with the current study, this work further indicates the dependence (independence) of aerosol distribution on the aerosol release location in laminar (turbulent) flow.

Ma and Lutchen[60] found that the oral deposition predicted by MFT agrees better with Grgic et al.[34] than that by TFT. On the contrary, Jayaraju et al.[44] showed that TFT predicts more accurate oral deposition compared to MFT. The difference between them may be attributable to the differences in their airway and RANS models. Ma and Lutchen[60] used MFT to predict the LR aerosol deposition

ratio of greater than unity, which was also found by Lambert et al.[51] using LES with a different airway model and ventilation boundary conditions.

2.4.3 Potential for Targeted Drug Delivery

The relationship between the aerosol distribution ratio and the aerosol release location at the mouthpiece in laminar flows could potentially be used for better localized targeting in drug delivery. In practice, the Re can be reduced to stabilize the flow not only by increasing the kinematic viscosity as in the current study, but also by decreasing the flow rate[34]. With a lower flow rate, the inhalation should last longer to keep the same tidal volume. Ross and Schultz[70] suggested that the dry powder inhaler (DPI) requires relatively high flow rate to create "respirable" aerosols, whereas the metered dose inhaler (MDI) does not. Although some patients, especially children, cannot use MDI correctly[19], the MDI is more suitable for the inhalation with low flow rate. Because DPI devices have rapidly been being improved[23, 74], new technology may enable DPI to generate fine aerosols with lower flow rate.

According to Martonen[62], the tidal volume and frequency of the representative breathing pattern for resting conditions are 500 mL and 14/min, which correspond to the period of 4.29 s, resulting in an average flow rate of 233 mL/s. If heliox (80%He-20%O2, $\nu = 4.95 \times 10^{-5}$ m^2/s) is selected as a carrier gas, the Re$_t$ is 375 with the assumption of $D_t = 16$ mm. As stated above, the main objective of this paper is to show the effect of gas properties on aerosol distribution, and He gas is used mainly to show the lower end of the kinematic viscosity range. However, according to the

above estimate, the Re_t based on the average flow rate of heliox for the resting breathing condition is lower than the critical Re_t. Therefore, it is still possible to produce a laminar flow condition, although it can be challenging to generate micro-particles with this flow rate.

Even if the Re_t is lower than the critical Re_t so that the flow is laminar, the relationship between aerosol distribution and release location may still depend on Re_t due to the complex geometry of the upper airways. Nonetheless, once the relationship for the individual with a given Re_t (lower than the critical Re_t) is known, the mouthpiece could be modified to optimize drug delivery. For the subject considered here, most of the small aerosols located near the center of the mouthpiece enter the left lung, so more aerosols can be delivered to the left (right) lung by releasing the aerosols near (away from) the center.

The advantage of the flow with Re_t higher than the critical Re_t is that the aerosols are delivered to the lung following the ventilation, so detailed information concerning the airway geometry is not needed. The ventilation can be estimated by using the image registration-derived boundary conditions. However, the Re_t should not be too high because (i) the tracheobronchial airway resistance increases almost linearly with increasing Re_t and (ii) the difference in aerosol delivery by differing carrier gases is small if the flow becomes turbulent.

CHAPTER 3
AUTOMATIC CONSTRUCTION OF MULTISCALE HUMAN AIRWAY MODELS INCLUDING TRIFURCATIONS

3.1 Introduction

The geometric models of branching tubular structures can be applied to medical education, virtual reality (VR) operating planning, augmented reality (AR) interoperative support, and numerical simulations of blood vessel and airway trees[85, 35, 76, 80]. One of the approaches to modeling branching structures is the centerline (CL)-based modeling. The CL-based models reconstruct the three-dimensional (3-D) geometry of a branching tubular structure from the one-dimensional (1-D) tree that contains the information about the skeleton and diameters of branches. The 1-D tree of the central airway can be extracted from a 3-D image, e.g., computed tomography (CT) image. The volume-filling technique[81] can generate anatomically-consistent 1-D trees of peripheral airway that cannot be resolved by CT scanning.

The CL-based models have been applied to visualizing and analyzing blood vessel trees. To visualize the surface of vascular structures around liver, brain, and heart, researchers have used a piecewise smooth subdivision surface generator that smooths an intermediate "base mesh" constructed with a recursive branching-construction procedure[25, 85, 92]. This method provides smooth and topologically correct surface meshes of n-furcation branching tubular structures using their 1-D trees, but the surface meshes were not used for numerical simulations of blood flow and blood vessel structure. To analyze vascular structures, Zhang et al.[96] used

hexahedral solid NURBS (Non-Uniform Rational B-Splines). In their process called vascular modeling pipeline, a variety of smooth n-furcation branching tubular structures are reconstructed with appropriate cross-section and branching templates for each mapped meshable region, and each circular cross-section is projected onto the image-based geometry for more realistic non-circular cross-section. However, the algorithm for automatic selection of appropriate templates was not presented.

The CL-based models have been also applied to constructing airway geometry. A number of CL-based models of symmetric airway trees with one or two generations have been used, but they do not capture the asymmetric nature of the human airway trees[40]. Several CL-based models of asymmetric airway trees with more than a few generations have been constructed from the 1-D trees (e.g., [84, 31, 83, 88]. Some of these 1-D trees were based on the "average" anatomical models proposed by Horsfield et al.[40] and Yeh and Schum[94]. These asymmetric models, however, do not account for inter-subject variability, which is an important step toward individual medicine. The subject-specific models are typically built manually from image data with image-processing tools. The CL-based modeling of airway trees (e.g., [80]) aims to automatically construct the 3-D airway geometries that incorporate subject-specific skeleton and branch diameters.

Marchandise et al.[61] developed a method to automatically construct image-based geometries using surface geometry as input, but one cannot use their method to create the surface geometry of artificial 1-D trees, e.g., for the region unresolved by CT. Lin et al.[55] presented the computational framework to automatically construct

the subject-specific CL-based geometry extending from the glottis to terminal bronchioles for computational fluid dynamics (CFD) analysis of pulmonary airflow. This geometry includes the anatomically-consistent artificial 1-D tree of the branches that cannot be resolved by CT for investigation of the "paths of interest". This model does not account for trifurcations, which can be found in the central airway of the human lung (e.g., [2, 99]). Therefore, the objective of this study is to develop an algorithm that can automatically construct 3-D geometric models of airway trifurcations in the human lung using the 1-D tree as input.

In this study, we extended the existing CL-based model[80] to account for trifurcations. In the existing model, the cross-section of a non-branching segment is defined by four "ring nodes", and the cross-section of a bifurcation is defined by the four ring nodes and one "crux node" responsible for the geometry around a carina, i.e., five nodes. As the existing model constructs a bifurcation by adding one crux node to a non-branching segment, the new model should be able to construct a trifurcation by adding another crux node, "left" or "right crux node", to one of the two child branches at the bifurcation. Furthermore, the new model can avoid intersection and twist of surfaces by using the additional crux node in two ways, resulting in two types of trifurcations ("fork-type" and "tripod-type") as explained later. Therefore, it is expected that the new model can automatically reconstruct the geometry of trifurcations whose overall geometric feature is captured in the framework of the existing bifurcation model.

This chapter is organized as follows. First, we describe the details of the CL-

based model: (i) segmentation to obtain the CT-based model, (ii) skeletonization to extract 1-D tree from the CT-based model, and (iii) geometry reconstruction to create the CL-based model. Second, we compare the CL-based model with the corresponding CT-based model. Finally, we discuss the characteristics, quality, and potential improvement of the new CL-based model.

3.2 Methods

The 3-D CL-based geometric airway model of the human lung consists of branches; a branch is surrounded by four quadrilateral curved surfaces; a quadrilateral curved surface is defined by four curves; and a curve is defined by two control nodes (CNs). At a CN the direction of the curves connected to the CN is defined in addition to the location of the CN. An end of the branch is defined by four curves connecting four CNs called ring nodes. If the branch has one, two, or three child branches (at straight airway, bifurcation, trifurcation), the bottom of the parent branch needs to have one, two, or three sets of ring nodes, respectively, to which the child branches are attached. One, two, and three sets of ring nodes can be defined by four, five, and six CNs, respectively, and there are two ways to define three sets of ring nodes using six CNs. The CNs are obtained by mapping the "generic CNs" that are defined in the local coordinate system aligned with the branch. The local coordinate system is defined by the skeleton. The original skeleton can contain straight airways, bifurcations, and trifurcations. If two consecutive bifurcations are very close to each other, the double bifurcation is considered as single trifurcations. The original and added

trifurcations are called intrinsic and extrinsic trifurcations. To avoid the surfaces intersecting each other or twisted, the trifurcations need to be classified into at least two types.

We constructed the CL-based model, following three main steps: generation of 1-D tree, CNs, and 3-D geometry. First, we extracted a 1-D tree from CT lung volume image data. Second, we used the 1-D tree to generate the CNs. Third, we used the CNs to create the curves and surfaces of the CL-based model. The second step includes the main difference between the existing and proposed algorithms, and this section is mainly devoted to the explanation of the second step. The second step consists of five sub-steps: definition of coordinate systems, definition of CNs for straight airways, definition of CNs for bifurcations, identification and classification of trifurcations, and definition of CNs for trifurcations.

3.2.1 Healthy and Severe Asthmatic Subjects

To develop the CL-based model, we used the CT images of 25 healthy and severe asthmatic (SA) subjects: 1 healthy subject acquired through the Biomedical Research Partnership (BRP) study and investigated in previous studies[14, 63, 95]), and 8 healthy and 16 SA subjects randomly selected from the data set acquired through the Severe Asthmatic Research Program (SARP). The Institutional Review Board at the University of Iowa and the University of Pittsburg approved the associated human studies along with the imaging protocol. We used the SARP subjects to determine the parameters for identification and classification of trifurcations, and the

BRP subject to discuss the error in the CL-based model and to create the geometry of the airways that are not resolved by CT.

3.2.2 1-D Tree

We extracted (segmented) the 3-D airway geometry from the CT image data, and we skeletonized the CT-based geometry to obtain the 1-D tree by using a commercial software package Apollo (VIDA). We extended the 1-D tree from the resolution limit of the CT images to the end of conducting airways by applying the volume-filling method[81] to the original 1-D tree. As a result, we obtained the 1-D tree extending from the trachea to the end of conducting airways. The 1-D tree needs to extend from the trachea to glottis when gas flow is simulated to account for the laryngeal jet[54, 13]. The 1-D tree data obtained with Apollo includes the coordinates of branching points, average diameter of branches, and generation number of branches. Apollo uses the thinning algorithm proposed by Palágyi et al.[68] to obtain the 1-D tree. The volume-filling method does not create trifurcations, so the generated 1-D tree does not include intrinsic trifurcations.

3.2.3 Coordinate System

A skeleton consists of centerline nodes (CLNs) and CLs, which connect the CLNs; and each branch consists of two CLNs and one CL in the CL-based model. The direction of CL is positive in the direction of increasing airway generation. We used the CLNs and CLs to map the generic CNs by translation and rotation. Two CNs can define a curve by specifying the directions of the curve, e.g., cubic Hermite

spline function[26], and four curves can define quadrilateral surface elements. The number of generic CNs should be minimized to reduce the complexity of the model. The generic CNs need to be mapped not only to avoid the surfaces intersecting each other but also to minimize the twist of the surface elements.

The generic CNs are defined in the local coordinate system in each branch, called branch coordinate system ($oxyz$), and they were mapped to the global coordinate system ($OXYZ$) by rotation and translation. The origin of $oxyz$ is the first CLN of the branch (Figure 3.1). The direction of z-axis is the same as the direction of the branch CL. The directions of x- and y-axes are defined to minimize the twist of the surface elements. To minimize the twist, we determined the direction of y-axis using the directions of the bifurcations around the branch. If the segment is not a child branch of the previous bifurcation, e.g., the trachea, the nearest bifurcation in positive CL direction was used (Figure 3.1b). If the segment is a child branch of the previous bifurcation as well as the parent branch of the following bifurcation, which is the case for most of the segments, both bifurcations were used (Figure 3.1c). If there is no bifurcation in the positive CL direction, i.e., ending branches, the nearest bifurcation in negative CL direction was used (Figure 3.1b). The method to obtain bifurcation directions is explained in Appendix A.1.

3.2.4 CNs for Straight Airways

The ending branches are straight airways, which have zero or one child branch. The generic CNs for a straight airway consist of four ring nodes: right, front, left,

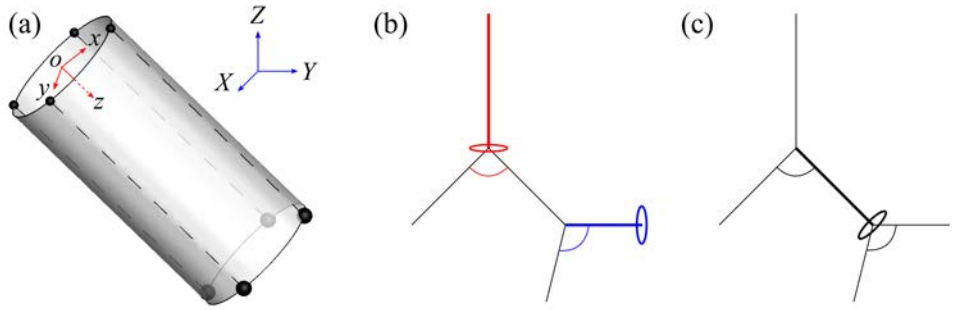

Figure 3.1: (a) The definition of global ($OXYZ$) and branch ($oxyz$) coordinate systems. The bifurcations that are used to determine the direction of y-axis at (b) a branch that does not have neighboring bifurcations in negative centerline (CL) direction (red), a branch that does not have neighboring bifurcations in positive CL direction (blue), and (c) a branch that have neighboring bifurcations in both negative and positive CL directions (black).

and back nodes (Figure 3.2). The (x, y)-coordinates of the four ring nodes are $(R, 0)$, $(0, R)$, $(R, 0)$, and $(0, R)$, respectively, where R is the branch radius. The z-coordinate of the ring nodes is 0 or L around the first or second CLNs, respectively, where L is the length of the segment. The two nearest ring nodes, e.g., right and front nodes, are connected with an s_1-curve, i.e., there are four s_1-curves around each CLN and eight s_1-curves in each branch (Figure 3.2a). A ring node around the first CLN is connected to the nearest ring node around the second CLN by an s_2-curve, i.e., there are four s_2-curves in each branch (Figure 3.2a). Two s_1-curves and two s_2-curves compose a quadrilateral surface element, i.e., there are four surface elements in each branch (Figure 3.2a). The method to obtain the directions of s_1- and s_2-curves is

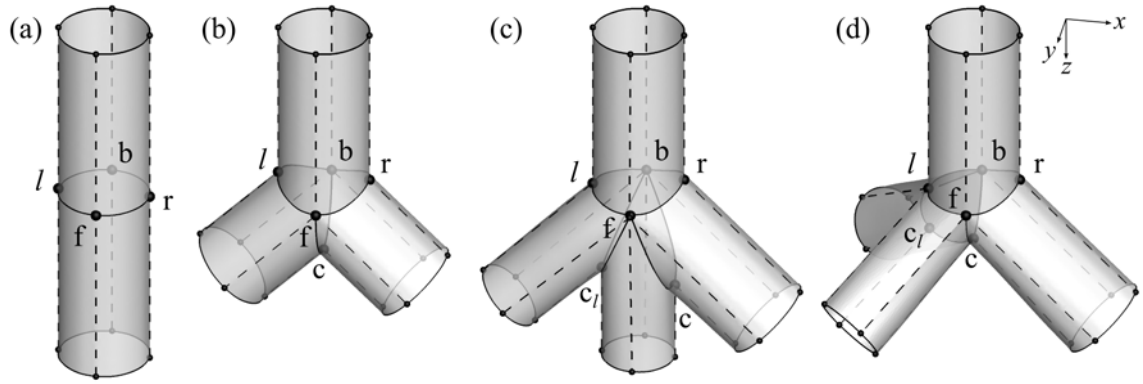

Figure 3.2: The generic control nodes (CNs) for a (a) straight airway, (b) bifurcation, (c) fork-type trifurcation, and (d) tripod-type trifurcation. The larger black nodes indicate the generic CNs of interest, and r, f, l, b, c, and c_l denotes right, front, left, back, crux, and left crux nodes, respectively. The solid and dashed curves are s_1- and s_2-curves, respectively. The left child branch was replaced with its child branches to form the trifurcations (c) and (d). The arrows labeled with x, y, and z indicate the positive directions of the x-, y-, and z-axes in the first segment of each geometry.

explained in Appendix A.2.

3.2.5 CNs for Bifurcations

Most of the branches are bifurcations, which have two child branches. The generic CNs for a bifurcation consist of four ring nodes and one crux node, which defines the geometry around the carina of the bifurcation (Figure 3.2b). The (x, y)-coordinates of the ring nodes are the same as those for the straight airway except for that R is defined as $R = 0.5\,[R_p + max\,(R_{c1}, R_{c2})]$, where R_p is the radius of the parent branch and R_{ci} is the radius of the i^{th} child branch. Tawhai et al.[80]

empirically obtained this formula. The z-coordinate of front and back nodes are the same as those for the straight airway, while the z-coordinate of right (left) node is the minimum of L and the one at the intersection of parent and right (left) child branch assuming both branches are cylindrical. The (X, Y, Z)-coordinates of the crux node is the one at the intersection of the child branches assuming they are cylindrical.

The ring nodes around the first CLN of a child branch correspond to one of the two sets of ring nodes around the second CLN of the parent branch: right-front-crux-back (right) and crux-front-left-back (left) rings (Figure 3.2b). The two child branches were connected to the two rings of the parent branch in a way that avoids the intersection of the child branches. The ring nodes around the first and second CLN of each child branch were connected in a way that minimizes the twist of surface elements. The surface elements are not twisted (s_2-curves are ideal) in Figure 3.2b because the child branches are not bifurcations. The method to obtain the directions of s_1- and s_2-curves (Figures 3.3a-3.3c) is explained in Appendix A.3.

3.2.6 Identification and Classification of Trifurcations

Trifurcations can be hidden among the bifurcations of 1-D trees. At a bifurcation one of the child branches can be so short in 1-D tree that the branch can be included in the following bifurcation in the corresponding 3-D geometry. In this case, the short child branch was replaced with its child branches, i.e., grandchild branches, to form an extrinsic trifurcation. We judged whether the child branch is short or not using the ratio of the distance between the crux node and the cross-section at the

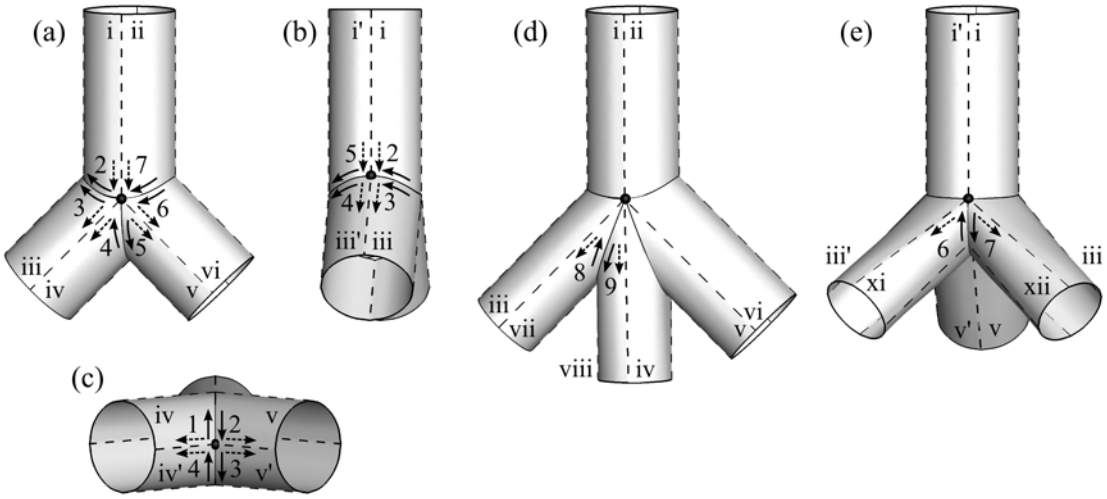

Figure 3.3: The versions of directions of s_j-curves at the (a) front, (b) left, and (c) crux nodes for a bifurcation, and at the (d) front node of a fork-type trifurcation and (e) left node of a tripod-type trifurcation. The black node indicates the node of interest. The Roman number denotes the index of a surface element, and the Arabic number denotes the index of a version. The solid and dashed curves are s_1- and s_2-curves, respectively, and the solid and dashed arrows indicate the directions of the s_1- and s_2-curves, respectively.

second CLN of the child branch (L') to the radius of the child branch (R), i.e., L'/R (Figure 3.4a). If L'/R is zero or negative, the branch is completely included in the following bifurcation. If L'/R is positive but small, the quality of resulting surface is not good (Figure 3.4b). We empirically found the threshold value for L'/R. If both child branches are short or consecutive child and grandchild branches are short, our trifurcation model cannot be used. Intrinsic trifurcations can be considered as a special type of extrinsic trifurcations whose L is zero. An intrinsic trifurcation was converted to double bifurcation by inserting a short dummy branch, which was eventually removed by applying the criterion to make extrinsic trifurcation.

We classified trifurcations into two types by topology. We extended the bifurcation model to a trifurcation model by splitting one of the child branches into left and right child branches (fork-type) (Figure 3.2c). We found that the surfaces of child branches intersect each other or they are severely twisted at some trifurcations where three child branches are far from coplanar. Therefore, we constructed another type of trifurcation model by splitting one of the child branches into front and back child branches (tripod-type) (Figure 3.2d). We quantified the difference between the two topologies using the angles between child branches: $r_{\theta 123} = \theta_{13}/(\theta_{12} + \theta_{23})$, where θ_{12}, θ_{13}, and θ_{23}, where θ_{kl} is the angle between the k^{th} and l^{th} child branches (Figures 3.5a-3.5b). At an intrinsic trifurcation, the order of child branches is defined as described in Appendix A.1. At an extrinsic trifurcation, the original child branch that has not been replaced is the first child branch, and the original grandchild branch that is closer to the first child branch by angle is the second child branch (Figure

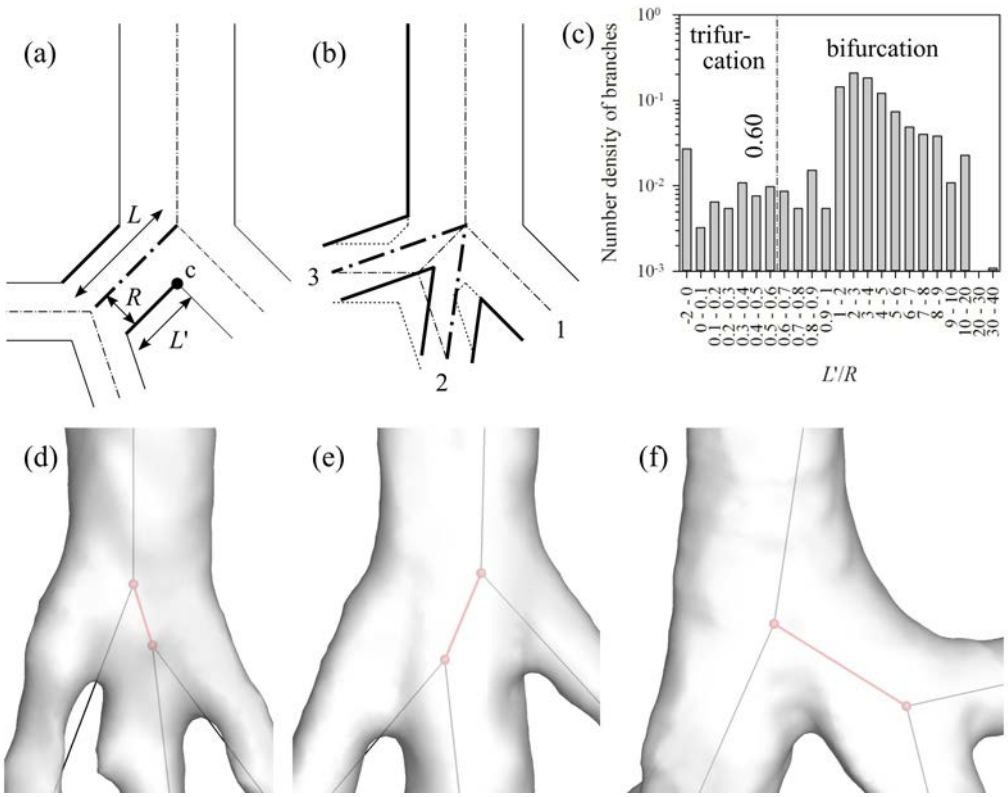

Figure 3.4: (a) The definition of parameters used to identify trifurcations, and (b) the trifurcations when a left child branch is too short. (c) The histogram of L'/R, and the child branches corresponding to (d) negative L'/R ($= -0.37$), (e) L'/R ($= 0.24$) below 0.6, and (f) L'/R ($= 0.95$) above 0.6. In (a) and (b), solid lines are the airway walls, and the dash-dotted lines are the centerlines. In (a) node c is crux node, and L is the length of the left branch, L' is the distance between the crux node and the cross-section at the second centerline node (CLN) of the left child branch, and R is the radius of the left child branch. In (b) dotted lines are the airway walls of the original bifurcation, and 1-3 show the order of child branches at the trifurcation. In (c) the number density is based on 921 central branches in 24 SARP subjects. In (d)-(f), the red spheres and lines show the location of CLNs and centerlines (CLs) of interest, respectively.

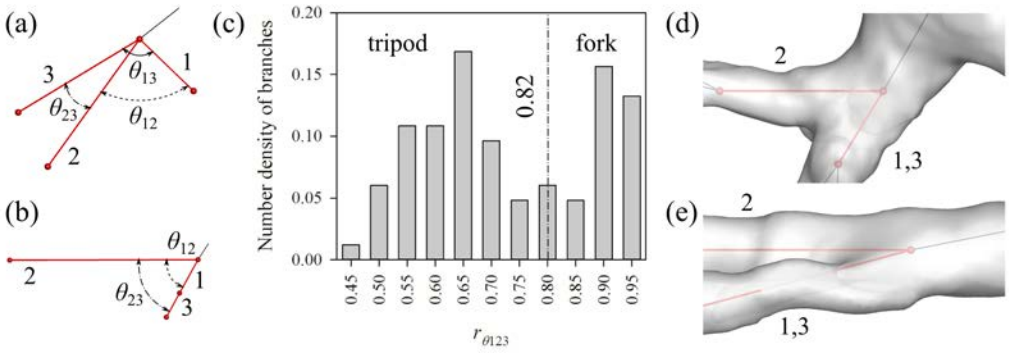

Figure 3.5: The definition of parameters used to classify trifurcations looking from (a) an arbitrary direction and (b) a direction parallel to the plane defined by the first and third child branches. (c) The histogram of $r_{\theta 123}$, and the trifurcations corresponding to (d) $r_{\theta 123}$ (= 0.61) below 0.82 and (e) $r_{\theta 123}$ (= 0.89) above 0.82 looking from a direction parallel to the plane defined by the first and third child branches. θ_{kl} is the angle between k^{th} and l^{th} child branches. $r_{\theta 123} = \theta_{13}/(\theta_{12} + \theta_{23})$ of 1.0 and 0.5 correspond to perfect fork- and tripod-type trifurcations, respectively. In (a)-(b) and (d)-(e), black and red lines show the centerline of parent and child branches, respectively, and 1-3 show the order of child branches at the trifurcations. In (c), the number density is based on 83 trifurcations in 24 SARP subjects.

3.4b). If $r_{\theta 123}$ is 1.0, the three child branches are coplanar to form a perfect fork-type trifurcation. If $\theta_{12} = \theta_{23} = \theta_{13}, r_{\theta 123} = 0.5$ and the branching is a perfect tripod-type trifurcation.

3.2.7 CNs for Trifurcations

The generic CNs for a trifurcation consist of four ring nodes and two crux nodes, i.e., the crux node for the bifurcation and right or left crux (second crux) node. The second crux node can be used in two ways to construct the two types of trifurcations. One of the two sets of ring nodes around the second CLN of the parent branch can be split into two sets of ring nodes in two ways by using the second crux node. For example, if the left child branch is too short and is replaced with its child branches, the second crux node is the left crux node. If the trifurcation is fork-type (Figure 3.2c), the left ring around the second CLN of the parent branch, crux-front-left-back nodes, is split into left crux-front-left-back and crux-front-left crux-back nodes, to which left-left and left-right child branches are attached, respectively. If the trifurcation is tripod-type (Figure 3.2d), the left ring of the parent branch is split into crux-front-left-left crux and crux-left crux-left-back rings, to which left-front and left-back child branches are attached, respectively.

We determined the coordinates of the CNs for trifurcations in a similar way to bifurcations. The coordinates of the ring nodes are basically the same as those for the bifurcation, but not the crux nodes. For a fork-type trifurcation, we determined the coordinates of the two crux nodes using the two nearest child branches, assuming they are cylindrical. For a tripod-type trifurcation, whose child branches are right, left-front, and left-back child branches, we determined the coordinates of the left crux node by using the left-front and left-back child branches, and the coordinates of the crux node is the average of the two intersections: the one between right and left-front

child branches and the one between right and left-back child branches. The method to obtain the directions of s_1- and s_2-curves (Figures 3.3d-3.3e) is explained in Appendix A.4.

3.2.8 Summary of CNs

We determined the coordinates of the CNs and the directions of s-curves in $OXYZ$ by rotation and translation of $oxyz$. First, we determined the coordinates of the ring nodes and the directions of s-curves at the ring nodes in $oxyz$, and we mapped them to the branch in $OXYZ$ by rotation and translation. Second, we determined the coordinates of the crux nodes in $OXYZ$ by using the information about the child branches. Third, the directions of s-curves at some CNs were improved or determined for ring nodes or crux nodes, respectively, in $OXYZ$ by using the coordinates of the CNs and the directions of child branches.

3.2.9 Construction of 3-D Model

We constructed the 3-D geometry, s-curves and surface elements, using the node and surface element information. The node information consists of the coordinates and the directions of s-curves at the CNs, and the surface element information consists of element connectivity in terms of node indices and s-curve versions. In this study, the curves and surfaces are defined by the spline curves and ruled surfaces on an open source program Gmsh[32]). We added three CNs to each s-curve to draw the spline curve on Gmsh using cubic Hermite spline function[26]). The coordinates of the CNs including the additional ones, s-curve connectivity, and surface element con-

nectivity are the input data required for Gmsh to construct the geometry. It should be noted that we replaced the information about the s-curve directions with the additional CNs on the curves, i.e., we discretized the continuous s-curves with additional CNs. We determined the optimum number of additional CNs by minimizing the data size and by maximizing the smoothness of the curve.

3.3 Results

3.3.1 Identification and Classification of Trifurcations

We applied the CL-based model to 24 SARP subjects to empirically determine the threshold values for L'/R and $r_{\theta 123}$, which are used to identify and classify trifurcations, respectively. The threshold value for L'/R was 0.60 based on visual inspection of the CT-based geometry of 921 central branches in 8 healthy and 16 severe asthmatic (SA) SARP subjects (Figure 3.4c). This means that the extrinsic trifurcation in this model is defined as the bifurcation where one of the child branches has L'/R of less than 0.60. For instance, we judged that the child branches in Figures 3.4d ($L'/R = 0.37$) and (e) ($L'/R = 0.24$) are short and that the child branch in Figure 3.4f ($L'/R = 0.95$) is not short. We used this criterion to find 83 trifurcations, 2 quadfurcations (four child branches) and 1 pentfurcation (five child branches). The number of quadfurcations and pentfurcations were rare ($< 5\%$) compared to the number of the trifurcations. The threshold value for $r_{\theta 123}$ was 0.82 based on visual inspection of 83 trifurcations in the 24 subjects (Figure 3.5c). For instance, we judged that the trifurcations in Figure 3.5d ($r_{\theta 123} = 0.61$) and (e) ($r_{\theta 123} = 0.89$) should be

tripod-type and fork-type trifurcations, respectively, to minimize the twist of surface elements.

Trifurcations were uniformly distributed in central branches. We identified the extrinsic trifurcations in the central airways of the 24 SARP subjects using the criterion: $L'/R < 0.60$. Every subject had at least one trifurcation, and the average number of trifurcations was 3.5 per subject: 1.4 fork-type and 2.1 tripod-type trifurcations. There was at least one branching point with more than two child branches in every lobe (Figure 3.6a). More than 50% of the subjects had trifurcations between the second- and third-generation branches in right lung, and more than 30% of the subjects had trifurcations between the third- and fourth-generation branches in left lung (Figure 3.6a). There was a fork-type trifurcation before right intermediate bronchus in 46% of the subjects (Figure 3.6b). There was a tripod-type trifurcation at right upper lobar bronchus in 79% of the subjects, and there was a tripod-type trifurcation at left upper division bronchus in 46% of the subjects (Figure 3.6c).

3.3.2 Trifurcations in Proximal Region

We applied the CL-based model to the BRP subject to compare the CL- and CT-based models. There were five intrinsic trifurcations in the 1-D tree. It took a few seconds to automatically reconstruct the 3-D CL-based geometry using the 1-D tree of the BRP subject. Based on the definition of trifurcations (Figure 3.4), we found two extrinsic trifurcations and one extrinsic quadfurcation. The narrowest child branch of the quadfurcation was removed to make a trifurcation because our CL-

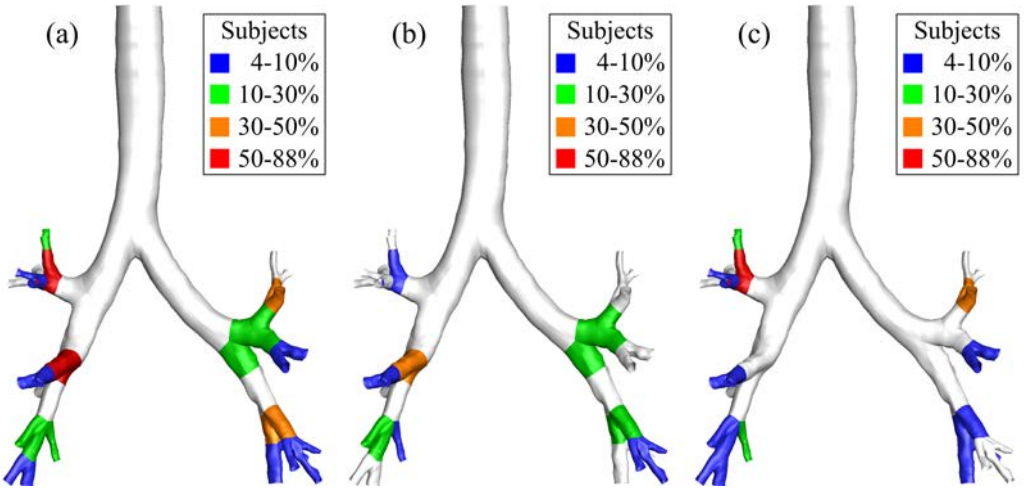

Figure 3.6: The distribution of (a) branching points with more than two child branches (including 2 quadfurcations and 1 pentfurcation), (b) fork-type trifurcations, and (c) tripod-type trifurcations in central branches in 24 SARP subjects.

based model does not account for qudfurcations. This trifurcation is not included in the analysis hereafter. The criterion to classify the trifurcations was applied to the six trifurcations, and two and four trifurcations were classified as fork- and tripod-type trifurcations, respectively (Figures 3.7).

The tripod-type trifurcations in the CL-based geometry were overall consistent with those in the CT-based geometry. At the tripod-type trifurcation in RUL (Figures 3.7c-3.7d), the directions of airways and the diameters at the end of child branches were consistent between the CL- and CT-based models. Intersections and severe twist of surfaces were not found in the child branches. The parent branch in the CT-based geometry was thicker than that in the CL-based geometry, because the cross-section in the former was elliptical rather than cylindrical as in the latter. The

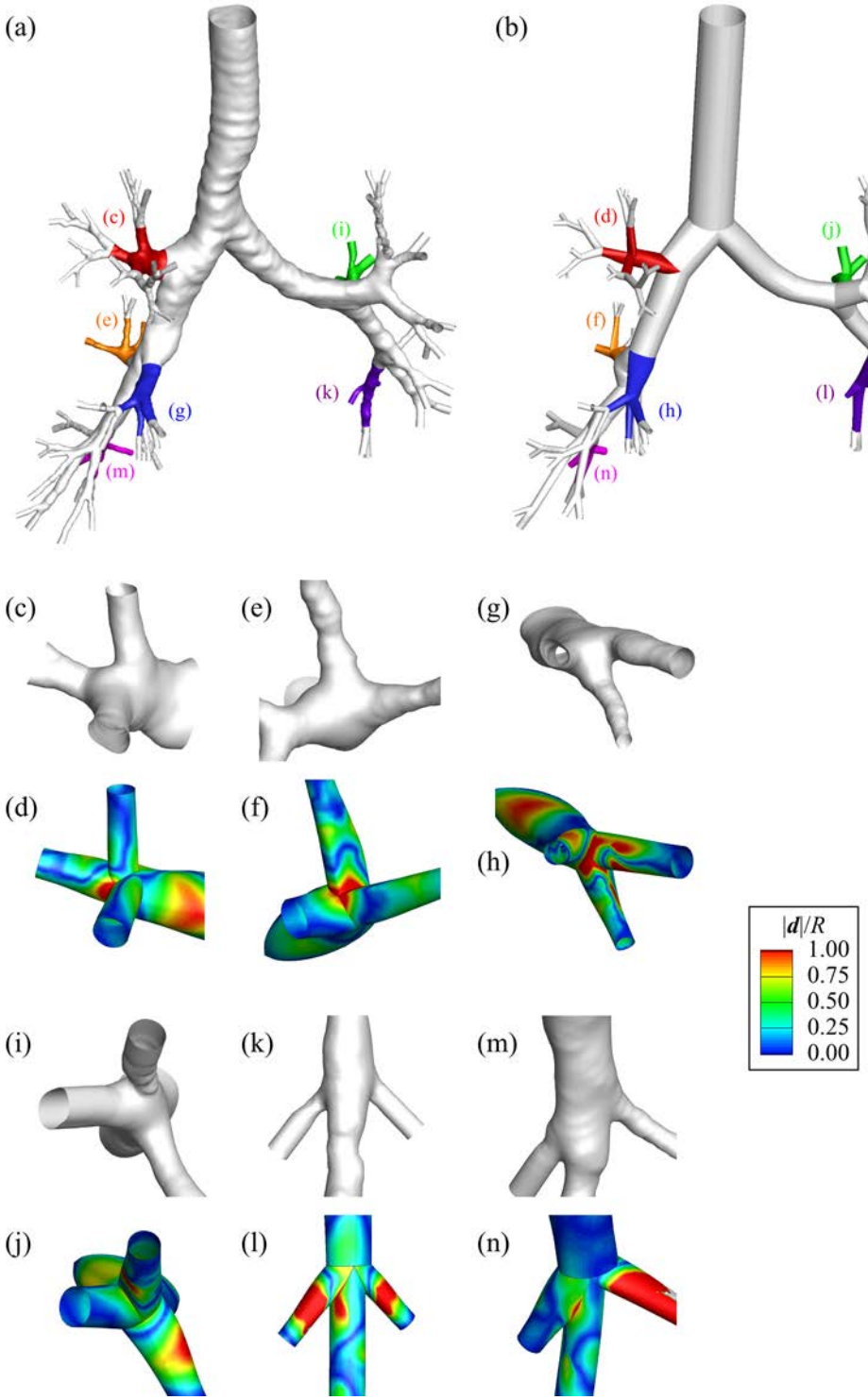

Figure 3.7: The (a) computed tomography (CT)- and (b) centerline (CL)-based geometric models of trifurcations. **d** is the radial distance between the surfaces in CT- and CL-based models, and R is the branch radius.

carina in the CT-based geometry was larger and smoother than that in the CL-based geometry. This is because the crux node was determined with the assumption that child branches are cylindrical.

The overall geometric features of fork-type trifurcations in the CT-based geometry was also captured in the CL-based geometry. At the fork-type trifurcation in LLL (Figures 3.7k-3.7l), the angles between airways and the diameters at the end of airways in the CL-based geometry were consistent with those in the CT-based geometry. The surfaces were not intersecting each other, and there was no severe twist of surfaces. The diameter of the left most child branch near the branching point in the CL-based geometry was larger than that in the CT-based geometry, and the local constriction of the middle child branch in the CT-based geometry was not captured in the CL-based geometry. This is attributed to that each branch was defined by the cross-sections at both ends.

We tried to quantify the difference between the CL- and CT-based models by measuring the distance between the two surfaces. It was difficult to measure the distance because the CL was not straight in many of the branches in the CT-based model. Nevertheless, we tried to measure the radial distance between the two surfaces, and normalized the radial distance by branch radius. The average normalized radial distance for the entire airway was about 0.25, i.e., on average the radial distance in a branch was about 25% of radius. The radial distance was large near the carina at the tripod-type trifurcations in RUL (Figure 3.7c-3.7d) and at the middle of left most child branches at the fork-type trifurcations in LLL (Figure 3.7k-3.7l), which is

consistent with the results from the qualitative comparison. The average normalized radial distance for the child branches were 0.30 and 0.52 at the tripod-type trifurcation in RUL and the fork-type trifurcation in LLL, respectively.

3.3.3 Trifurcations in Peripheral Region

We used the CL-based model to construct the 3-D geometry of the branches from the trachea to the end of terminal bronchioles. We applied the volume filling method to the 1-D tree of the CT-resolved branches for the BRP subject to generate the 1-D tree of the conducting airways that were not resolved by CT (Figure 3.8a). To clearly show the CL-based model of the CT-resolved and generated branches, we selected the paths to every lobe (Figure 3.8b). The highest generation in the paths to LUL, LLL, RUL, RML, and RLL were 18, 19, 16, 22, and 16, respectively. The maximum generation number of the conducting airway was larger than the maximum number of 16 in Weibel's model[90] along the paths to LUL, LLL, and RML, but it should vary depending on the path and subject. We used the extracted and generated 1-D tree to automatically reconstruct the CL-based model of the selected branches in every lobe (Figure 3.8b). There were four short child branches in the generated branches, so the generated branches included four trifurcations.

3.4 Discussion

3.4.1 Trifurcations in Human Lung

Trifurcations were found in the central branches of the human lung. We found at least one trifurcation in every subject considered, while trifurcations have not been

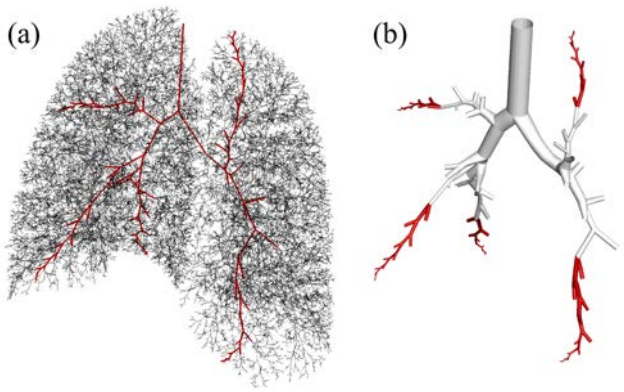

Figure 3.8: The paths of interest in conducting region: (a) 1-D tree, (b) CL-based geometry. In (a), red lines indicates the centerlines of the paths of interest. In (b), the centerlines of the red airways were artificially generated using the volume filling method[81].

considered in the previous studies that used the geometric model of the human lung with more than a few generations (e.g., [84, 31, 83, 88]). In the present study we found trifurcations at left upper division bronchus, left lower lobar bronchus, right upper lobar bronchus, and before intermediate bronchus, in 46%, 33%, 88%, and 50% of the 24 healthy and SA SARP subjects considered, respectively. This means that it was not possible to create the 3-D airway geometry of central branches in these subjects without using the trifurcation model. Furthermore, if a geometric model does not account for trifurcations in the central airways, the higher generation airways attached to the trifurcations cannot be included in the model. We also found that artificial higher-generation branches selected in this study included short child branches to form trifurcations. Therefore, trifurcation model is crucial to create the

geometric model of branches not only in proximal region but also peripheral regions.

The results is the present study overall agrees with a previous study. We found trifurcation at the left upper division bronchus in 25% (2/8) of the healthy SARP subjects considered, which agrees well with the observation by Boyden[7] and Zhao et al.[99] who found trifurcation at the same branch in 27% (27/100) and 23% (50/216) of the subjects, respectively. We found trifurcations at the left lower lobar bronchus in 38% (3/8) of the healthy SARP subjects considered, while Zhao et al.[99] found trifurcation in the same region in 18% (39/216) of the subjects. We found trifurcation at the right upper bronchus in 88% (7/8) of the healthy SARP subjects considered, while Boyden[7] found trifurcation in the same region in 46% (23/50) of the subjects. The difference between the present study and the previous studies may be caused by the criteria to define trifurcations and the number of subjects considered. Both the present and previous studies agree on that right upper lobar bronchus, left upper division bronchus, and left lower lobar bronchus are the preferential locations of trifurcations among the central branches. We did not find the abnormal branches at the first branching[2].

3.4.2 Trifurcation in CL-based Model

We classified the trifurcations in the airway tree of the human lung. To avoid the surfaces intersecting each other or twisted, we classified the trifurcations into at least two types by topology: fork- and tripod-type trifurcations. At fork-type trifurcations, three child branches were close to coplanar, but they are not at the

tripod-type trifurcations. We quantified the topological difference using the angles between three child branches, and we empirically determined the threshold value to classify the two types of trifurcations. This classification is different from that by Zhao et al.[99] who classified the branching patterns by combination of child branches. The topology of fork- and tripod-type trifurcations are similar to that of the particular Type II branching patterns in LLL and LUL whose geometries are shown in their paper, respectively, but this does not mean the classifications in this paper and Zhao et al.[99] are interchangeable. The overall geometric features of trifurcations in the CL-based geometry were consistent with those in the CT-based geometry. We needed at least two types of trifurcations to reconstruct the overall geometrically consistent trifurcations in the central branches of healthy and SA subjects.

We quantitatively defined the extrinsic trifurcation hidden in a 1-D tree. In a 1-D tree there can be any bifurcations, but some double bifurcations have to be considered as trifurcations in 3-D geometry because the airway has diameter. When a child branch of a bifurcation in the 1-D tree was too short, the double bifurcation (the bifurcation and following bifurcation) was converted to an extrinsic trifurcation. The extrinsic trifurcation is empirically defined as the bifurcation where directional distance from the carina to the end of child branch is smaller than 60% of its radius including negative distance. The reconstructed bifurcations and extrinsic trifurcations captured overall geometric features of the central branches in the CT-based geometry. The criterion to identify the extrinsic trifurcations hidden in the 1-D tree was empirically found to reconstruct the overall geometrically consistent central airway

tree of a healthy subject.

We quantified the difference between the CL- and CT-based geometry. The objective of this study is to include trifurcations in the CL-based model for 3-D visualization of 1-D trees, rather than developing the most accurate geometric model. However, we estimated the geometric error in the CL-based model so that we can compare it with the errors in more accurate models in the future. The average normalized radial distance between the central branches of the CL- and CT-based models was about 0.25, and 0.37 for the child branches of trifurcations. The error in the CL-based model seems large, but we think they are reasonable because the CL is straight and radius is nearly uniform in each branch of the CL-based model.

3.4.3 Potential Improvements

The proposed geometric model can be improved in several ways. The 3-D geometry reconstructed in this study captures overall geometric features of 3-D geometry for 3-D visualization of 1-D trees, but the geometry needed to be refined when the geometry is used for, e.g., numerical simulation of aerosol distribution in the human lung. The glottis needs to be attached above the trachea to reproduce the laryngeal jet, and airway cross-section should be modified using the CT-images to obtain non-circular cross-sections (hybrid CL-CT-based geometry). If the airway with non-circular cross-section is split into multiple sub-segments, sub-segment scale geometric features, e.g., bend and constriction, can be captured and the transition between parent and child branches becomes smoother. The proposed trifurcation model

can be extended to quadfurcation model by splitting another child branch into two. The thinning algorithm proposed by Palágyi[68] produces a significantly smaller number of spurious branches compared to the other methods, but some spurious branches still need to be removed manually to obtain the 1-D tree. The whole procedure to reconstruct a 3-D CL-based geometric model from CT images will be more efficient if the skeletonization becomes more accurate.

CHAPTER 4
AUTOMATIC MESHING OF IMAGE-BASED HUMAN AIRWAY MODELS FOR NUMERICAL SIMULATION OF DRUG DELIVERY

4.1 Introduction

A better understanding of the regional distribution of aerosols in the human lung helps to improve targeted delivery of pharmaceutical drugs to the regions of interest in aerosol therapy[6]. Numerical (*in silico*) models based on computational fluid dynamics (CFD) are commonly used for the study of pulmonary aerosol delivery with different subjects, body postures, breathing patterns, carrier gases, inhalers, and aerosol types. Subject-specific airway geometry for CFD is essential to account for inter-subject variability. However, it is time-consuming to pre-process image-based geometry and post-process the gas-flow and aerosol data obtained from the simulations, because airway geometry is complex. The pre-process includes construction of geometry, generation of a CFD mesh, and specification of boundary conditions. The post-process mainly involves aerosol counting in the regions of interest, e.g., branches in certain generation or lobe.

A number of researchers presented geometric airway models without describing automated procedures for constructing the geometry (e.g., [84, 31, 83, 88]). Tawhai et al.[80] proposed a method to automatically construct the three-dimensional (3-D) geometry using the skeleton and diameters of branches in the one-dimensional (1-D) tree. This 3-D geometry is a collection of branches corresponding to their respective branches in the 1-D tree. Thus, we can use the anatomic information about the airway

obtained from the 1-D tree such as branch connectivity and dimension to facilitate pre- and post-process data. This method can represent the airway branch-scale geometry (e.g., direction and diameter), although sub-branch-scale geometry (e.g., bend and constriction) and diameter-scale geometry (e.g., cartilage rings) are simplified and trifurcation geometry is not represented. Later we improved this method to account for trifurcations (Chapter 3). However, these geometries have not been used for CFD simulations of aerosol delivery in the human lung. Marchandise et al.[61] proposed a method to automatically construct the geometry, but each sub-zone (patch) did not correspond to each branch in the 1-D tree. As a result, the pre- and post-process could be time-consuming.

The CFD mesh for the airway geometry has been manually generated with mesh-generation programs in most of the previous studies (e.g., Lin et al.[54]), but the mesh can be automatically generated. For example, in the CL-based geometric model proposed by Tawhai et al.[80], each branch is represented by a cylinder-like surface, which can define the volume for a 3-D CFD mesh. The optimal mesh size in the volume can be roughly determined by the diameter and flow rate in the branch (e.g., Yin et al.[95]). An open source mesh-generation program Gmsh[32] can automatically generate the mesh using the mesh size at control nodes (CNs) as input data. Therefore, the 3-D airway geometry can be automatically discretized seamlessly from the trachea to the terminal bronchioles. Furthermore, boundary conditions on the top, bottom, and side wall surfaces of the cylinder-like volume can be systematically specified. The objective of this study is to numerically predict the regional aerosol

distribution in the human lung using the automatically constructed and meshed 3-D human airway geometry.

For visualization purposes, airway models only need to capture branch-scale geometric features, thus, CL-based cylinder-like geometry is sufficient (Chapter 3). For aerosol simulations, however, sub-branch geometric features are important because aerosol transport is sensitive to flow structures in central airways, and flow structures depend on local geometric features such as airway cross-sectional shape, transition between a parent and child branches, airway bend, and constriction. To make CL-based geometry more realistic, a hybrid CL-CT-based model can fit CL-based geometry to CT-based geometry (e.g., [80, 96]). Glottal constriction is responsible for the unsteady and turbulent laryngeal jet, which plays important roles in gas-flow and aerosol delivery in the human lung (e.g., [54, 13, 63]). Most of CT images do not include the geometry of extrathoracic (mouth-larynx) region to reduce radiation exposure, but the approximate laryngeal model can be developed from the data in the literature, e.g., Cheng et al.[12] and Choi et al.[13], and CT images. Therefore, we expect that the simulations with the airway geometry automatically constructed and meshed with the hybrid model provide accurate regional aerosol distribution on airway-branch scale.

The rest of the chapter is organized as follows. First, we describe technical detail of the method to automatically construct and mesh image-based subject-specific airway geometry. Second, we compare the prediction of aerosol deposition by the CL-based and hybrid models with that of CT-based model. Finally, we discuss the

performance, advantages, and potential improvements of the geometric model.

4.2 Methods

The numerical simulation of aerosol transport in the human lung consists of four major steps: construction of geometric model, generation of CFD mesh, gas-flow simulation, and aerosol simulation. We added the geometric laryngeal model to the model proposed in Chapter 3, and we improved the CL-based model using CT image to construct the hybrid CL-CT-based model. In the hybrid model the CL is not straight and the cross-section is not circular and not uniform in each branch. To automatically generate the CFD mesh, we used an open-source mesh-generation program Gmsh[32]. To compute the mesh size in each cross-section, we used the local flow rate. We extracted the boundary meshes for each branch to specify the boundary conditions in the gas-flow simulation and to post-process the results from the aerosol simulation. To use the geometric laryngeal model, we modified the inlet boundary condition in the gas-flow simulation. We used the CL connectivity to efficiently post-process the results from the aerosol simulation.

4.2.1 Geometric Human Airway Model

The CL-based geometric airway model proposed in Chapter 3 consists of branches; the inner wall of each branch consists of four quadrilateral surfaces; each quadrilateral surface is defined by the four curves (two s_1-curves perpendicular to CL and two s_2-curves parallel to CL); each curve is defined by two end nodes (location of CNs and directions of s-curves at the CNs); the cross-section is defined by four CNs

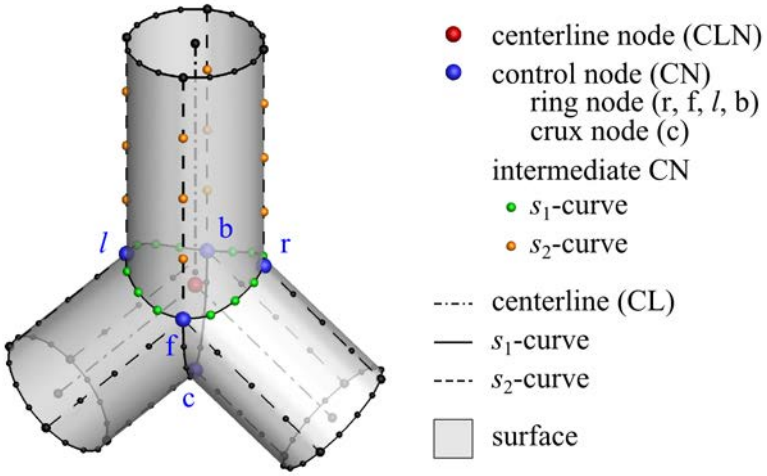

Figure 4.1: The definition of nodes, curves, and surfaces of the centerline-based geometric airway model ([80], Chapter 3).

called ring nodes; the geometry of bifurcations or trifurcations is defined by one or two more CNs called crux nodes, respectively; the CLs of neighboring branches are connected at centerline nodes (CLNs); and each curve is discretized by adding three more intermediate CNs (Figure 4.1).

4.2.2 3-D Hybrid CL-CT-based Model

We modified the CL-based model using CT image to construct the hybrid CL-CT-based model. In the CL-based model, each branch is straight and its cross-section is basically circular and uniform. To obtain non-straight branches, non-circular cross-section, and non-uniform cross-section in the CT-resolved region, we fitted the CL-based model to the CT image following the four main steps: (i) fit CLs, (ii) fit ring nodes, (iii) fit right, left, and crux nodes, and (iv) fit intermediate CNs (Figure 4.2).

We present the four steps below.

To fit CLs, we first inserted CLNs to make sub-branches, and then estimated the location of inserted CLNs using CT image. A branch can be curved, and a part of the straight CL can be even outside the branch (Figure 4.2a). To obtain the curved CL, we inserted sub-branches whose aspect ratio is close to one, where aspect ratio is defined as the ratio of length to diameter. The aspect ratio should not be too small so that the cross-sections along a curved airway segment do not intersect each other. At each CLN, we used the clustering algorithm DBSCAN (Density Based Spatial Clustering of Applications with Noise)[24] to distinguish the triangular elements of the CT-based airway surface around CLN from the elements around the CLNs of neighboring branches. The extracted surface elements are used to estimate the location of fitted CLN. The resulting geometric model with curved CL and circular cross-section is called the uniform hybrid CL-CT-based model.

To fit ring nodes, we used the fitted CLNs. Since surface fitting requires fitting direction, we used the fitted CLNs and the ring nodes in the uniform hybrid model to obtain the fitting direction (Figure 4.2b). The ring nodes can be used to obtain non-circular cross-section. The location of a fitted ring node is the intersection of the CT-based surface and the line defined by the fitted CLN and the ring node in the uniform hybrid model. The direction of s_1-curves at the fitted ring node is the direction in the uniform hybrid model projected on the plane whose normal vector is the average normal vector of four triangular elements around the fitted ring node.

To fit right, left, and crux nodes at bifurcations and trifurcations, we searched

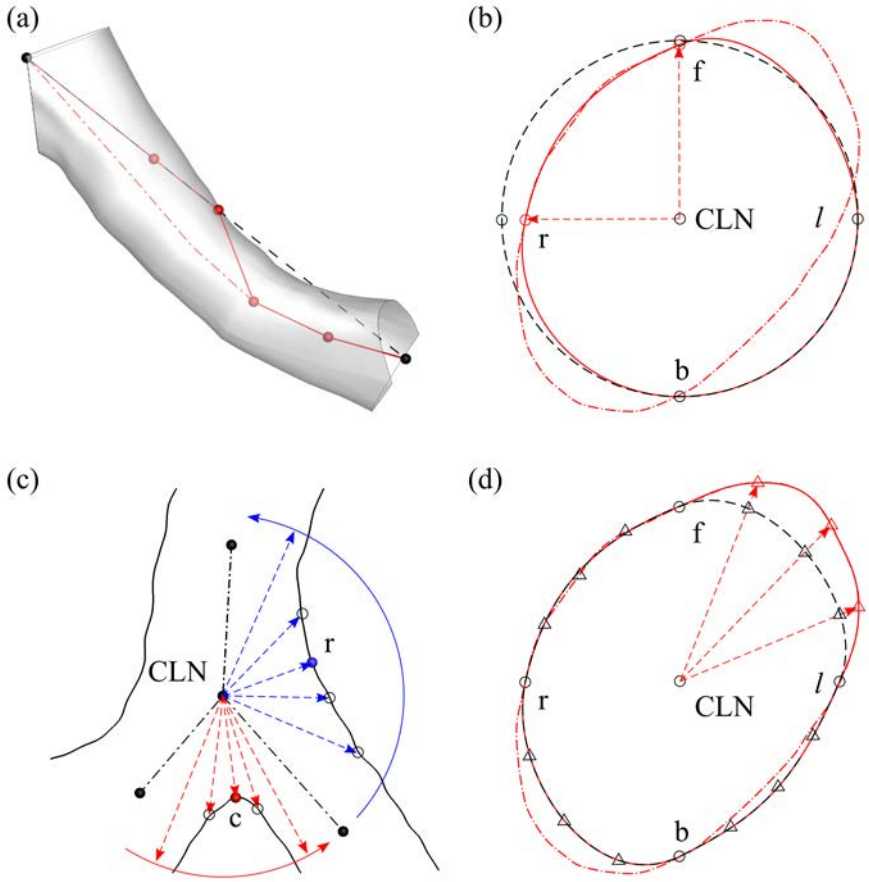

Figure 4.2: The fitting of (a) centerline nodes (CLNs), (b) ring nodes, (c) right, left, and crux nodes, and (d) intermediate control nodes (CNs) to computed tomography (CT)-based geometry. "r", "f", "l", "b", and "c" are the right, front, left, back, and crux nodes. The black dash-dotted lines and solid curves show centerlines and inner wall, respectively. The black dashed lines and curves show the geometry before fitting. The solid and dash-dotted red curves show partially and fully fitted geometry, respectively, and the arrows show the fitting directions.

for the point on the CT-based surface closest to the fitted CLN. For example, by definition, a crux node is always located between two child branches, so the directions of the two child branches can be used to find the crux node (Figure 4.2c). For explanation purposes, there are four searching directions in Figure 4.2c, but actual number of searching directions is larger than the number of triangular elements between the two child branches. For example, to find the searching directions for the right node, we used the direction of the right child branch and the direction of the parent branch projected on the plane defined by the two child branches (Figure 4.2c).

To fit the intermediate CNs, we used the fitted CLN and ring nodes. In Chapter 3, we discretized an s-curve with three intermediate CNs to draw the s-curve on Gmsh[32] (Figure 4.2d). The intermediate CNs can be used to further improve the quality of the hybrid CL-CT-based model. The location of a fitted intermediate CN on an s_1-curve is the intersection of the CT-based surface and the line defined by the fitted CLN and the original intermediate CN. To fit an intermediate CN on an s_2-curve, we used the original intermediate CN projected on the fitted CL. The resulting geometric model with curved CL and non-circular cross-section is called the non-uniform hybrid CL-CT-based model.

4.2.3 Geometric Laryngeal Model

We extended the 1-D tree from the trachea to larynx using the information about the trachea. CT data usually do not include the region above the trachea because of the negative effect of CT scan on the subjects. From the fluid mechanical

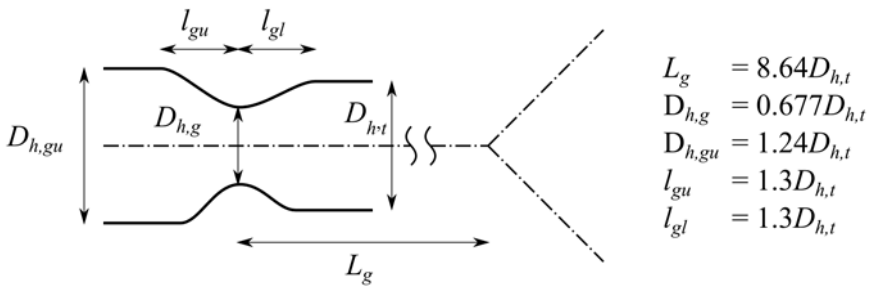

Figure 4.3: The definition and the values of the parameters to construct the geometric laryngeal model. The hydraulic diameter of the trachea $D_{h,t}$, the location of the glottis L_g, the (hydraulic) diameter at the glottis $D_{h,g}$, the (hydraulic) diameter above the glottis $D_{h,gu}$, the length of upper part of the glottis l_{gu}, and the length of lower part of the glottis l_{gl}.

point of view, glottal constriction plays a crucial role in creating turbulent laryngeal jet during inhalation[54, 63]. Therefore, the geometry around the larynx needs to be artificially generated. The geometry of larynx obviously varies subject to subject, so our goal is to make an approximate laryngeal model that can create realistic level of turbulence in the trachea. We modeled the geometry of larynx using five parameters: location of the glottis L_g, (hydraulic) diameter at the glottis $D_{h,g}$, (hydraulic) diameter above the glottis $D_{h,gu}$, length of the larynx above the glottis l_{gu}, and length of the larynx below the glottis l_{gl} (Figure 4.3). We normalized the five parameters with the hydraulic diameter of trachea $D_{h,t}$, e.g., $L_g^* = L_g/D_{h,t}$, so that the parameters can be applied to different subjects in the future.

To empirically determine the five parameters, we used the data in the literature

and the CT image of healthy subjects. We mainly used the data reported by Cheng et al.[12] and the CT image of two healthy subjects. The Institutional Review Board approved the associated human studies along with the imaging protocol. Cheng et al.[12] did not report the inflation level, while the inflation level for the CT image of the two healthy subjects were near total lung capacity. There is no precise definition of the beginning of trachea, and CT image would not necessarily start from the beginning of trachea even if there was such a definition. The nearest benchmark that is included in most of CT images is the first bifurcation, so we empirically determined the distance between the glottis and first bifurcation L_g^*. Since Cheng et al.[12] did not report the distance, we obtained the distance from the data reported by Choi et al.[13]. We plotted the distribution of D_h^* around the larynx to empirically determine $D_{h,g}^*$ and $D_{h,gu}^*$, and to empirically determine l_{gu}^* and l_{gl}^* by manually fitting the cubic Hermite spline curve[26] provided $D_{h,g}^*$ and $D_{h,gu}^*$ are the ones determined earlier.

4.2.4 CFD Mesh Generation

We automatically generated the CFD mesh using Gmsh[32]. On Gmsh, mesh size can be specified at each CN. Gmsh determines the mesh size on curves, on surfaces, and in volumes interpolating mesh sizes at neighboring CNs. The Reynolds number of the pulmonary flow is not very high ($\sim$ 1000-2000) in the trachea, so we distributed the grid uniformly in the cross-section. The image registration of two CT images can predict the flow rate in each branch[95]. We used the flow rate to determine the mesh size so that the mesh size in every airway is similar to each other

in terms of wall unit. To compute the mesh size in a cross-section of branch D_b, we used the following equation:

$$\Delta_b = min\left(\Delta_t\sqrt{\frac{D_b^3}{r_{Q,b}D_t^3}}, \frac{D_b}{6}\right), \tag{4.1}$$

where Δ_t is the mesh size in the trachea, D_t is the trachea diameter, D_b is the branch diameter, and $r_{Q,b}$ is the ratio of branch to trachea flow rate. Equation 4.1 is derived in Appendix B assuming laminar flow, and we determined Δ_t so that the mesh size is comparable to the thickness of viscous sub-layer in the trachea, where flow is the most turbulent. We also used about 30% smaller Δ_t, but the predicted flow field and aerosol deposition were not sensitive to Δ_t. The mesh size Δ_b is not greater than $D_b/6$ to guarantee the accuracy of the flow field.

We extracted the boundary and volume meshes for each airway to specify the boundary conditions in the gas-flow simulation and to post-process the results from the aerosol simulation. To have one volume for one branch, which makes it easy to post-process the data from aerosol simulations, we merged sub-branch volumes. The CFD mesh for each branch consists of top, bottom, and side boundary meshes and one volume mesh. The top and bottom are internal boundary in most of branches, while they can be external boundary in beginning and ending branches. To guarantee the mesh consistency on the internal boundaries, we first generated the boundary mesh for the whole geometric model using Gmsh. Then, we generated the volume mesh branch by branch in parallel by running multiple Gmsh simultaneously. The resulting CFD mesh for the whole geometric model consists of boundary and volume meshes for each branch. It was easy to specify the boundary conditions in the gas-flow simulation and

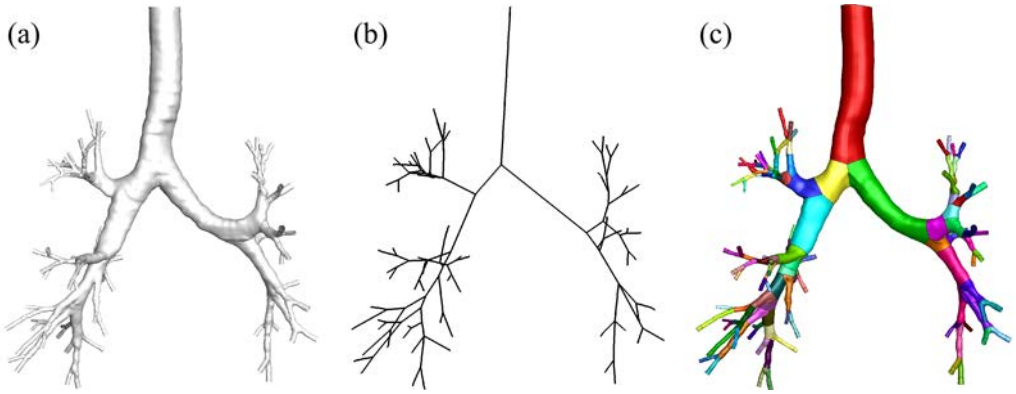

Figure 4.4: (a) The surface of computed tomography (CT)-based model, (b) skeleton, and (c) surface of non-uniform hybrid centerline(CL)-CT-based model.

to count the number of aerosols passing through the internal or external boundaries for each segment in the aerosol simulation, because the boundary and volume meshes are consistent with the branches in 1-D tree (Figure 4.4).

4.2.5 Gas Flow Simulation

To reproduce the air flow in the numerical human airway model, we used the large eddy simulation (LES) model validated by Lin et al.[53] and Choi et al.[13]. For comparison purposes, the breathing pattern was the same as that used by Miyawaki et al.[63], i.e., steady inspiratory flow rate of 342 mL/s ($\sim$ 20 L/min) for a time period of 2.16 sec. The Reynolds number at the trachea Re_t was about 1300. We imposed a turbulent flow above the glottis as explained later, the laminar parabolic flow at the end of the model as in Yin et al.[95], and no-slip boundary condition on the airway wall.

4.2.6 Inlet Boundary Condition

We fed a homogeneous isotropic turbulent flow above the glottis to use the approximate laryngeal model. The flow becomes turbulent in the oral cavity and the time-averaged velocity profile is nearly uniform over the cross-section above the glottis when the parabolic laminar flow is fed at the mouth piece[13]. It is known that the turbulence of the flow upstream of a constriction greatly affects the characteristics of the jet downstream of the constriction. A turbulent flow with uniform time-averaged velocity profile needs to be fed above the glottis if the geometric model does not include the extrathoracic region. The geometry of the larynx was unknown and approximated, so using isotropic turbulent flow is the best approximation.

To reproduce the homogeneous isotropic turbulent flow above the glottis, we used the synthetic eddy method (SEM) proposed by Jarrin et al.[43]. The SEM is one of the simplest methods to reproduce synthetic turbulent flows that have correlation in time and space. The SEM does not require a 3-D turbulent flow field a priori, but instead reproduces synthetic turbulence as simulations go at the inlet surface. The only input parameters for the SEM are the length scale and Reynolds stress tensor of the turbulent flow. The Reynolds stress tensor of a homogeneous isotropic turbulent flow can be built using only turbulent intensity. Therefore, the SEM requires only the length scale and intensity of homogeneous isotropic turbulence. According to Choi et al.[13], the turbulent intensities above the glottis were 0.29 and 0.13 for Re_t of 1300 and 440, respectively. Based on the results from a preliminary simulations with the CT-based extrathoracic model used by Miyawaki et al.[63], the largest eddy size of

turbulence above the glottis was approximately 8.0 and 4.3 mm, or 0.44 and 0.24 $D_{h,t}$, for $\mathrm{Re_t}$ of 1300 and 2800, respectively. In this study, we used the turbulent intensity of 0.29 and turbulent length scale of 8.0 mm.

4.2.7 Aerosol Simulation

To simulate the aerosol transport in the numerical airway model, we used the Lagrangian tracking algorithm validated by Miyawaki et al.[63]. Miyawaki et al.[63] found the aerosols are well distributed over the cross-section above the glottis when air was used as carrier gas. According to a preliminary study, 20 μm-aerosols deposited most among 2.5, 5, 10, and 20 μm-aerosols in the central branches considered in this study. We considered the oral deposition using the empirical curve proposed by Grgic et al.[34] when determining the size of the aerosols that deposit most in the central branches. In this study, we released 10,000 of 20-μm aerosols uniformly over the cross-section above the glottis. We updated the flow field every 0.006 sec and released the aerosols 8 times with interval of 0.048 sec to account for the unsteady nature of air flow as in Miyawaki et al.[63]. To evaluate the performance of the hybrid model, we computed deposition efficiency (DE) for each branch:

$$DE = N/M, \tag{4.2}$$

where M and N are the numbers of aerosols entered and deposited in the branch. We used the side boundary mesh to compute N, and N and skeleton connectivity to compute M by adding N of own branch and N of all the higher-generation branches attached to own branch.

4.3 Results

4.3.1 Aerosol Deposition

To compare the aerosol deposition predicted with different models, we performed aerosol simulation using CL-based model, uniform hybrid model, and non-uniform hybrid model. We can discuss the error in geometry and aerosol deposition due to straight CL by comparing the CL-based and uniform hybrid models, and the errors due to non-uniform cross-section by comparing the uniform and non-uniform hybrid models. For CT-based model, we used the results from the simulation performed by Miyawaki et al.[63]. To compute DE for the CT-based model, we split the surface of the CT-based model used by Miyawaki et al.[63] into branches using the surface of the non-uniform hybrid model.

For comparison purposes, the DE predicted by the CL-based model, uniform hybrid model, and non-uniform hybrid model were plotted against the DE predicted by the CT-based model (Figure 4.5). We did not include the data for branches with $M < 12$ (about 100 in 8 releases) because the uncertainty in DE tends to be large when M, denominator of the right hand side of Equation 4.2, is too small. To quantitatively compare DE, we computed the p-value of the t-test for the slope of linear regression (β_1) with null hypothesis of $\beta_1 = 1$ and alternate hypothesis of $\beta_1 \neq 1$. The null hypothesis was not rejected with significance level of 10% for the non-uniform hybrid model, and 1% for the uniform hybrid model. However, the null hypothesis was rejected with significance level of 1% for the CL-based model. The correlation coefficient r was more than 0.9 for the non-uniform hybrid model,

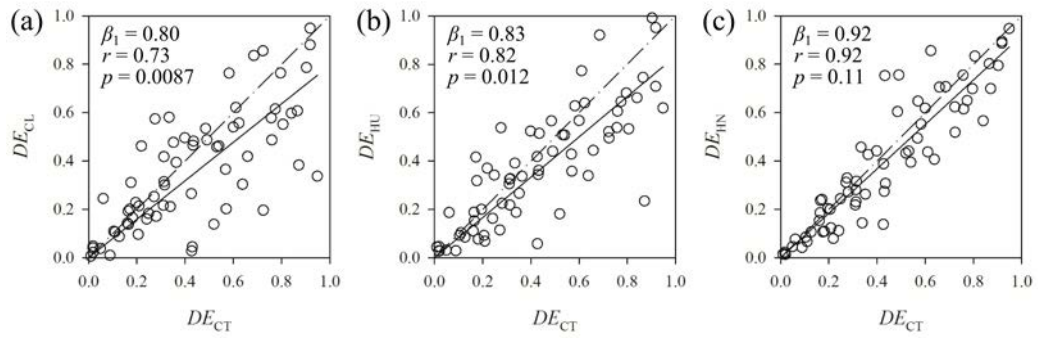

Figure 4.5: The correlations of the deposition efficiency (DE) of 20-μm aerosol predicted by computed tomography (CT)-based model with the DE predicted by the (a) centerline (CL)-based, (b) uniform hybrid, and (c) non-uniform hybrid models. The solid lines denote regression lines with zero intercept, and the dot-dashed lines denote the line with slope of one and intercept of zero. β_1, r, and p denote the slope of regression lines with zero intercept, correlation coefficient, and p-value of the t-test for β_1 with null hypothesis of $\beta_1 = 1$ and alternate hypothesis of $\beta_1 \neq 1$, respectively.

between 0.8 and 0.9 for the uniform hybrid model, and between 0.7 and 0.8 for the CL-based model. The three models overall underestimated DE, and the degree of under prediction increased in the order of the non-uniform hybrid, uniform hybrid, and CL-based model. The average DE for the branches in the CT-based model was 0.43, or 43%. The average absolute error in DE was 0.13, 0.12, and 0.08 for the CL-based, uniform hybrid, and non-uniform hybrid models, respectively, compared to the CT-based model.

4.3.2 Hybrid CL-CT-based Model

To compare the geometries of different models, we extracted the skeleton and the surface mesh of the CL-based, uniform hybrid, and non-uniform hybrid models. The major sources of error in the geometry of the CL-based model are straight branch and uniform cross-section. We estimated the error due to straight branch by comparing the skeleton of the CL-based and the hybrid models. To estimate the error due to uniform cross-section, we compared the distance between the surfaces of the CT-based and hybrid models.

For each branch, we computed the average distance between the CLN of the hybrid model and straight CL of the CL-based model, and normalized the distance by branch radius. If there are no sub-branches in a branch, the normalized average distance is zero for that branch. For instance, the normalized average distance was 0.55 in the left main bronchus (LMB), which means that the average distance between straight and curved CLs was 55% branch radius in the LMB. We further averaged the normalized average distance of branches to obtain global error due to straight branch, which was 0.14.

For each branch, we computed the average distance between the surface of the CT-based model and the surface of the CL-based, uniform hybrid, and non-uniform hybrid models; and normalized the distance by branch radius (Figure 4.6). For instance, the normalized average distance was 0.50, 0.094, and 0.025 in the LMB for the CL-based, uniform hybrid, and non-uniform hybrid models, respectively, although it was difficult to estimate the distance for the CL-based model because of the straight

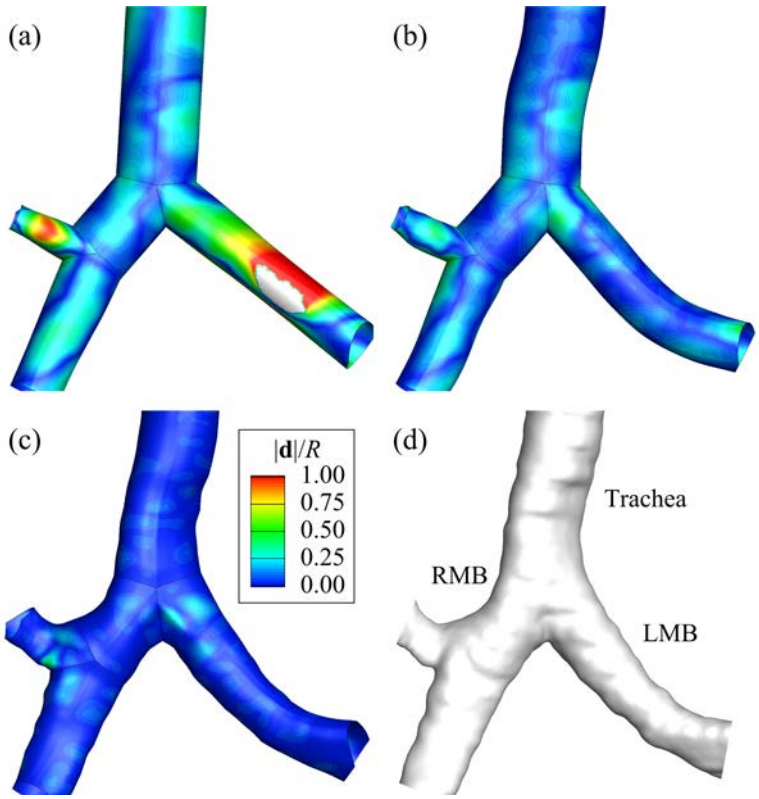

Figure 4.6: The (a) centerline (CL)-based, (b) uniform hybrid, (c) non-uniform hybrid, and (d) CT-based models around the first bifurcation. **d** is the radial distance between the surfaces of each model and the CT-based model, and R is the branch radius. LMB and RMB are left and right main bronchus, respectively.

CL. The global error was 0.25, 0.12, and 0.028 for the CL-based, uniform hybrid, and non-uniform hybrid models, respectively. The error was large at non-circular cross-sections, e.g., near carina and at the end of the LMB (Figure 4.6b). To test the robustness of the non-uniform hybrid model, we applied the model to the 8 healthy and 16 severe asthmatic (SA) subjects used in Chapter 3 (Figure 4.7). The average global error was 0.038.

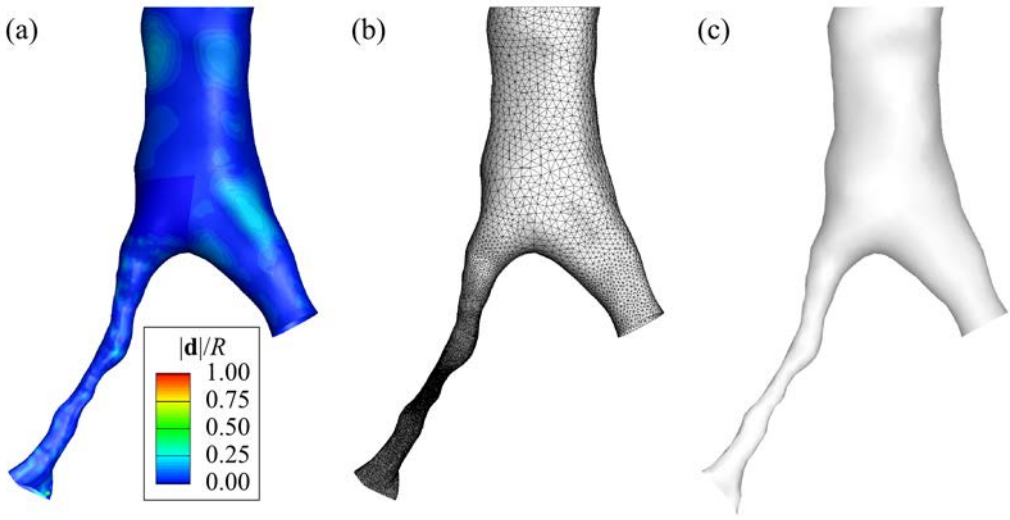

Figure 4.7: The (a) non-uniform hybrid geometry, (b) CFD mesh for non-uniform hybrid geometry, and (c) CT-based geometry around a bifurcation of a severe asthmatic subject. **d** is the radial distance between the surfaces of each model and the CT-based model, and R is the branch radius.

4.3.3 Laryngeal Model

To construct approximate geometric laryngeal model, we empirically determined the five parameters L_g^*, $D_{h,g}^*$, $D_{h,gu}^*$, l_{gu}^*, and l_{gl}^* (Figure 4.3). The normalized glottis location L_g^* ($= L_g/D_{h,t}$) were 8.64 ($\pm$ 0.58), where the value in the parenthesis indicates the standard error. The normalized hydraulic diameter at the glottis and above the glottis were 0.677 ($\pm$ 0.054) and 1.24 ($\pm$ 0.06), respectively. The best normalized length of the larynx above and below the glottis, l_{gu}^* and l_{gl}^*, were both 1.3 (Figure 4.8). The fitted curve represented the distributions of D_h^* in three geometries reasonably well.

To examine the performance of the approximate laryngeal model, we compared the turbulent kinetic energy (TKE) distribution in the trachea predicted with the CT-based and approximate models (Figure 4.9). In the CT-based model, we imposed laminar flow at the mouthpiece, while we used SEM to feed turbulent flow above the glottis in the approximate model. The laryngeal jet was not parallel to the airway direction in the CT-based model, and TKE was amplified in the shear layer around the jet (Figure 4.9a). The jet was parallel to the airway direction in the approximate model, and the approximate model captured the amplification of TKE in the shear layer around the laryngeal jet (Figure 4.9b). Furthermore, the highest TKE in the two models were of the same order of magnitude. Since cross-section was not axisymmetric in the CT-based model, we compared the cross-sectional averaged TKE (k_X) distributions in the two models. The approximate model reproduced overall profile of k_X distribution reasonably well. The approximate model overestimated

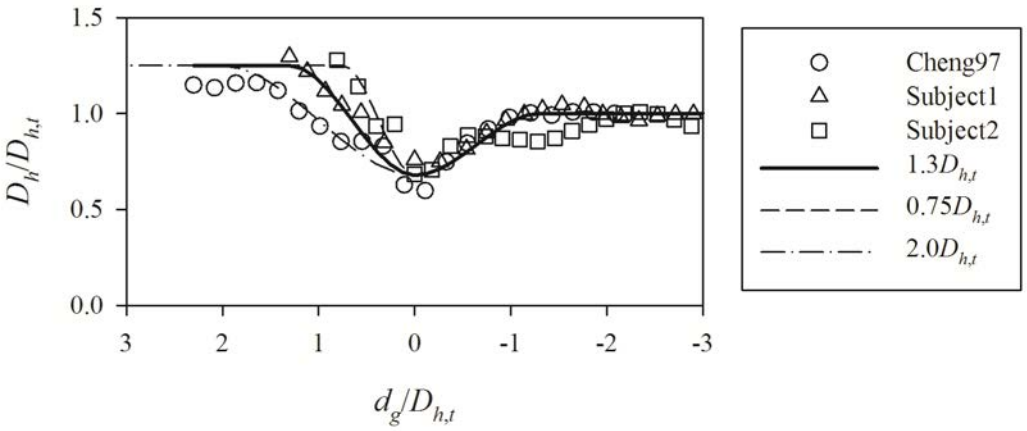

Figure 4.8: The geometric laryngeal model constructed using the geometries of Cheng et al.[12] (Cheng97) and two healthy subjects (Subject1 and 2). The lengths of larynx above the glottis normalized by the (hydraulic) diameter of the trachea l^*_{gu} for the model represented by solid, dashed, and dash-dotted curves are 1.3, 0.75, and 2.0, respectively. $D_{h,t}$, D_h, and d_g denote the hydraulic diameter of the trachea, hydraulic diameter of a cross-section in the larynx, and the distance from the glottis to the cross-section, positive in upward direction, respectively.

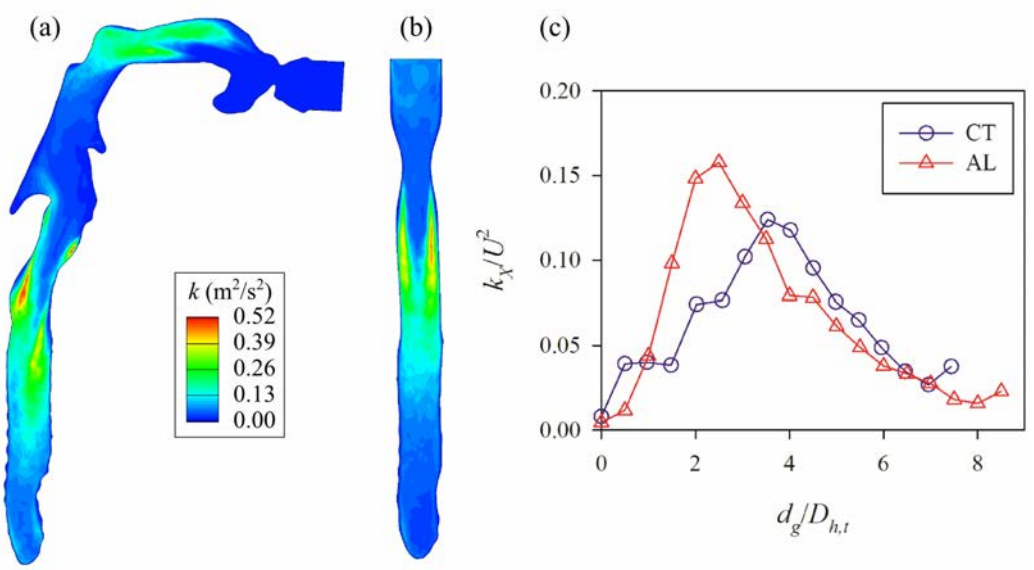

Figure 4.9: The turbulent kinetic energy (TKE, k) distributions in the plane cutting through the center of glottis predicted with the (a) computed tomography (CT)-based and (b) approximate laryngeal (AL) models, and (c) the cross-sectional averaged TKE (k_X) distribution in the trachea for both models. U, d_g, and $D_{h,t}$ are bulk velocity, distance from the glottis, and hydraulic diameter of the trachea, respectively.

the highest k_X by 27%, and the location of the highest k_X was one trachea hydraulic diameter closer to the glottis compared to the CT-based model. When we fed laminar flow above the glottis in the approximate model (not shown), TKE was negligible compared to the CT-based model.

4.4 Discussion

4.4.1 Aerosol Deposition

To evaluate the ability of the non-uniform hybrid model to predict aerosol deposition, we compared the depositions of 20 μm-aerosols predicted by the CT-based and non-uniform hybrid models. The difference between the aerosol depositions predicted by the CT-based and non-uniform hybrid models was not significant with significance level of 10%. Furthermore, the average absolute error in the aerosol deposition predicted by the non-uniform hybrid model was as small as the uncertainty in the prediction of oral deposition by CT-based model reported by Miyawaki et al.[63], which was about 0.07 at low $\mathrm{Stk} \cdot \mathrm{Re}^{0}.37$. Therefore, as expected, the quality of the automatically generated CFD mesh based on the non-uniform hybrid model is high enough to predict aerosol deposition. The non-uniform hybrid model may be used especially for studies that involve multiple subjects because this method requires much less time to pre- and post-process data compared to the CT-based models constructed manually.

We also tested the performance of the uniform hybrid and CL-based models. The uniform hybrid or CL-based model may be required when researchers want to manipulate branch diameter to investigate aerosol deposition in the human lung. For instance, we need to increase diameter of asthmatic branches if we want to investigate the effect of skeleton in asthmatic lung on aerosol deposition because asthmatic branches are typically narrower than healthy branches. As expected, the uniform hybrid model was more accurate than the CL-based model in terms of the prediction of

aerosol deposition. Therefore, the uniform hybrid model should be used when branch diameter needs to be manipulated.

To discuss the error in the prediction of aerosol deposition, we can use the difference between aerosol depositions predicted by the CL-based, uniform hybrid, and non-uniform. The three models underestimated aerosol deposition by 20, 17, and 8% on average, respectively. The underestimation by the CL-based and uniform hybrid models is reasonable, because CL is straight in the CL-based model and cross-section is uniform in the uniform hybrid model. Straight CL contributes 25% and uniform cross-section contributes 75% of the difference between the aerosol depositions predicted by CL-based and non-uniform hybrid models.

4.4.2 Hybrid CL-CT-based model

We compared the geometry of the CT-based model with that of the CL-based, uniform hybrid, and non-uniform hybrid models. The error in the surface geometries of the CL-based, uniform hybrid, and non-uniform hybrid models were 25, 12, and 2.8%, respectively. The difference between the errors in the surface geometries of CL-based and uniform hybrid models agreed with the average distance between the straight and curved CLs, which was 14%. Straight CL contributes 59% and uniform cross-section contributes 41% of the difference between the surface geometries of CL-based and non-uniform hybrid models.

To test the robustness of the non-uniform hybrid model, we applied the model to SA subjects. It is well known that asthmatic lungs tend to have narrow branches,

which makes it difficult to fit CLs. Asthmatic branches also tend to be non-circular possibly due to excessive mucus, and accurate fitting requires more than four CNs. The average error in the surface of geometries for 8 healthy and 16 SA subjects was 3.8%, which is as small as the error for the subject considered in this study. Therefore, this model may also be used to study SA subjects.

4.4.3 Laryngeal Model

To construct artificial laryngeal model, we empirically determined the dimensions of larynx. According to Choi and Wroblewski[16], the ratio of cross-sectional area at the glottis to trachea is 0.40 at mid-inspiration, i.e., $D^*_{h,g}$ is 0.63 with the assumption of circular cross-section. The $D^*_{h,g}$ found in this study is reasonably consistent with the published value for mid-inspiration.

We used the empirically determined dimensions of larynx and SEM to reproduce turbulent laryngeal jet. The approximate laryngeal model captured overall distribution of TKE in the trachea reasonably well, and the highest TKE predicted by the CT-based and approximate laryngeal models were of the same order of magnitude. We think the approximate laryngeal model reproduced realistic level of turbulence given that (i) we defined the geometry of larynx with only five parameters, (ii) we only specified the largest eddy size and turbulent intensity as input to generate isotropic turbulent flow above the glottis, and (iii) we did not optimize the parameters specifically for this subject. If the airway geometry above the trachea is unknown, the turbulent flow generated with this approximate laryngeal model would be accurate

enough.

4.4.4 Advantages

The CL-based and hybrid models are basically an extension of 1-D tree to 3-D geometry, and the major advantages of these models are related to this modeling philosophy. Since these models are extended from 1-D tree, one sub-domain corresponds to one branch. This is a very important feature of numerical models for the following nine reasons. First, we can create the geometry with generated or manipulated skeleton using the CL-based model. Second, we can create the geometry with manipulated diameter using the uniform hybrid model. Third, we can create the geometry that includes CT-resolved and CT-unresolved branches combining the non-uniform hybrid and CL-based models. Fourth, we can generate CFD mesh for branches in parallel. Fifth, we can easily impose boundary conditions using, e.g., flow rate and diameter even for a large number of branches. Sixth, we can map the surface and volume elements in the CT-based model to branches using non-uniform hybrid model. Seventh, we can easily compute branch-averaged quantity during/after gas-flow simulations. Eighth, we can easily count the number of aerosols entered and deposited in branches during/after aerosol simulations. Thanks to the seventh and eighth features, we can investigate the correlation between the quantities for branches with the geometric properties of the branches, e.g., diameter, length, curvature, branching angle, and gravity angle. Ninth, we can investigate multiple subjects easier compared to traditional manual methods. For example, the method proposed by Marchandise et al.[61]

does not have the first three features, although the quality of their CFD mesh for CT-resolved branches seems high. The elements in their CFD mesh can be mapped to branches using the non-uniform hybrid model for post-processing.

4.4.5 Potential Improvements

In this study we did not consider the other functions of extrathoracic region in drug delivery, but they can be included depending on the purpose of the simulations. The important function is the filtering or aerosols due to oral deposition. This can be implemented using the similarity curve based on the experiments conducted by Grgic et al.[34] (Grgic's curve). The seven parameters, five for geometry and two for gas-flow, for the approximate laryngeal model could be improved by studying more subjects. It would be ideal to find empirical formula for those parameters based on clinical characteristics of subjects, breathing patterns, and geometry of trachea so that the parameters can be determined even if CT images do not include extrathoracic region. Furthermore, in moving lung simulations, the parameters for glottal opening ($D^*_{h,g}$) and gas-flow may need to vary during a respiratory cycle[8].

CHAPTER 5
NUMERICAL INVESTIGATION OF AEROSOL DEPOSITION IN HUMAN LUNGS WITH SKELETONS OF SEVERE ASTHMATIC SUBJECTS

5.1 Introduction

More than 200 million people in the world suffer from asthma according to an estimate by World Health Organization (WHO) in 2011[91]. Asthma is caused by genetic and environmental factors, which explain 30-80% and 20-70% of asthma risk, respectively[66]. Environmental factor consists of exposure to biological and chemical aerosols, e.g., house dust mites, pollen, NO_x, and environmental tobacco smoke (ETS). Asthma causes airway narrowing mainly because of muscle tightening, airway inflammation, and excessive mucus (e.g., [45]), which makes it difficult for the patients to breath due to higher resistance. Thus, a better understanding of the cause of asthma would improve the prevention and treatment of asthma.

The exposure to aerosols can be investigated numerically. The numerical (*in silico*) models based on three-dimensional (3-D) computational fluid dynamics (CFD) can provide aerosol deposition in each branch using first principles (mainly Navier-Stokes equation and equation of particle motion) (e.g., [63]). Researchers have used the 3-D CFD-based numerical models to understand the aerosol deposition in asthmatic lungs (e.g., [72, 58, 41]). Several structural and functional variables such as airway skeleton structure, LA, and regional ventilation could contribute to the development of asthma caused by aerosol exposure. In most of the numerical studies of

asthma, the effect of narrowed branches on aerosol deposition was investigated and higher aerosol deposition and larger pressure drop were found in narrowed branches when regional ventilation of healthy subjects was applied. These studies did not investigate the correlation between skeleton structure of asthmatic subjects and aerosol deposition. The objective of the present study is to investigate the effect of skeleton structure on aerosol deposition in asthmatic lungs using in-house subject-specific 3-D CFD-based numerical models.

The inter-subject variability in airway skeleton could be related to the inter-subject variability in development of asthma. It is well known that high density of aerosols in air increases the risk of asthma[66], but this alone may not fully explain why one person will develop asthma but another will not in similar environmental conditions. It is possible that the lungs of the two people have different structure and function, resulting in higher exposure to aerosols for one of the individuals. In large (proximal) branches, aerosols deposit mainly due to inertial impaction, so smaller diameter, larger flow rate, and larger curvature of airflow streamline can cause higher aerosol deposition. The curvature of streamline is determined by airway skeleton, especially branching angle (BA), which can be defined as the difference between the directions of parent and child branches (e.g., [40, 52]). In small (peripheral) branches, sedimentation is the main aerosol deposition mechanism; sedimentation depends on gravity angle, which is defined as the difference between the directions of gravity and a branch. Researchers have performed cluster analyses to find the phenotypes of severe asthma (e.g., [42]), but the variables related to airway skeleton were not considered.

We hypothesize that there are asthmatic subjects whose airway skeletons can cause higher aerosol deposition compared to healthy subjects.

The study of correlation between airway skeleton structure and aerosol deposition in asthmatic subjects gives some insight into the understanding of the environmental factor of asthma. The exposure to aerosols does not affect BA according to a previous study of rat lungs[52]; Montaudon et al.[64] found that LA of branches with fourth or higher generation in asthmatic lungs is significantly smaller than that in healthy lungs; Orphanidou et al.[67] and Choi et al.[15] found that asthma changes regional ventilation. Therefore, airway model with controlled LA, controlled regional ventilation, and subject-specific skeleton is similar to the airway before the development of asthma. The results from the aerosol simulations with this airway should provide insightful information about the environmental factor of asthma. CT images of healthy subjects can provide the controlled LA of central branches, the Horsfield's model[40] can provide the controlled regional ventilation in central airway, and the hybrid CL-CT-based model developed in Chapter 4 can construct the airway geometry with the controlled LA and subject-specific skeleton.

The rest of the chapter is organized as follows. First, we mainly describe the method to create the airway geometry before the onset of asthma. Second, we present the results from the numerical simulations about the skeleton and aerosol deposition in asthmatic lungs before the onset of asthma. Finally, we discuss the effect of skeleton on aerosol deposition in asthmatic lungs.

5.2 Methods

We analyzed the geometry and aerosol deposition in central branches of healthy and severe asthmatic (SA) subjects, following three main steps. First, we randomly selected normal and SA subjects from the data set acquired through the Severe Asthmatic Research Program (SARP). Second, we measured the dimensions of central branches and created airways before development of asthma using in-house image-based geometric airway model (Chapter 3 and 4). Finally, we simulated aerosol motion in the airways using in-house numerical aerosol model[63]).

5.2.1 Healthy and Severe Asthmatic Subjects

In a preliminary study, we found that the branches in SA lungs that can be resolved by CT do not seem to be significantly narrower than those in healthy lungs if forced expiratory volume in one second is higher than 45% predicted (FEV1pp $>$ 45%). Thus, we classified SA subjects into two sub-groups: SA1 if FEV1pp $<$ 45% and SA2 if FEV1pp $>$ 45%. To analyze the geometry of airways, we randomly selected the CT images of eight healthy, eight SA1, and eight SA2 subject from the data set obtained at the University of Pittsburgh. The Institutional Review Board at the University of Pittsburgh approved the associated human studies along with the imaging protocol. Airways in CT images become more difficult to identify if the body mass index (BMI) is too large, so we did not include the subjects with BMI larger than 35. Table 5.1 shows that there is no significant difference in BMI and total lung capacity (TLC) between the three groups, while FEV1pp is significantly different.

Table 5.1: Clinical characteristics of healthy and severe asthmatic (SA) subjects used for geometric analysis.

Group	Healthy	SA1	SA2
Height (cm)	166 ± 10	173 ± 10	171 ± 12
Weight (kg)	68 ± 16	84 ± 25	78 ± 17
BMI	24 ± 4.7	28 ± 5.6	27 ± 3.1
TLCpp (%)	98 ± 12	105 ± 16	97 ± 13
FEV1pp (%)	96 ± 10	$37 \pm 5.2^{\dagger,\ddagger}$	$66 \pm 17^{\dagger}$

[a] The data are based on eight subjects for each group, and mean $\pm$ sample standard deviation is presented.

[b] The signs † and ‡ indicate significantly smaller values compared to healthy and SA2 lungs, respectively, based on one-tailed t-test with significance level of 5%.

To analyze aerosol deposition, we selected three healthy (1-3) and three SA1 (4-6) subjects (Table 5.2). The in-house large eddy simulation (LES)-based model is more accurate than Reynolds-Averaged Navier-Stokes (RANS)-based model, but the model is still computationally too expensive to simulate aerosol motion for 24 subjects used in geometric analysis. The effect of turbulent diffusion on aerosol deposition was controlled by selecting the subjects with similar TLC: 5.30 ± 0.16 L and 5.31 ± 0.29 L for healthy and SA1 subjects. Subjects 4 and 5 developed asthma as adult, so we can use their data to discuss the environmental factor of asthma. We can still use the data of the three SA1 subjects to discuss the effect of skeleton on aerosol deposition in asthmatic lungs. The number of subjects in the analysis of aerosol deposition is small, so my intent is to find if there is more aerosol deposition in any of the three SA1 lungs compared to healthy subjects, rather than to draw general conclusions about SA subjects.

5.2.2 Geometry of Healthy Airways

We created the geometry of airways with average healthy LA and subject-specific skeleton using the hybrid centerline (CL)-CT-based geometric model (Chapter 3 and 4). First, we manually improved the segmentation of CT images after running automatic segmentation on a commercial segmentation program Apollo (VIDA). Second, we extracted the branches corresponding to the central branches 0-38 used by Horsfield et al.[40] (Figure 5.1). To compare the dimensions of the airways up to fourth generation with published data, we included more branches so that all branches

Table 5.2: Clinical characteristics of healthy and severe asthmatic (SA) subjects used for aerosol analysis.

Group	Healthy			SA1		
Subject	1	2	3	4	5	6
AAO	-	-	-	28	24	0
TLC (L)	5.17	5.48	5.24	5.55	4.98	5.39
TLCpp (%)	111	103	101	127	105	88
FEV1pp (%)	102	109	94	40	42	35
μ_{Area^*}	0.99	0.99	0.98	0.49	0.75	0.89

[a] AAO is age of asthma onset.

with generation up to four were included. The added branches were not considered when analyzing aerosol deposition.

Third, we obtained the LA and BA of each branch using the hybrid geometric model. We estimated the inner diameter of an airway lumen by averaging the radii in four directions that are perpendicular to each other, and we used the diameter to estimate the LA with the assumption of a circular lumen (Figure 5.2 (a)). Most of the aerosols deposit near carina due to impaction in central branches, so the BA near carina should be more related to aerosol deposition, rather than the BA for the entire branch. For instance, the left main bronchus (LMB) tends to be long and curved, so the two BAs are different. The hybrid geometric model splits a long branch into sub-branches whose aspect ratios are about one, where aspect ratio is the ratio of the length to diameter of a (sub-) branch. We computed the BA using the parent and

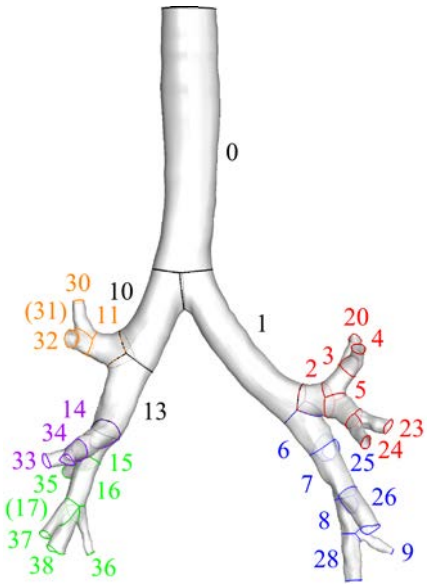

Figure 5.1: The branch numbers used by Horsfield et al.[40]. Branch 31 is hidden behind branches 30 and 32, and branch 17 for this subject is very short. The numbers and edges of branches are colored by lobe.

child sub-branches directly connected to the carina (Figure 5.2 (b)).

Fourth, we normalized the LA with TLC to eliminate the inter-subject variability in LA due to lung size:

$$LA^*_{b,s} = LA_{b,s}/TLC_s^{2/3}, \tag{5.1}$$

where b is branch index and s is subject index. This normalization is reasonable because the TLC of the asthmatic lungs is about 100% predicted value (Table 5.1), and small normalized LA means that the airway is narrow compared to the capacity of the lung, resulting in small FEV1pp. Fifth, we computed the average normalized

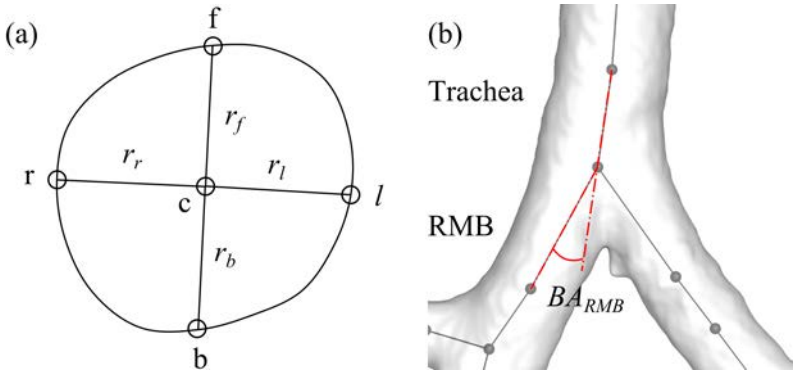

Figure 5.2: The definition of the dimensions of branches: (a) the radii in four directions used to estimate luminal area (LA), and (b) the branching angle (BA). r, f, l, b, and c are right, front, left, back, and centerline points in Chapter 3, respectively. The figure shows the BA of right main bronchus (RMB).

healthy LA and BA for each central branch:

$$LA^*_{h,b} = (1/N_h)\sum_{s=1}^{N_h} LA^*_{b,s} \text{and} \tag{5.2}$$

$$BA_{h,b} = (1/N_h)\sum_{s=1}^{N_h} BA_{b,s}, \tag{5.3}$$

respectively, where N_h is the number of healthy subjects. Sixth, we further normalized LA and BA with average healthy values:

$$LA^{**}_{b,s} = LA^*_{b,s}/LA^*_{h,b} \text{and} \tag{5.4}$$

$$BA^*_{b,s} = BA_{b,s}/BA_{h,b}. \tag{5.5}$$

For simplicity, we may use Area* and Angle* to mean $LA^{**}_{b,s}$ and $BA^*_{b,s}$ hereafter, respectively. Seventh, we computed average normalized LA for each subject (LA^{**}_s)

to evaluate overall degree of disease:

$$LA_s^{**} = (1/N_b) \sum_{b=1}^{N_b} LA_{b,s}^{**}, \tag{5.6}$$

where N_b is the number of branches. For simplicity, we may use μ_{Area^*} to mean LA_s^{**} hereafter. Eighth, we computed the average healthy LA for each branch in each subject ($LA_{h,b,s}$) using their TLC and the average normalized healthy LA:

$$LA_{h,b,s} = LA_{h,b}^{*} \cdot TLC_s^{2/3}. \tag{5.7}$$

We selected the subjects with similar TLC, so $LA_{h,b,s}$ does not vary with subject. Finally, we created the CFD mesh of airways with average healthy LA ($LA_{h,b,s}$) and subject-specific skeleton using the hybrid geometric model (Chapter 3). Each branch in the resulting CFD mesh has circular cross-section and curved centerline (Figure 5.3). The CT-image of the airway above trachea was not available, so we attached the laryngeal model developed in Chapter 4 to the trachea.

5.2.3 Numerical Aerosol Simulations

To reproduce 3-D turbulent air flow field in the airways, we used the 3-D CFD model developed and validated by Lin et al.[53] and Choi et al.[14]. In central branches, air flow is turbulent (e.g., [21, 63]), so the model is based on LES to resolve large scale eddies. We considered the steady inhalation with flow rate of 20 L/min to simulate breathing in rest condition, and the corresponding local Reynolds number in the trachea (Re_t) is 1600. We imposed turbulent flow at the inlet (above glottis) using synthetic eddy method (SEM)[43] as in the simulations in Chapter 4. We

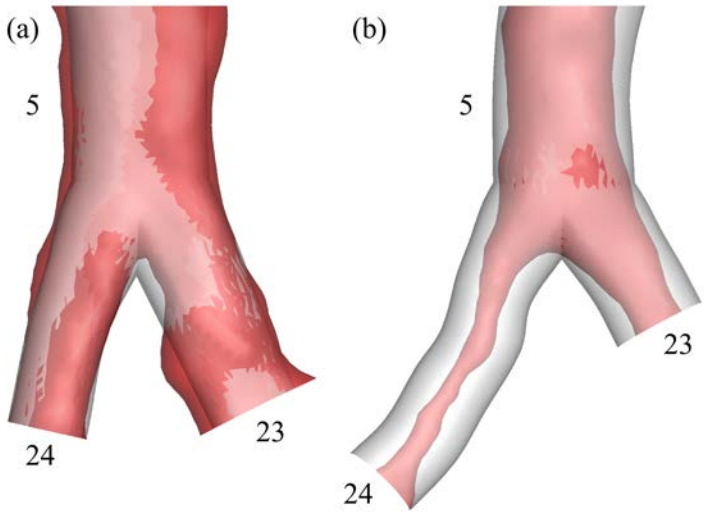

Figure 5.3: The surface of computed tomography images (red) and computational fluid dynamics meshes (white) at left lingual bifurcation for subjects (a) 1 and (b) 4 with average healthy luminal area ($LA_{h,b,s}$) and subject-specific skeleton. The numbers in the figure denote the branch numbers used by Horsfield et al.[40]. The luminal area (LA) of branch 24 in subject 4 is 7% of average healthy LA ($LA^{**}_{b,s} = 0.07$).

estimated the length scale of the largest eddy and turbulent intensity at the inlet by using the data from a preliminary study and the data presented by Choi et al.[13]. We scaled the length scale and turbulent intensity based on trachea diameter and Re_t. To control the effect of regional ventilation on aerosol deposition, we applied the flow rate outlet boundary condition proposed by Horsfield et al.[40] to every subject. This means the local Re and Stokes number (Stk) in a branch of a subject are similar (difference $< 5\%$) to those of another subject because the averaged healthy LAs are similar.

To compute the particle trajectories in airways, we used Lagrangian particle tracking model developed and validated by Kumar et al.[49] and Miyawaki et al.[63]. The CFD simulation is much more computationally expensive than aerosol simulation, so we computed the particle trajectories as a post process of the CFD simulation. The Re_t is similar to the Re_t used in the simulation of air by Miyawaki et al.[63], so we updated the unsteady flow field every 0.006 sec in this study as well to resolve large eddies. We evaluated aerosol deposition in a branch using deposition efficiency (DE), which is defined as

$$DE_b = N_{p,b}/M_{p,b}, \tag{5.8}$$

where $M_{p,b}$ and $N_{p,b}$ are numbers of aerosols entered and deposited in branch b, respectively. Average healthy DE and normalized DE are defined as

$$DE_{h,b} = (1/N_h)\sum_{s=1}^{N_h} DE_{b,s} \text{and} \tag{5.9}$$

$$DE^*_{b,s} = DE_{b,s}/DE_{h,b}, \tag{5.10}$$

respectively, where $DE_{b,s}$ is DE_b in Equation 5.8 for subject s. For simplicity, we may use Ptcl* to mean $DE^*_{b,s}$ hereafter.

We used the most effective aerosol size when analyzing aerosol deposition, and we used the deposition fraction (DF) of the branches of interest to compare the effectiveness of aerosol size. The DF of a branch is defined as the ratio of the number of aerosols deposited in the branch to the number of aerosols entered the oral cavity:

$$DF_b = \frac{N_{p,b}}{M_{p,o}} = \frac{M_{p,t}}{M_{p,o}}\frac{N_{p,b}}{M_{p,t}} = \frac{M_{p,o} - N_{p,o}}{M_{p,o}} DF'_b = (1 - DF_o)DF'_b, \tag{5.11}$$

where $N_{p,o}$ is the numbers of aerosols deposited in the oral cavity, $M_{p,o}$ and $M_{p,t}$ are numbers of aerosols entered the oral cavity and the trachea, respectively, DE_o is the DE in oral cavity, and DF_b is the DF based on M_t, rather than M_o. The DE_o was estimated based on the empirical curve for oral deposition proposed by Grgic et al.[34] and the length scale of the oral cavity used by Miyawaki et al.[63].

As we will present later, the LA of the SA1 subjects was significantly smaller than that of the healthy subjects in the central branches whose generation number is greater than two, so we considered those branches as the branches of interest when obtaining the effective aerosol size. The total DF of 5, 10, 20, and 40-μm aerosols in the central branches whose generation number is greater than two, i.e., $\sum_{gen>2} DF_b$, were 0.03, 0.10, 0.16, and 0.00, respectively. Therefore, 20 μm was the most effective among the four aerosol sizes tested, and 16% of 20-μ aerosols deposited in the branches of interest. The analyses of aerosol deposition below are based on the results from the simulations of 20-μm aerosols. Cement dust, Coal dust, flour, paint spray, bacteria, and pollen may contain 20-μm aerosols[38].

5.2.4 Statistical Tests

We used two-tailed and one-tailed t-test for mean with significance level of 5% to test if one value is "significantly different" from another value and if one value is "significantly smaller" than another value, respectively.

5.3 Results

5.3.1 Aerosol Deposition in Asthmatic Lungs

We found the correlation between diseased branch and aerosol deposition in one (subject 4) of the three SA1 subjects considered even if the LA is healthy. In Figure 5.4, each point represents one branch of subject 4. In this study, we assumed a branch of SA subjects with smaller Area* is more diseased because it is well known that luminal area of asthmatic branches is smaller than that of healthy branches. The correlation coefficient r for Area* vs. Ptcl* was -0.49, and p-value of the two-tailed t-test for the slope of linear regression was 0.014 (Figure 5.4 (a)). This implies that there is more aerosol deposition in more diseased branches even if the LA is as large as that in healthy branches. The r and p-value for Area* vs. Angle* were -0.40 and 0.056 if one branch with very large BA (branch 31) is not considered (Figure 5.4 (a)). This implies that the BA of more diseased branches is larger, although p-value is slightly larger than 5%, i.e., marginally significant. The r and p-value for Angle* vs. Ptcl* were 0.42 and 0.042 if one branch with very large BA (branch 31) is not considered (Figure 5.4 (b)). This implies that there is more aerosol deposition in the branches with larger BA.

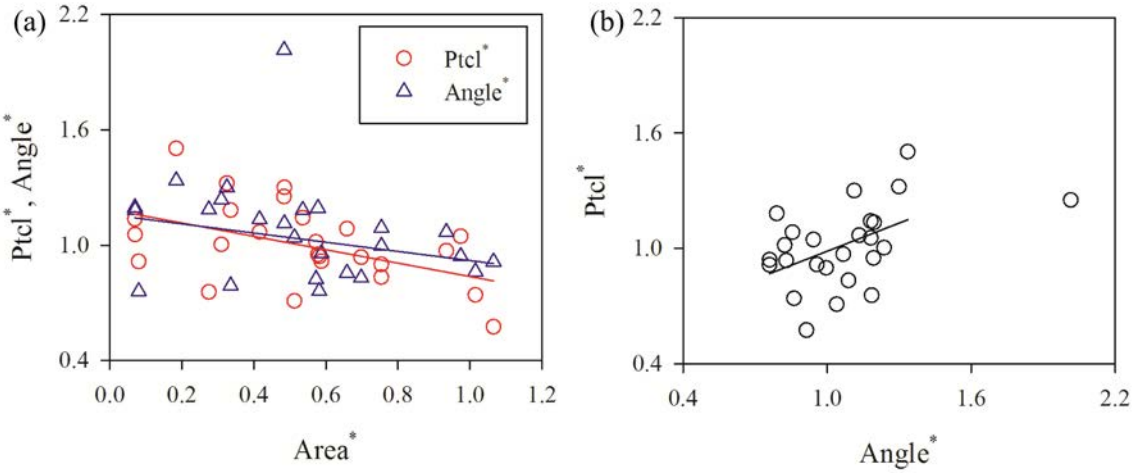

Figure 5.4: The correlation between normalized luminal area (Area*), normalized deposition efficiency of 20-μm aerosols (Ptcl*), and normalized branching angle (Angle*) for one (subject 4) of the three SA1 subjects analyzed. The correlation coefficient r and p-value for Area* vs. Ptcl*, Area* vs. Angle*, and Angle* vs. Ptcl* were (-0.49, 0.014), (-0.40, 0.056), and (0.42, 0.042), respectively, if one outlier with very large BA is not included. The number of healthy subjects (N_h) used to get Area*, Ptcl*, and Angle* are eight, three, and three, respectively.

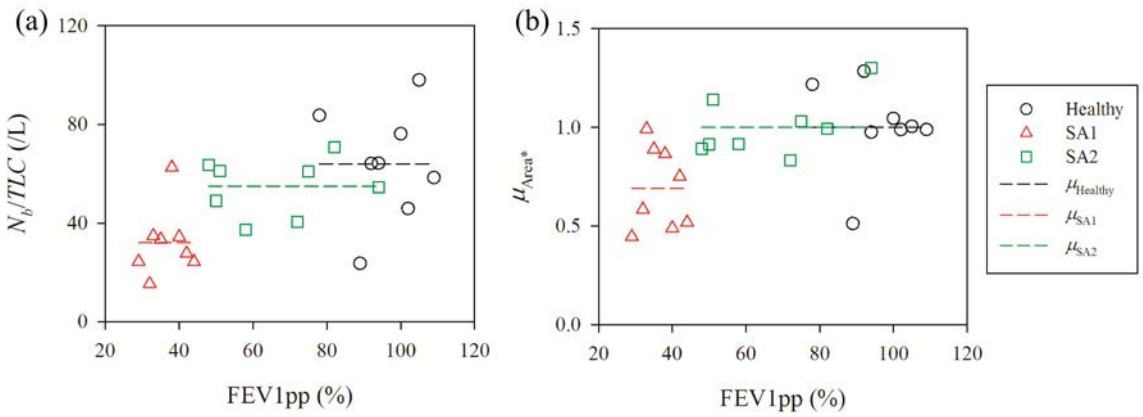

Figure 5.5: The number of segmented branches normalized by TLC and (b) the average normalized luminal area of central branches as a function of FEV1pp for healthy, SA1, and SA2 subjects.

5.3.2 Luminal Area and Branching Angles

The number of segmented branches in SA1 subjects was significantly smaller than that of healthy and SA2 subjects. In Figure 5.5, each point represents one subject, and the dashed line denotes the average value for each group. The branches in SA1 subjects were clearly narrower than those in healthy and SA2 subjects based on visual inspection, so we counted the number of branches segmented to quantify this difference. The smaller number of segmented branches imply overall narrower branches with given spatial resolution of CT images. The number of segmented branches in SA1 subjects was significantly smaller than that in healthy ($p = 0.003$) and SA2 ($p = 0.002$) subjects, but the number of segmented branches in SA2 subjects was not significantly smaller than that in healthy subjects (Figure 5.5 (a)), which agrees with qualitative observation.

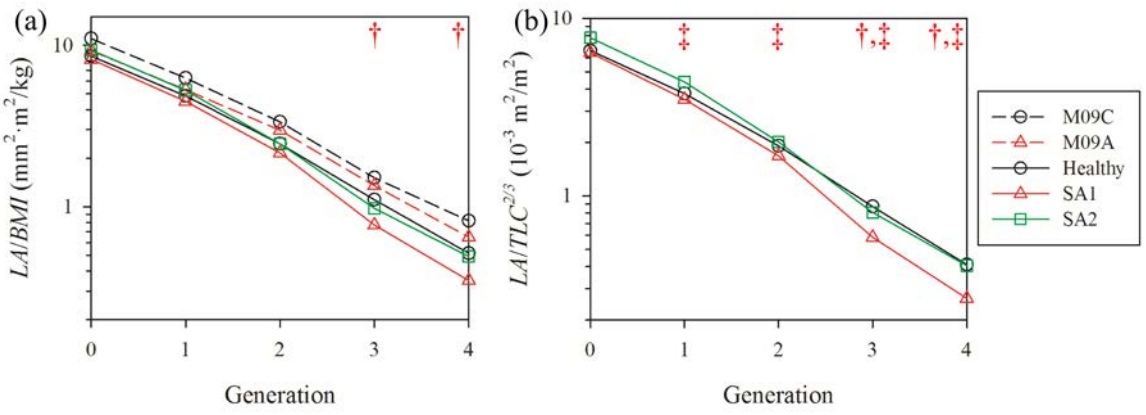

Figure 5.6: The average generational luminal area (LA) normalized by (a) body mass index (BMI) and (b) total lung capacity (TLC) for controlled (M09C) and asthmatic (M09A) subjects reported by Montaudon et al.[64], healthy, SA1, and SA2 subjects. The signs † and ‡ indicate significantly smaller values compared to healthy and SA2 subjects, respectively, based on one-tailed t-test with significance level of 5%.

The LA of central branches with generation number higher than two in SA1 subjects was significantly smaller than that in healthy subjects. Figures 5.6 (a) and (b) shows that LA of central branches normalized either by BMI or TLC is significantly smaller than that in healthy subjects if generation number is three or four. Figure 5.6 (b) shows that LA of central branches normalized by TLC is significantly smaller than that in SA2 subjects for generation one through four.

The LA of central branches in SA1 subjects was significantly smaller than that of healthy and SA2 subjects. To compare the LA of central branches collectively, we compared $\mu_{\text{Area}*}$ of the subjects in the three groups. The LA of central branches in SA1 subjects was significantly smaller than that in healthy ($p = 0.007$) and SA2 (p

= 0.003) subjects, but the LA of central branches in SA2 subjects was not significantly smaller than that in healthy subjects (Figure 5.5 (b)). μ_{Area^*} of subject 4 was the smallest among the three SA1 subjects considered in aerosol deposition analysis (Table 5.2). To compare the LA of central branches individually, we compared Area* of the central branches in healthy and SA1 subjects. The LA of SA1 subjects was smaller than that of healthy subjects in 31 of 32 (97%) branches, and the former was significantly smaller than the latter in 12 of 32 (38%) branches (Figure 5.7 (a)), whose generation number is higher than one (Figure 5.7 (b)).

The BA of central branches in SA1 subjects was not significantly different from that of healthy subjects. To compare the BA of central branches individually, we compared Angle* of the central branches in healthy and SA1 subjects. The BA of SA1 subjects was larger than that of healthy subjects in 20 of 31 (65%) branches, and the former is significantly different from the latter in 1 of 31 branches (3%) branches (Figure 5.8 (a)).

5.4 Discussion

We analyzed the geometry and aerosol deposition of central branches in healthy and SA subjects using the in-house numerical airway geometry and aerosol models, respectively. We tried to find if there are any SA subjects whose airway skeleton can cause higher aerosol deposition compared to healthy subjects.

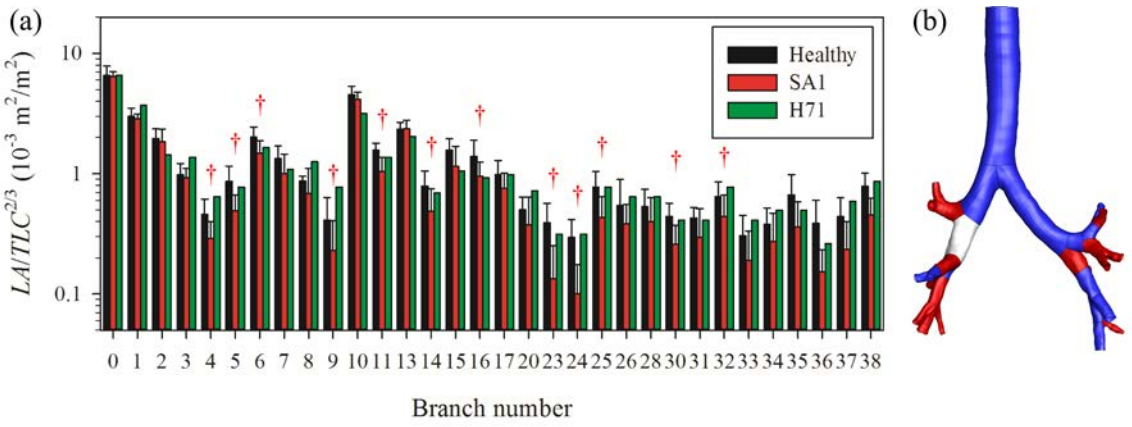

Figure 5.7: (a) The normalized luminal area ($LA^*_{b,s}$) of central branches in healthy subjects, SA1 subjects, and the healthy subject studied by Horsfield et al.[40] (H71); and (b) the location of the branches where $LA^*_{b,s}$ of SA1 subjects is smaller (blue) or significantly smaller (red) than that of healthy subjects. The TLC of the healthy subject studied by Horsfield et al.[40] was not available and assumed to be the average TLC (5.43 L) of the healthy subjects in the present study. The sign † indicates significantly smaller values compared to healthy subjects based on one-tailed t-test with significance level of 5%.

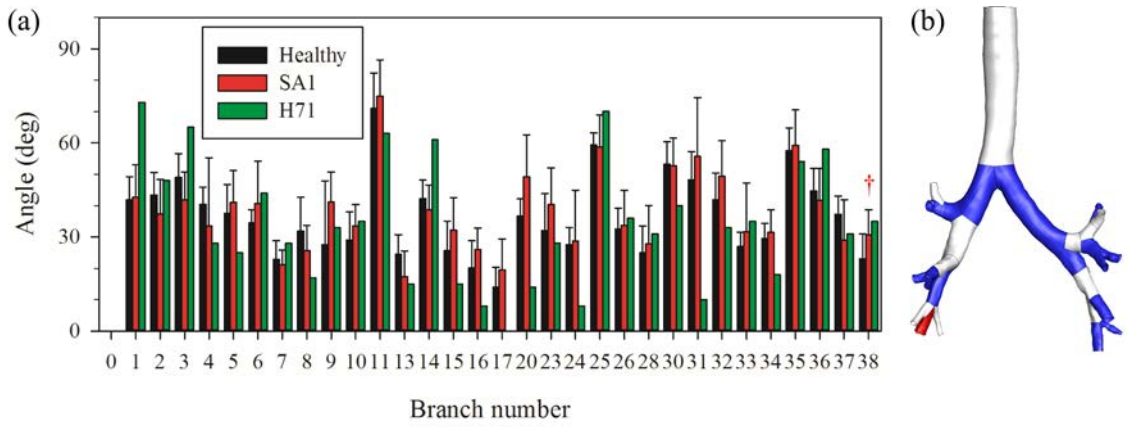

Figure 5.8: (a) The branching angle ($BA_{b,s}$) of central branches in healthy subjects, SA1 subjects, and the healthy subject studied by Horsfield et al.[40] (H71); and (b) the location of the branches where $BA_{b,s}$ of SA1 is larger (blue) or significantly larger (red) than that of healthy subjects. The sign † indicates significantly different values compared to healthy subjects based on two-tailed t-test with significance level of 5%.

5.4.1 Aerosol Deposition in Asthmatic Lungs

We found significant correlation between diseased (narrow) branches and aerosol deposition in the most diseased SA1 subject (subject 4) among the three SA1 subjects considered in the analysis of aerosol deposition even if the LA of the diseased branches is healthy. The sign of the correlation coefficient is negative, so there is more aerosol deposition in more diseased (narrower) branches compared to healthy subjects. We try to find the cause of this correlation. In the analysis of aerosol deposition, LA, breathing pattern, and regional ventilation were controlled (healthy), so two of the most important non-dimensional parameters for aerosol deposition in central branches Re and Stk (e.g., [34]) were controlled. The other important fac-

tors in aerosol deposition in central branches include BA and aerosol distribution before entering a branch, which depends on the aerosol motion in the upstream. We found significant correlation between BA and aerosol deposition in this subject. The sign of the correlation coefficient is positive, so there is more aerosol deposition in the branches with larger BA compared to healthy subjects. Larger BA implies that larger curvature of airflow streamlines, resulting in more aerosol deposition due to impaction, so this correlation is reasonable especially when Re and Stk are controlled. This implies the more diseased branches have larger BA, and we found marginally significant ($p < 0.06$) correlation between diseased branches and BA.

The results show the possibility that this subject (subject 4) had central branches with larger BA, and that caused more aerosol deposition, resulting in diseased (narrow) branches. This is based on the assumption that exposure to aerosol does not affect BA as reported by Lee et al.[52] using rat lungs. Even if this is the case, it is still not clear why this subject had branches with larger BA compared to healthy subjects. It should be also noted that this alone does not fully explain the cause of asthma, but this rather shows higher risk of asthma due to environmental factors. If asthma (aerosol exposure) does affect BA, i.e., my assumption is not valid; it is possible that asthma changed the skeleton of this subject in a way that increased aerosol deposition as Inthavong et al.[41] briefly mentioned. If this is the case, developing asthma would cause more aerosol deposition due to narrowed LA and increased BA. It is still not clear why there was not significant correlation between diseased branches and aerosol deposition in the other two SA1 subjects (subjects 5 and 6).

Their asthma might not have been caused by environmental factors.

We found that 20-μm aerosols are the most effective among 5, 10, 20, and 40-μm aerosols for the deposition in central branches whose generation number is higher than 2. This aerosol size is larger than the most effective aerosol size for tracheobronchial deposition, e.g., summarized by Stahlhofen et al.[77], which is about 6 μm. This is reasonable because tracheobronchial region include more (up to 15th generation) branches, where more small aerosols should deposit due to sedimentation. We did not consider aerosol growth, but the aerosols whose size become about 20-μm as they reach central branches may be important when considering environmental factors for asthma.

5.4.2 Luminal Area and Branching Angle

We found significant difference between the LAs of central branches in SA1 and SA2 subjects, but no significant difference between healthy and SA2 subjects. We classified SA subjects based on FEV1pp, and the threshold value for FEV1pp was 45%. The number of segmented branches and LA ($\mu_{\mathrm{Area}*}$) of SA1 subjects were significantly smaller than those of SA2 subjects. There was no significant difference in either number of segmented branches or LA between healthy and SA2 subjects. This implies that proximal branches were affected in SA1 subjects, but not in SA2 subjects. SA2 subjects still have severe asthma, so it is possible that only peripheral branches were affected in SA2 subjects. When airflow and/or aerosol deposition in the airway of SA subjects are investigated using CT images, SA2 subjects may not be

different from healthy subjects because their airway geometry is not clearly different from healthy one in the region that can be resolved by CT at the moment.

The difference between the average generational LA profiles of healthy and SA1 subjects was significant, which is consistent with the study by Montaudon et al.[64]. The slope of average generational LA profile agreed with that reported by Montaudon et al.[64] reasonably well (Figure 5.6 (a)). The difference in the LAs of trachea, left main bronchus (LMB), and right main bronchus (RMB) (branches with generation number 0-1) between healthy and SA1 was smaller than that between controlled and asthmatic subjects reported by Montaudon et al.[64] (Figure 5.6 (a)). The LAs of central branches with generation number greater than two in SA1 subjects were significantly smaller than those in healthy subjects, while Montaudon et al.[64] reported the difference in LA is significant in the branches with generation number greater than three. This difference may be attributed to number of subjects, methods to estimate LA, and normalization by BMI (inter-subject variability), although we think this difference by one generation is insignificant.

The LA of central branches in SA1 subjects were significantly smaller than that in healthy subjects based on branch-by-branch comparison. The LA of healthy subjects agreed reasonably well with that of the healthy subject studied by Horsfield et al.[40] (Figure 5.7 (a)), although the TLC of the latter was not available and assumed to be the average TLC of the former (5.43 L). It was unexpected that the LA of SA1 subjects is significantly smaller than that of healthy subjects even in low-generation branches, e.g., branches 6 and 11. This result should encourage researchers

to investigate asthma in large airways using CT images even if small airways are not resolved.

It seems that the BA of central branches in SA1 subjects were overall larger than that in healthy subjects, but the difference was not significant in most of the branches. The BA of healthy subjects did not agree well with that of the healthy subject studied by Horsfield et al.[40] (Figure 5.8 (a)). For instance, the main bifurcation (branches 1 and 10) is much more asymmetric in the latter than in the former. This discrepancy may be attributed to that the branching angle was estimated based on the geometry near carina, while Horsfield et al.[40] may have used the entire branch; in addition to the inter-subject variability. The difference in BA between healthy and SA1 subjects was not significant in most of the branches mostly because of large inter-subject variability.

5.4.3 Potential Improvements

My analysis of aerosol deposition included three SA1 subjects due to the computational cost of the in-house LES-based numerical aerosol model, but more subjects may be required to draw general conclusions about SA1 subjects. It is ideal to use the geometry of airways before developing severe asthma, but we predicted the geometry based on available data. The in-house numerical aerosol model assumed static airway geometry, steady inspiration, isothermal airflow, and no aerosol growth, and those effects may need to be considered for more realistic simulations in the future.

CHAPTER 6
SUMMARY AND FUTURE WORK

6.1 Summary

6.1.1 Realistic Numerical Human Airway Model

The effect of carrier gas properties on particle transport in the human lung is investigated numerically in an imaging based airway model. The airway model consists of multi-detector row computed tomography (MDCT)-based upper and intrathoracic central airways. The large eddy simulation technique is adopted for simulation of transitional and turbulent flows. The image-registration-derived boundary condition is employed to match regional ventilation of the whole lung. Four different carrier gases of helium (He), a helium-oxygen mixture (He-O_2), air, and a xenon-oxygen mixture (Xe-O_2) are considered. A steady inspiratory flow rate of 342 mL/s is imposed at the mouthpiece inlet to mimic aerosol delivery on inspiration, resulting in the Reynolds number at the trachea of $Re_t \sim 190$, 460, 1300, and 2800 for the respective gases of He, He-O_2, air, and Xe-O_2. Thus, the flow for the He cases is laminar, transitional for He-O_2, and turbulent for air and Xe-O_2. The instantaneous and time-averaged flow fields and the laminar/transitional/turbulent characteristics resulting from the four gases are discussed. With increasing Re_t, the high-speed jet formed at the glottal constriction is more dispersed around the peripheral region of the jet and its length becomes shorter. In the laminar flow the distribution of 2.5-μm particles in the central airways depends on the particle release location at the

mouthpiece inlet, whereas in the turbulent flow the particles are well mixed before reaching the first bifurcation and their distribution is strongly correlated with regional ventilation.

6.1.2 CL-based Geometric Human Airway Model

The author developed new algorithms to automatically identify, classify, and construct the three-dimensional (3-D) geometry of trifurcations in the human lung using the one-dimensional (1-D) tree, which consists of the airway skeleton and branch diameters. The anatomical information about the 1-D tree such as branch connectivity and dimension facilitates data analysis, whereas 3-D geometry is essential for visualization of airway geometry and accurate simulations of gas-flow and aerosol delivery in the airways. A trifurcation is a branching point that has three child branches, and construction of trifurcation geometry is challenging because of the orientations and lengths of the child branches. The existing geometric model does not account for trifurcations, but we expected that trifurcation geometry can be constructed in the framework of the existing geometric bifurcation model. To avoid the intersection and twist of 3-D airway trifurcation surface, we classified trifurcations into two types by topology. The parameters for identification and classification of trifurcations were determined empirically from 8 healthy and 16 severe asthmatic subjects. More than 50% of the subjects had trifurcations between the second- and third-generation branches in right lung, and more than 30% of the subjects had trifurcations between the third- and fourth-generation branches in left lung. We applied the new model to

constructing anatomically-consistent 3-D geometry of the branches that were not resolved by computed tomography (CT). Future models can fit the proposed geometry to CT-based geometry, resulting in more realistic geometry.

6.1.3 Hybrid CL-CT-based Geometric Human Airway Model

The author proposed a new method to automatically construct and mesh 3-D human airway geometry for computational fluid dynamics (CFD)-based simulation of pulmonary gas-flow and aerosol delivery. Traditional methods to construct and mesh realistic CT-based geometry were time-consuming, because it was done manually with image-processing and mesh-generating programs. However, we expected that realistic geometry with curved centerlines (CLs) and non-circular cross-sections can be constructed and meshed automatically, and that the simulation with this geometry would provide accurate regional aerosol distribution on airway-branch scale. The proposed method utilizes anatomical information obtained from the 1-D tree such as branch connectivity and diameters to efficiently construct realistic geometry, generate optimal CFD mesh, specify boundary conditions, and reduce simulations results. The proposed geometric model automatically fits the straight CLs and circular cross-sections of cylinder-like branches called the CL-based geometry to the CT-based geometry, resulting in the hybrid CL-CT-based geometry. Furthermore, the model adds an approximate laryngeal model to the trachea of the hybrid model. The aerosol deposition predicted by the hybrid model agreed well with the prediction by CT-based model. The average geometric error based on 8 healthy and 16 severe

asthmatic subjects was 3.8% branch radius. The approximate laryngeal model generated realistic level of turbulence in the trachea. The proposed method is suited for branch by branch analyses of multiple subjects.

6.1.4 Skeleton of Severe Asthmatic Subjects

The author investigated the effect of airway skeleton structure on aerosol delivery in asthmatic subjects using in-house computational fluid dynamics (CFD)-based numerical human airway models. Several structural and functional variables such as airway skeleton structure, luminal area, and regional ventilation could contribute to the development of asthma caused by aerosol exposure. However, previous studies did not investigate the correlation between skeleton structure and aerosol deposition. We hypothesized that there are asthmatic subjects whose airway skeletons can cause higher aerosol deposition compared to healthy subjects. In the simulations, flow rate and luminal area, i.e., Reynolds and Stokes numbers, in each branch were controlled, but skeleton was subject-specific. This model is similar to the airway before development of asthma. We found significant correlation between diseased branch and aerosol deposition in one of the three severe asthmatic subjects considered even if the luminal area is healthy. The correlation between diseased branch and branching angle was marginally significant for this subject. These results show the possibility that this subject had central branches with larger branching angle compared to healthy subjects, and that caused more aerosol deposition, resulting in diseased branches. We also found a significant difference in luminal area of central branches between two

sub-groups of SA subjects classified by a global parameter of lung function.

6.2 Future Work

6.2.1 Geometric Models

There were branching points with more than three child branches, but the current model can construct the geometry of up to three child branches. Future method could construct quadfurcation geometry still in the same framework of the current model by splitting one of the three child branches into two. In this modification it could be an issue that too many surfaces and volumes are connected to one control node, resulting in skewed CFD mesh elements. In addition, it could be difficult to fit the surfaces at quadfurcation to CT-based geometry, because it is already difficult to fit many surfaces at trifurcations.

Empirically-determined five parameters define the geometry of the current artificial laryngeal model, and the parameters are functions of only the trachea geometry. The parameters could be correlated with the clinical characteristics of subjects such as height and total lung capacity (TLC), and the geometry of branches distal to the trachea. It is possible that statistical methods give better formulae for the parameters that are functions of more variables. The potential issue for this modification is that CT-image of extrathoracic region for a number of subjects may not be easily available, because that is the reason why the artificial laryngeal model is needed.

6.2.2 CFD Models

The current artificial laryngeal model uses two parameters to add synthetic turbulence to the flow above the glottis, and the parameters are functions of the trachea hydraulic diameter and Re. Ideally, the breathing pattern and the geometry of extrathoracic region determine the parameters. If there is a correlation between clinical characteristics of subjects and the length scale of the extrathoracic region, the breathing pattern and the clinical characteristics could determine the parameters. Similar to the artificial laryngeal model, the availability of CT-image of the extrathoracic region could be an issue for this modification.

6.2.3 Applications

The hybrid model has a lot of potential applications because of its ability to manipulate airway structure, and we demonstrated one of them to investigate the effect of airway skeleton structure on aerosol deposition in SA lungs. Future study may need to consider more subjects to draw general conclusions about SA subjects. Potential issue for the future study or one of the reasons why three SA subjects were considered is that it is difficult to control variables. For example, it is difficult to find the SA subjects with similar TLC. If TLC is different, it is difficult to control Re, which is one of the most important non-dimensional parameters governing gas-flow and aerosol delivery in the human lung. Nonetheless, the skeleton and branch diameter can be manipulated in the hybrid model, and this is a powerful tool to test various hypotheses.

Dr. Eric A. Hoffman, Dr. John Newell, and Dr. Meilan Han investigated the correlation between tapering and wall thickness of airway branches using the subjects of the subpopulations and intermediate outcome measures in COPD study (SPIROMICS) (presented at the scientific sessions of the American Thoracic Society 2013; private communication with Dr. Eric A. Hoffman). They found that the tapering of the subjects with a high bronchitis index cluster is different from that of the subjects with a low bronchitis index. Thus, the new geometric modeling and meshing method can be potentially applied to the investigation of the effect of branch tapering on aerosol deposition in the branches with chronic bronchitis.

In addition to the applications to gas-flow and aerosol delivery in the human lung, future studies can use the hybrid model to investigate the detailed geometric characteristics of airway branches. The hybrid model of a branch can consist of sub-branches, and the centerline and control nodes of the non-uniform hybrid model in each sub-branch are fitted to the CT-based geometry. For example, the non-uniform hybrid model can provide curvature of branches, variation of luminal area in branches, and branching angle and luminal geometry of sub-branches. Furthermore, correlation between lung diseases and those geometric characteristics can be investigated.

APPENDIX A
3-D CL-BASED GEOMETRIC AIRWAY MODEL

A.1 Bifurcation Direction

The direction of a bifurcation $\mathbf{n}_b$ is defined as $\mathbf{n}_b = \mathbf{c}_1 \times \mathbf{c}_2 / |\mathbf{c}_1 \times \mathbf{c}_2|$, where $\mathbf{c}_1$ and $\mathbf{c}_2$ are the directions of the first and second child branches, respectively. The direction of y-axis is the same as the projection of $\mathbf{n}_b$ to plane perpendicular to z-axis, i.e., x-y plane. The direction of x-axis is defined by y- and z-axes to make a right-handed Cartesian coordinate system. At a bifurcation, the indices of the child branches are defined when the 1-D tree is constructed with Apollo (VIDA). At an intrinsic trifurcation, the child branches were sorted in descending order by the product of the two angles between own and other two branches, i.e., the first child branch is the farthest from the other two child branches by angle, and $\mathbf{c}_1$ is defined by the first child branch, and $\mathbf{c}_2$ is the average of the second and third child branches. At an extrinsic trifurcation, $\mathbf{n}_b$ is defined using the first bifurcation in the original double bifurcation.

A.2 Directions of s_1- and s_2-curves in Straight Airways

The directions of s_1- and s_2-curves are defined at each CN. The direction of an s_1-curves is positive in the direction of the positive rotation around z-axis, e.g., from right to left node, and the direction of an s_2-curve is positive in the positive z-direction (Figure 2 (a)). The direction of an s-curve at a point on the curve in $oxyz$ is mathematically expressed as $\partial \mathbf{x} / \partial s_j$, where s_j is the coordinate along the s_j-curve.

The direction of s_1-curves at right, front, left, and back nodes are $\partial\mathbf{x}/\partial s_1 = (0,1,0)$, $(1,0,0)$, $(0,1,0)$, and $(1,0,0)$, respectively, and the direction of s_2-curves at the ring nodes is $\partial\mathbf{x}/\partial s_2 = (0,0,1)$. It should be noted that $|\partial\mathbf{x}/\partial s_j| = 1$ at each CN, which is required when using cubic Hermite spline function[26].

A.3 Directions of s_1- and s_2-curves in Bifurcations

The directions of s-curves are not necessarily unique, i.e., $\partial\mathbf{x}/\partial s_j$ is not necessarily continuous, at the CNs of the bifurcation. For example, three s_2-curves are connected to the front node, but their directions are different from each other (Figure 3 (a)). To account for this, multiple 'versions' of directions, or derivatives[26], are defined at the CNs. For example, six surface elements are attached to the front node, so six versions of directions of s-curves are defined at the front node. The version indices of s-curves in element i, iii, iv, v, vi, and ii in Figure 3 (a) are 2, 3, 4, 5, 6, and 7, respectively. Version 1 is reserved for the front node in a straight airway. Versions 2, 3, 6, and 7 of s_1-curve and versions 2 and 7 of s_2-curve are the same as version 1 of respective curves. Versions 3, 4, 5, and 6 of s_2-curve are parallel to the CL of the child branches: versions 3 and 4 to the left child branch and versions 5 and 6 to the right one. Version 4 of s_1-curve is opposite to version 5 of s_1-curve, which is determined using the coordinates of the crux node. Similarly, the directions of the s-curves at every CN were determined using the coordinates of the CNs and the directions of the child branches (e.g., Figures 3 (b) and (c)).

A.4 Directions of s_1- and s_2-curves in Trifurcations

Similar to the bifurcation, we determined multiple versions of directions of s-curve at CNs using the coordinates of CNs and the directions of child branches. At the front node of a fork-type trifurcation (Figure 3.2d), we determined versions 4, 5, 8, and 9 of s_1-curves using the coordinates of the crux nodes, and versions 3, 4, 5, 6, 8, and 9 of s_2-curves using the directions of the child branches. At the left node of a tripod-type trifurcation (Figure 3.2e), we determined versions 6 and 7 of s_1-curves using the coordinates of the left crux node, and versions 6 and 7 of s_2-curves using the directions of the child branches. We determined the directions of the s-curves at every CN in similar ways.

APPENDIX B
DERIVATION OF LOCAL MESH SIZE

In a laminar fully-developed pipe (Poiseuille) flow the wall shear stress τ_w is

$$\tau_w = \frac{8\mu U_b}{D_b} \ , \tag{B.1}$$

where μ is the dynamic viscosity of the fluid, U_b is the local bulk velocity, and D_b is the local diameter. Equation B.1 can be expressed using the ratio of local to the trachea flow rate $r_{Q,l}$ as

$$\tau_w = 8\mu \frac{4Q_t r_{Q,l}}{\pi D_b^2} \frac{1}{D_b} = c \frac{r_{Q,l}}{D_b^3} \ , \tag{B.2}$$

where Q_t is the flow rate in the trachea and c is a constant for any airway. Equation B.2 is used to get the friction velocity u^* and the mesh size in wall unit y^+ as

$$u^* = \sqrt{\tau_w/\rho} = c\sqrt{r_{Q,l}/D_b^3} \text{ and} \tag{B.3}$$

$$y^+ = \frac{u^* y}{\nu} = c\Delta_b \sqrt{\frac{r_{Q,l}}{D_b^3}} \ , \tag{B.4}$$

where ρ is the density of the fluid and Δ_b is the local mesh size. When y^+ is constant for any airway, the local mesh size can be obtained using the trachea mesh size Δ_t:

$$\Delta_b = \Delta_t \sqrt{\frac{D_b^3}{r_{Q,l} D_t^3}} \ , \tag{B.5}$$

where the flow rate ratio for the trachea $r_{Q,t}$ is 1.

REFERENCES

[1] GM Allen, BP Shortall, T. Gemci, TE Corcoran, and NA Chigier. Computational simulations of airflow in an in vitro model of the pediatric upper airways. *Journal of Biomechanical Engineering*, 126(5):604–613, 2004.

[2] S. W. Atwell. Major anomalies of the tracheobronchial tree. *Diseases of the chest*, 52(5):611–615, 1967.

[3] S. Balachandar and J. K. Eaton. Turbulent dispersed multiphase flow. *Annual Review of Fluid Mechanics*, 42:111–133, 2010.

[4] I. Balásházy and W. Hofmann. Particle deposition in airway bifurcationsi. inspiratory flow. *Journal of Aerosol Science*, 24(6):745–772, 1993.

[5] I. Balásházy and W. Hofmann. Deposition of aerosols in asymmetric airway bifurcations. *Journal of Aerosol Science*, 26(2):273–292, 1995.

[6] W. D. Bennett. Targeting respiratory drug delivery with aerosol boluses. *Journal of aerosol medicine*, 4(2):69–78, 1991.

[7] Edward A. Boyden. A synthesis of the prevailing patterns of the bronchopulmonary segments in the light of their variations. *CHEST Journal*, 15(6):657–668, 1949.

[8] T. Brancatisano, PW Collett, and LA Engel. Respiratory movements of the vocal cords. *Journal of applied physiology*, 54(5):1269–1276, 1983.

[9] J. R. Cebral and R. M. Summers. Tracheal and central bronchial aerodynamics using virtual bronchoscopy and computational fluid dynamics. *Medical Imaging, IEEE Transactions on*, 23(8):1021–1033, 2004.

[10] T. L. Chan and M. Lippmann. Experimental measurements and empirical modelling of the regional deposition of inhaled particles in humans. *American Industrial Hygiene Association Journal*, 41(6):399–409, 1980.

[11] T. L. Chan, R. M. Schreck, and M. Lippmann. Effect of the laryngeal jet on particle deposition in the human trachea and upper bronchial airways. *Journal of Aerosol Science*, 11(5-6):447–459, 1980.

[12] K. H. Cheng, Y. S. Cheng, H. C. Yeh, and DL Swift. Measurements of airway

dimensions and calculation of mass transfer characteristics of the human oral passage. *Journal of Biomechanical Engineering*, 119:476, 1997.

[13] J. Choi, M. H. Tawhai, E. A. Hoffman, and C. L. Lin. On intra-and intersubject variabilities of airflow in the human lungs. *Physics of Fluids*, 21:101901, 2009.

[14] J. Choi, G. Xia, M. H. Tawhai, E. A. Hoffman, and C. L. Lin. Numerical study of high-frequency oscillatory air flow and convective mixing in a ct-based human airway model. *Annals of Biomedical Engineering*, pages 1–22, 2010.

[15] Sanghun Choi, Eric A. Hoffman, Sally E. Wenzel, Merryn H. Tawhai, Youbing Yin, Mario Castro, and Ching-Long Lin. Registration-based assessment of regional lung function via volumetric ct images of normals vs. severe asthmatics. *Journal of applied physiology*, 2013.

[16] Y. Choi and DE Wroblewski. Characteristics of glottis-induced turbulence in oscillatory flow: An empirical investigation. *Journal of Biomechanical Engineering*, 120:217, 1998.

[17] JK Comer, C. Kleinstreuer, S. Hyun, and CS Kim. Aerosol transport and deposition in sequentially bifurcating airways. *TRANSACTIONS-AMERICAN SOCIETY OF MECHANICAL ENGINEERS JOURNAL OF BIOMECHANICAL ENGINEERING*, 122(2):152–158, 2000.

[18] T. E. Corcoran and S. Gamard. Development of aerosol drug delivery with helium oxygen gas mixtures. *Journal of Aerosol Medicine*, 17(4):299–309, 2004.

[19] G. K. Crompton. Problems patients have using pressurized aerosol inhalers. *European journal of respiratory diseases.Supplement*, 119:101–104, 1982. LR: 20080221; JID: 8010618; 0 (Aerosols); ppublish.

[20] C. Darquenne, C. van Ertbruggen, and G. K. Prisk. Convective flow dominates aerosol delivery to the lung segments. *Journal of applied physiology*, 111(1):48, 2011.

[21] E. Dekker. Transition between laminar and turbulent flow in human trachea. *Journal of applied physiology*, 16(6):1060, 1961.

[22] M. B. Dolovich, R. C. Ahrens, D. R. Hess, P. Anderson, R. Dhand, J. L. Rau, G. C. Smaldone, and G. Guyatt. Device selection and outcomes of aerosol therapy: Evidence-based guidelines*: American college of chest physicians/american college of asthma, allergy, and immunology. *CHEST Journal*, 127(1):335–371, 2005.

[23] M. J. Donovan, A. Gibbons, M. J. Herpin, S. Marek, S. L. McGill, and H. D. C. Smyth. Novel dry powder inhaler particle-dispersion systems. *Therapeutic Delivery*, 2(10):1295–1311, 2011.

[24] Martin Ester, Hans-Peter Kriegel, Jrg Sander, and Xiaowei Xu. A density-based algorithm for discovering clusters in large spatial databases with noise. In *Proceedings of the 2nd International Conference on Knowledge Discovery and Data mining*, volume 1996, pages 226–231. AAAI Press, 1996.

[25] P. Felkel, R. Wegenkittl, and K. Buhler. Surface models of tube trees. In *Computer Graphics International, 2004. Proceedings*, pages 70–77. IEEE, 2004.

[26] JW Fernandez, P. Mithraratne, SF Thrupp, MH Tawhai, and PJ Hunter. Anatomically based geometric modelling of the musculo-skeletal system and other organs. *Biomechanics and Modeling in Mechanobiology*, 2(3):139–155, 2004.

[27] W. H. Finlay. *The mechanics of inhaled pharmaceutical aerosols: An introduction*. Academic Pr, 2001.

[28] R. K. Freitas and W. Schröder. Numerical investigation of the three-dimensional flow in a human lung model. *Journal of Biomechanics*, 41(11):2446–2457, 2008.

[29] W. J. Gauderman, E. Avol, F. Gilliland, H. Vora, D. Thomas, K. Berhane, R. McConnell, N. Kuenzli, F. Lurmann, and E. Rappaport. The effect of air pollution on lung development from 10 to 18 years of age. *New England Journal of Medicine*, 351(11):1057–1067, 2004.

[30] W. J. Gauderman, C. Murcray, F. Gilliland, and D. V. Conti. Testing association between disease and multiple snps in a candidate gene. *Genetic epidemiology*, 31(5):383–395, 2007.

[31] T. Gemci, V. Ponyavin, Y. Chen, H. Chen, and R. Collins. Computational model of airflow in upper 17 generations of human respiratory tract. *Journal of Biomechanics*, 41(9):2047–2054, 2008.

[32] C. Geuzaine and J. F. Remacle. Gmsh: A 3-d finite element mesh generator with built-in pre-and post-processing facilities. *International Journal for Numerical Methods in Engineering*, 79(11):1309–1331, 2009.

[33] A. D. Gosman and E. Ioannides. Aspects of computer simulation of liquid-fuelled combustors. *Journal of Energy*, 7:482–490, 1983.

[34] B. Grgic, W. H. Finlay, P. K. P. Burnell, and A. F. Heenan. In vitro intersubject and intrasubject deposition measurements in realistic mouth-throat geometries. *Journal of Aerosol Science*, 35(8):1025–1040, 2004.

[35] H. K. Hahn, B. Preim, D. Selle, and H. O. Peitgen. Visualization and interaction techniques for the exploration of vascular structures. In *Visualization, 2001. VIS'01. Proceedings*, pages 395–578. IEEE, 2001.

[36] T. Heistracher and W. Hofmann. Physiologically realistic models of bronchial airway bifurcations. *Journal of Aerosol Science*, 26(3):497–509, 1995.

[37] J. Heyder, J. Gebhart, G. Rudolf, C. F. Schiller, and W. Stahlhofen. Deposition of particles in the human respiratory tract in the size range 0.005-15 [mu] m. *Journal of Aerosol Science*, 17(5):811–825, 1986.

[38] W. C. Hinds. Aerosol technology: properties, behavior, and measurement of airborne particles. 1982.

[39] Werner Hofmann. Modelling inhaled particle deposition in the human lunga review. *Journal of Aerosol Science*, 42(10):693–724, 2011.

[40] K. Horsfield, G. Dart, D. E. Olson, G. F. Filley, and G. Cumming. Models of the human bronchial tree. *Journal of applied physiology*, 31(2):207, 1971.

[41] K. Inthavong, J. Tu, Y. Ye, S. Ding, A. Subic, and F. Thien. Effects of airway obstruction induced by asthma attack on particle deposition. *Journal of Aerosol Science*, 41(6):587–601, 2010.

[42] Nizar N. Jarjour, Serpil C. Erzurum, Eugene R. Bleecker, William J. Calhoun, Mario Castro, Suzy AA Comhair, Kian Fan Chung, Douglas Curran-Everett, Raed A. Dweik, and Sean B. Fain. Severe asthma lessons learned from the national heart, lung, and blood institute severe asthma research program. *American journal of respiratory and critical care medicine*, 185(4):356–362, 2012.

[43] N. Jarrin, R. Prosser, J. C. Uribe, S. Benhamadouche, and D. Laurence. Reconstruction of turbulent fluctuations for hybrid rans/les simulations using a synthetic-eddy method. *International Journal of Heat and Fluid Flow*, 30(3):435–442, 2009.

[44] S. T. Jayaraju, M. Brouns, C. Lacor, B. Belkassem, and S. Verbanck. Large eddy and detached eddy simulations of fluid flow and particle deposition in a human mouth-throat. *Journal of Aerosol Science*, 39(10):862–875, 2008.

[45] P. K. Jeffery. Remodeling in asthma and chronic obstructive lung disease. *American journal of respiratory and critical care medicine*, 164(Supplement 2):S28–S38, 2001.

[46] D. Khler. Aerosols for systemic treatment. *Lung*, 168:677–684, 1990.

[47] C. S. Kim and A. J. Iglesias. Deposition of inhaled particles in bifurcating airway models: I. inspiratory deposition. *Journal of Aerosol Medicine*, 2(1):1–14, 1989.

[48] C. Kleinstreuer and Z. Zhang. Laminar-to-turbulent fluid-particle flows in a human airway model. *International Journal of Multiphase Flow*, 29(2):271–289, 2003.

[49] H. Kumar, M. H. Tawhai, E. A. Hoffman, and C. L. Lin. Steady streaming: A key mixing mechanism in low-reynolds-number acinar flows. *Physics of Fluids*, 23:041902, 2011.

[50] N. R. Labiris and M. B. Dolovich. Pulmonary drug delivery. part i: Physiological factors affecting therapeutic effectiveness of aerosolized medications. *British journal of clinical pharmacology*, 56(6):588–599, 2003.

[51] A. R. Lambert, P. T. O'shaughnessy, M. H. Tawhai, E. A. Hoffman, and C. L. Lin. Regional deposition of particles in an image-based airway model: large-eddy simulation and left-right lung ventilation asymmetry. *Aerosol Science and Technology*, 45(1):11–25, 2011.

[52] DongYoub Lee, Chris Wallis, Laura S. Van Winkle, and Anthony S. Wexler. Disruption of tracheobronchial airway growth following postnatal exposure to ozone and ultrafine particles. *Inhalation toxicology*, 23(9):520–531, 2011.

[53] C. L. Lin, H. Lee, T. Lee, and L. J. Weber. A level set characteristic galerkin finite element method for free surface flows. *International Journal for Numerical Methods in Fluids*, 49(5):521–547, 2005.

[54] C. L. Lin, M. H. Tawhai, G. McLennan, and E. A. Hoffman. Characteristics of the turbulent laryngeal jet and its effect on airflow in the human intra-thoracic airways. *Respiratory physiology & neurobiology*, 157(2-3):295–309, 2007.

[55] C. L. Lin, M. H. Tawhai, G. McLennan, and E. A. Hoffman. Multiscale simulation of gas flow in subject-specific models of the human lung. *IEEE ENGINEERING IN MEDICINE AND BIOLOGY MAGAZINE*, pages 26–33, 2009.

[56] M. Lippmann, D. B. Yeates, and R. E. Albert. Deposition, retention, and

clearance of inhaled particles. *British journal of industrial medicine*, 37(4):337, 1980.

[57] Y. Liu, R. M. C. So, and C. H. Zhang. Modeling the bifurcating flow in an asymmetric human lung airway. *Journal of Biomechanics*, 36(7):951–959, 2003.

[58] P. Longest, S. Vinchurkar, and T. Martonen. Transport and deposition of respiratory aerosols in models of childhood asthma. *Journal of Aerosol Science*, 37(10):1234–1257, 2006.

[59] B. Ma and K. R. Lutchen. An anatomically based hybrid computational model of the human lung and its application to low frequency oscillatory mechanics. *Annals of Biomedical Engineering*, 34(11):1691–1704, 2006.

[60] B. Ma and K. R. Lutchen. Cfd simulation of aerosol deposition in an anatomically based human largemedium airway model. *Annals of Biomedical Engineering*, 37(2):271–285, 2009.

[61] E. Marchandise, C. Geuzaine, and JF Remacle. Cardiovascular and lung mesh generation based on centerlines. *International journal for numerical methods in biomedical engineering*, 2013.

[62] TB Martonen. Mathematical model for the selective deposition of inhaled pharmaceuticals. *Journal of pharmaceutical sciences*, 82(12):1191–1199, 1993.

[63] S. Miyawaki, M. H. Tawhai, E. A. Hoffman, and C. L. Lin. Effect of carrier gas properties on aerosol distribution in a ct-based human airway numerical model. *Annals of Biomedical Engineering*, pages 1–13, 2012.

[64] M. Montaudon, M. Lederlin, S. Reich, H. Begueret, J. M. Tunon de Lara, R. Marthan, P. Berger, and F. Laurent. Bronchial measurements in patients with asthma: Comparison of quantitative thin-section ct findings with those in healthy subjects and correlation with pathologic findings1. *Radiology*, 253(3):844–853, 2009.

[65] S. A. Morsi and A. J. Alexander. An investigation of particle trajectories in two-phase flow systems. *Journal of Fluid Mechanics*, 55(02):193–208, 1972.

[66] Institute of Medicine (US). Committee on the Assessment of Asthma and Indoor Air. *Clearing the Air: Asthma and Indoor Air Exposures*. National Academy Press, 2000.

[67] D. Orphanidou, JM Hughes, MJ Myers, AR Al-Suhali, and B. Henderson. To-

mography of regional ventilation and perfusion using krypton 81m in normal subjects and asthmatic patients. *Thorax*, 41(7):542–551, 1986.

[68] K. Palágyi, J. Tschirren, E. A. Hoffman, and M. Sonka. Quantitative analysis of pulmonary airway tree structures. *Computers in biology and medicine*, 36(9):974–996, 2006.

[69] RF Phalen, HC Yeh, GM Schum, and OG Raabe. Application of an idealized model to morphometry of the mammalian tracheobronchial tree. *The Anatomical Record*, 190(2):167–176, 1978.

[70] D. L. Ross and R. K. Schultz. Effect of inhalation flow rate on the dosing characteristics of dry powder inhaler (dpi) and metered dose inhaler (mdi) products. *Journal of aerosol medicine*, 9(2):215–226, 1996.

[71] J. Sandeau, I. Katz, R. Fodil, B. Louis, G. Apiou-Sbirlea, G. Caillibotte, and D. Isabey. Cfd simulation of particle deposition in a reconstructed human oral extrathoracic airway for air and helium-oxygen mixtures. *Journal of Aerosol Science*, 41(3):281–294, 2010.

[72] Gabriela Sbirlea-Apiou, Marc Lemaire, Ira Katz, Joy Conway, John Fleming, and Ted Martonen. Simulation of the regional manifestation of asthma. *Journal of pharmaceutical sciences*, 93(5):1205–1216, 2004.

[73] A. Schmidt, S. Zidowitz, A. Kriete, T. Denhard, S. Krass, and H. O. Peitgen. A digital reference model of the human bronchial tree. *Computerized Medical Imaging and Graphics*, 28(4):203–211, 2004.

[74] Y. J. Son and J. T. McConville. Advancements in dry powder delivery to the lung. *Drug development and industrial pharmacy*, 34(9):948–959, 2008.

[75] R. M. Spencer, J. D. Schroeter, and T. B. Martonen. Computer simulations of lung airway structures using data-driven surface modeling techniques. *Computers in biology and medicine*, 31(6):499–511, 2001.

[76] R. C. Splechtna, A. L. Fuhrmann, and R. Wegenkittl. *ARAS-augmented reality aided surgery system description*, 2002.

[77] W. Stahlhofen, G. Rudolf, and A. C. James. Intercomparison of experimental regional aerosol deposition data. *Journal of Aerosol Medicine*, 2(3):285–308, 1989.

[78] K. W. Stapleton, E. Guentsch, M. K. Hoskinson, and W. H. Finlay. On the suitability of k-turbulence modeling for aerosol deposition in the mouth and

throat: a comparison with experiment. *Journal of Aerosol Science*, 31(6):739–749, 2000.

[79] R. P. Subramaniam, B. Asgharian, J. I. Freijer, F. J. Miller, and S. Anjilvel. Analysis of lobar differences in particle deposition in the human lung. *Inhalation toxicology*, 15(1):1–21, 2003.

[80] M. H. Tawhai, E. A. Hoffman, and C. L. Lin. The lung physiome: merging imaging-based measures with predictive computational models. *Wiley Interdisciplinary Reviews: Systems Biology and Medicine*, 1(1):61–72, 2009.

[81] M. H. Tawhai, P. Hunter, J. Tschirren, J. Reinhardt, G. McLennan, and E. A. Hoffman. Ct-based geometry analysis and finite element models of the human and ovine bronchial tree. *Journal of applied physiology*, 97(6):2310, 2004.

[82] B. H. Thompson, W. J. Lee, J. R. Galvin, and J. S. Wilson. Lung anatomy. in: Virtual hospital: The apprentices assistant (online). The University of Iowa College of Medicine, 2004. http://www.vh.org/Providers/Textbooks/LungAnatomy/LungAnatomy.html.

[83] G. Tian, P. W. Longest, G. Su, and M. Hindle. Characterization of respiratory drug delivery with enhanced condensational growth using an individual path model of the entire tracheobronchial airways. *Annals of Biomedical Engineering*, 39(3):1136–1153, 2011.

[84] C. van Ertbruggen, C. Hirsch, and M. Paiva. Anatomically based three-dimensional model of airways to simulate flow and particle transport using computational fluid dynamics. *Journal of applied physiology*, 98(3):970, 2005.

[85] I. Volkau, W. Zheng, R. Baimouratov, A. Aziz, and W. L. Nowinski. Geometric modeling of the human normal cerebral arterial system. *Medical Imaging, IEEE Transactions on*, 24(4):529–539, 2005.

[86] A. W. Vreman. An eddy-viscosity subgrid-scale model for turbulent shear flow: Algebraic theory and applications. *Physics of Fluids*, 16:3670, 2004.

[87] W. Wall, P. Gamnitzer, and A. Gerstenberger. Fluid-structure interaction approaches on fixed grids based on two different domain decomposition ideas. *International Journal of Computational Fluid Dynamics*, 22(6):411–427, 2008.

[88] D. Walters, G. Burgreen, D. Lavallee, D. Thompson, and R. Hester. Efficient, physiologically realistic lung airflow simulations. *Biomedical Engineering, IEEE Transactions on*, (99):1–1, 2011.

[89] D. K. Walters and W. H. Luke. A method for three-dimensional navierstokes simulations of large-scale regions of the human lung airway. *Journal of Fluids Engineering*, 132:051101, 2010.

[90] E. R. Weibel. *Morphometry of the human lung.* Academic Press, New York, 1963.

[91] World Health Organization (WHO). Fact sheet no. 307 on asthma. 2011.

[92] X. Wu, V. Luboz, K. Krissian, S. Cotin, and S. Dawson. Segmentation and reconstruction of vascular structures for 3d real-time simulation. *Medical image analysis*, 15(1):22–34, 2011.

[93] J. Xi and P. Longest. Transport and deposition of micro-aerosols in realistic and simplified models of the oral airway. *Annals of Biomedical Engineering*, 35(4):560–581, 2007.

[94] H. C. Yeh and GM Schum. Models of human lung airways and their application to inhaled particle deposition. *Bulletin of mathematical biology*, 42(3):461–480, 1980.

[95] Y. Yin, J. Choi, E. A. Hoffman, M. H. Tawhai, and C. L. Lin. Simulation of pulmonary air flow with a subject-specific boundary condition. *Journal of Biomechanics*, 43(11):2159–2163, 2010.

[96] Y. Zhang, Y. Bazilevs, S. Goswami, C. L. Bajaj, and T. J. R. Hughes. Patient-specific vascular nurbs modeling for isogeometric analysis of blood flow. *Computer Methods in Applied Mechanics and Engineering*, 196(29-30):2943–2959, 2007.

[97] Z. Zhang and C. Kleinstreuer. Effect of particle inlet distributions on deposition in a triple bifurcation lung airway model. *Journal of Aerosol Medicine*, 14(1):13–29, 2001.

[98] Z. Zhang and C. Kleinstreuer. Laminar-to-turbulent fluidnanoparticle dynamics simulations: Model comparisons and nanoparticle-deposition applications. *International Journal for Numerical Methods in Biomedical Engineering*, 27:1930–1950, 2011.

[99] X. Zhao, Y. Ju, C. Liu, J. Li, M. Huang, J. Sun, and T. Wang. Bronchial anatomy of left lung: a study of multi-detector row ct. *Surgical and radiologic anatomy*, 31(2):85–91, 2009.

[100] Y. Zhou and Y. S. Cheng. Particle deposition in a cast of human tracheobronchial airways. *Aerosol Science and Technology*, 39(6):492–500, 2005.